July 2020

SEQUENCE CONTROL OF COMPLEX COACERVATION

Li-Wei Chang
University of Massachusetts Amherst

SEQUENCE CONTROL OF COMPLEX COACERVATION

A Dissertation Presented

by

LI-WEI CHANG

Submitted to the Graduate School of the
University of Massachusetts Amherst in partial fulfillment
of the requirements for the degree of

DOCTOR OF PHILOSOPHY

May 2020

Chemical Engineering

SEQUENCE CONTROL OF COMPLEX COACERVATION

A Dissertation Presented

by

LI-WEI CHANG

Approved as to style and content by:

_____
Sarah L. Perry, Chair

_____
Neil S. Forbes, Member

_____
John Klier, Member

_____
Ryan C. Hayward, Outside Member

_____
John Klier, Department Head
Chemical Engineering

ACKNOWLEDGMENTS

I would like to express my sincere appreciation to my advisor, Prof. Sarah Perry for her guidance and support over the years. I want to thank her for continually conveying the knowledge of science, as well as suggestions of resolving problems. In addition, she put a lot of effort to help me improve my presentation and article writing skills. It really benefited my research and future career. Without her persistent help this dissertation would not have been possible.

I also want to thank Prof. Charles Sing along with his students Dr. Tyler Lytle and Jason Madinya. Their inspirational computational and theoretical works really have provided me insightful explanations for the phenomena I have observed in my experiments. I really enjoyed the collaboration and hope we will have more opportunity to work with in the future.

In addition, I would like to thank my groupmates for their assistance in the lab. Zoey Meng was always helpful in learning about instruments that I am not familiar with, as well as discussing science. I really enjoyed the time spent with all of you, and wish you all the best in the future.

A variety of other people have been key in the development of this dissertation. Prof. Rachel Letteri was invaluable in her assistance of peptide cleavage. I would like to thank Dr. Stephen Eyles for his help in Mass Spectrometry, as well as Dr. Lizz Bartlett's for her assistance in maintenance and troubleshooting of isothermal titration calorimetry.

Last but not least, I want to thank my beloved family. Although we are not able to see each other very often, you are always in my mind. Without your love and support, I can never achieve my dream of pursing my PhD in Unites States. Besides, I want to especially thank my dear friends, Ning-Yi Hsu, James Dai, and Yueh-Chun Wu. Thank you for always being there for me when I was down and need someone to talk to. Without your help and accompany, I can never finish this long journey.

ABSTRACT

SEQUENCE CONTROL OF COMPLEX COACERVATION

May 2020

LI-WEI CHANG, B.S., NATIONAL CHUNG HSING UNIVERSITY

M.S., NATIONAL CENTRAL UNIVERSITY

Ph.D., UNIVERSITY OF MASSACHUSETTS AMHERST

Directed by: Professor Sarah L. Perry

Complex coacervation is a liquid-liquid phase separation driven by the complexation of oppositely charged polyelectrolytes. The resulting coacervate phase has been used for many applications, such as underwater adhesives, drug delivery, food and personal care products. There also has been increasing interest in coacervate-like droplets occurring in biological systems. The majority of these "membraneless organelles" involve a combination of intrinsically-disordered proteins and RNA, and phase separate due to long-range charge effects and short-range hydrophobic effects. While evolution has optimized the self-assembly of these types of biological polymers, our ability to design such materials remains limited, in part because the relevant interactions that occur over a wide range of different length scales.

The goal of this research is to establish molecular-level design rules as to how chemical sequence can modulate the formation and properties of complex coacervates. While studies to date have focused on the effect of parameters such as the charge stoichiometry, temperature, pH, salt concentration, stereochemistry, polymer architecture, and the density of charges present, the ability to pattern the sequence of charges and other chemistries has been rarely studied. However, polypeptides represent a model platform for the synthesis and study of polyelectrolytes with precisely controlled polymer architecture and sequence patterning at the molecular level, while retaining relevance to a variety of biological, medical, and industrial applications. Experimental measures such as turbidimetry and optical microscopy, coupled with isothermal titration calorimetry were used to study how variations in the patterning and overall fraction of charged

groups along the polymer affect coacervate phase behavior. Increasing the number of charged residues increased the salt resistance and the size of the two-phase region. More interestingly, a comparison between polypeptides with the same overall charge fraction, but different periodic repeating patterns of charged monomers showed an increase in coacervate stability with increasing charge block size. Thermodynamic data, coupled with insights from simulation showed that the increase in stability was entropic in nature, resulting from differences in the one-dimensional confinement of counterions along the patterned polymer. We have also explored arbitrary sequences, hydrophobicity, and the identity of salt, as well as the self-coacervation of polyampholytes.

TABLE OF CONTENTS

LIST OF TABLES

Table Page

LIST OF FIGURES

Figure Page

CHAPTER 1

INTRODUCTION

Complex coacervation is a liquid-liquid phase separation phenomenon driven by the electrostatic and entropically-driven complexation of oppositely charged polyelectrolytes (Figure 1.1a,b).[1–6] The resulting coacervate phase retains significant amounts of water and ions and displays an extremely low surface tension that has enabled the use of these materials for many applications, such as underwater adhesives, drug delivery, food and personal care products. There also has been increasing interest in coacervate-like droplets occurring in biological systems.[7–9] The majority of these so-called membraneless organelles involve a combination of intrinsically-disordered proteins and RNA, and phase separate due to a combination of long-range charge effects and short-range hydrophobic effects (Figure 1c).[7] While evolution has optimized the self-assembly of biological materials over millions of years, our ability to design such materials remains limited, in part because the relevant interactions that occur over a wide range of different length scales.

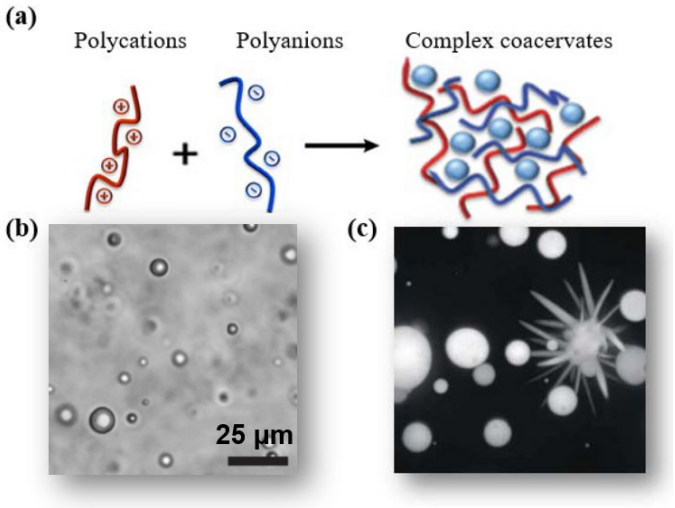

Figure 1.1. (a) Schematic depiction of polyelectrolyte complex formation. Optical micrographs of (b) liquid complex coacervates, and (c) liquid droplets and sea urchin-like solid protein granules related to amyotrophic lateral sclerosis (ALS). Adapted from Cell, 162 (5), Patel, A.; Lee, H. O.; Jawerth, L.; Maharana, S.; Jahnel, M.; Hein, M. Y.; Stoynov, S.; Mahamid, J.; Saha, S.; Franzmann, T. M.; Pozniakovski, A.; Poser, I.; Maghelli, N.; Royer, L. A.; Weigert, M.; Myers, E. W.; Grill, S.; Drechsel, D.; Hyman, A. A.; Alberti, S. A.. Liquid-to-Solid Phase Transition of the ALS Protein FUS Accelerated by Disease Mutation, 1066–1077, Copyright (2015), with permission from Elsevier.

In this dissertation, I look to establish molecular-level design rules as to how chemical sequence can modulate the formation and properties of complex coacervates (Figure 1.2). While studies to date have focused on the effect of parameters such as the charge stoichiometry, temperature, pH, salt concentration, stereochemistry,[10–13] polymer architecture,[14] and the density of charges present, the ability to pattern the sequence of charges and other chemistries has been rarely studied, due to the difficulty of synthesizing polyelectrolytes with equal chain length and charge density, but different distributions of charge or other functionalities. However, polypeptides represent a model platform for the synthesis and study of polyelectrolytes with precisely controlled polymer architecture and sequence patterning at the molecular level, while retaining relevance to a variety of biological, medical, and industrial applications.[15,16] I hypothesize that control over the density and distribution of charge and hydrophobicity within coacervating polymers can be used as a composition-independent strategy for modulating the phase behavior, and potentially the rheological properties of the material.

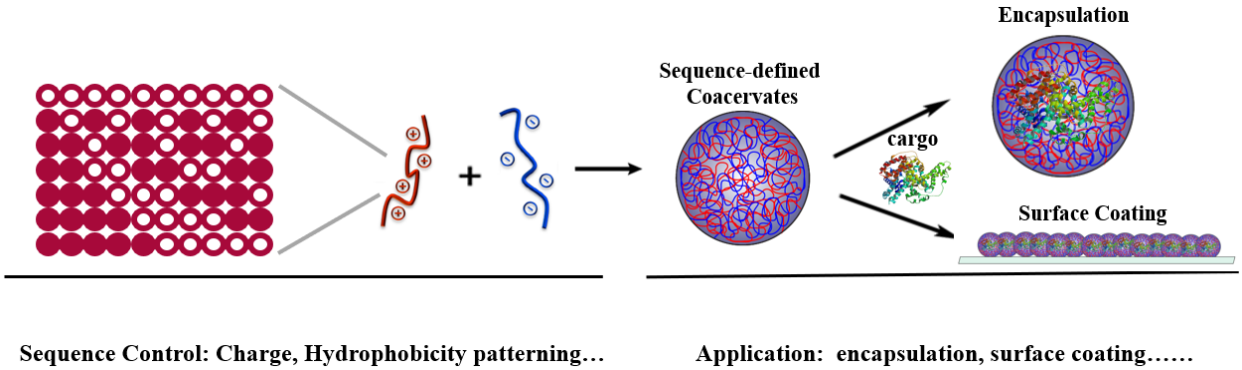

Figure 1.2. Sequence-controlled coacervates can be used for a range of industrial applications ranging from cargo encapsulation to active surface coatings.

1.1 Complex Coacervation

Complex coacervates were first reported by Bungenberg de Jong and Kruyt when they observed there was a liquid-liquid phase separation occurring in the mixture of gelatin and gum Arabic. They called these dense, colloid-rich droplets in this protein-polysaccharide mixing system "coacervates," which came from the prefix *co* and Latin word *acervus*, meaning "coming together

in a heap."[17] Unlike simple coacervation, which occurs as a segregative phase separation due to thermodynamic incompatibility or a net repulsion between macromolecules, complex coacervation is an associative phase separation resulting from a strong affinity of oppositely-charged species in aqueous solution.[18,19] Complex coacervation is an entropically driven process, where the initial electrostatic attraction between oppositely charged polyelectrolytes is followed by the release of small, bound counter-ions and the restructuring of water molecules (Figure 1.1a).[20–23] Complex coacervates initially form as macroion-rich droplets distributed in a macroion-poor supernatant, and will gradually coalesce over time (Figure 1.1b).[23]

Since complex coacervation is a charge-driven phenomenon, many different types of charged macroions have been found to form coacervates, including biological polymers, synthetic polymers, surfactants, folded proteins, and nanoparticles. In fact, due to the ubiquity of charged molecules in water, complex coacervates could be found everywhere in nature and our daily life.

1.2 Complex Coacervation in Nature

Complex coacervation is an associative liquid-liquid phase separation, and can be found broadly in nature. For example, researches have shown that coacervating proteins can be produced by marine organisms such as mussels, tubeworms and sandcastle worms as a natural underwater adhesive.[24] For example, the sandcastle worm can secrete sticky, water-immiscible, coacervate-like materials comprised of oppositely charged proteins and curing agent to glue sand and small mineral particles together to form tubular shells with strong mechanical properties for protection. This natural underwater adhesive of the sandcastle worm has unique properties, such as wet interfacial adhesion, underwater delivery, and triggered solidification,[24–26] and has become the inspiration for the development of industrial synthetic coacervate-based underwater adhesives.[27]

Over the last decade, research about complex coacervation occurring in biology has drawn a lot of attention. Coacervate-like liquid-liquid phase separation has been broadly observed in biological system as "membraneless organelles," formed from complexes of RNA and intrinsically

disordered proteins (IDPs), which are proteins that do not fold into stable structure spontaneously.[28–31] Figure 1.3 shows some examples of membraneless organelles existing in living cells.[32] One of the most important functions of membraneless organelles, as with any organelle, is compartmentalization. In contrast to traditional membrane-bound organelles, this liquid-liquid phase separation creates an interface that allow for the easy transport of biomaterials into and out of compartment. This natural partitioning of biomaterials can facilitate the generation of locally high concentrations of bio-reactants or the spatial colocalization of materials, which can facilitate more efficient reactions.[33,34]

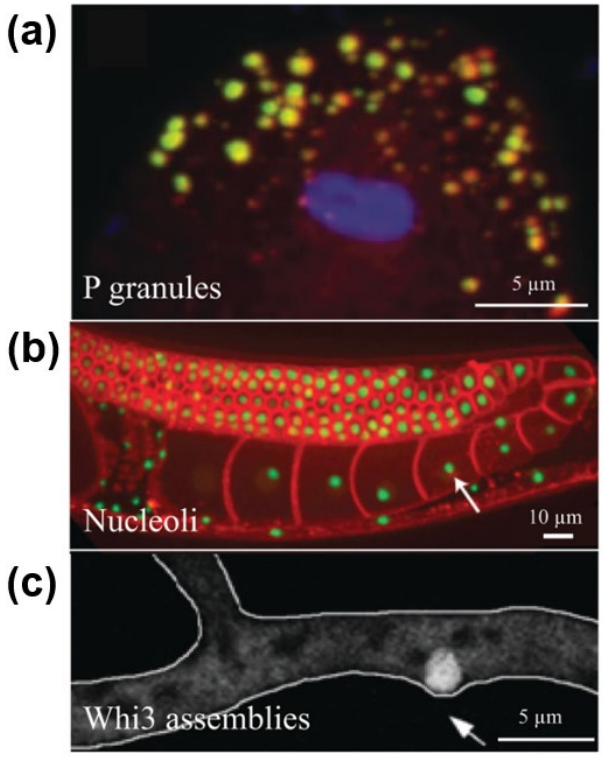

Figure 1.3. Some common membraneless organells can be found in living cells. **(a)** P granules (yellow circle) within the *C. elegans* embryo **(b)** Nucleoli (green circle) within the *C. elegans* hermaphrodite **(c)** Whi3 assemblies (white circle) in the hypha of the multinucleate fungus *Ashbya gossypii*. (Taylor *et al.*, *Soft Matter*, 2016)[32]. Adapted by permission of The Royal Society of Chemistry.

Recently, there has been increasing interest in understanding how IDPs can influence the formation of membraneless organelles through a coacervate-like phase separation process.[35]

Despite this lack of hierarchical order, recent work has shown that the precise sequence of charged amino acids still plays a defining role in the structure and function of IDPs.[8,9,36–41] The properties of IDPs is generally related to their containing sequences of low complexity. However, understanding the underlying physics of the behavior and function of IDPs is still a challenge due to the necessary inclusion of the complex diversity of interactions and sequence effects into macromolecular models. One common approach that has been used to understand the effect of sequence on the behavior of IDPs is the use of model polymer systems as a synthetic, non-biological analogue.[34,42–51] Polyampholytes, which are polymers containing both positive and negative charges, are particularly useful in this role due to the abundance of charged amino acids in IDPs (at least 75% of IDPs are polyampholytes).[52] In this thesis, we will systematically investigate the effect of the patterning of positive and negative charges to elucidate the physics of such sequence-dependent phase behavior in polyampholytes.

1.3 The Application of Complex Coacervates in Industry

Complex coacervation has long been used for industrial applications ranging from encapsulation and delivery to surface coatings and underwater adhesives.[18,27,53–58] One of the most common applications of complex coacervation is in encapsulation application due to its unique properties enabling encapsulation of both hydrophilic and hydrophobic cargo in water and the extremely low surface energy of coacervates.[6,59–62]Tromp *et al.* and Tuinier *et al*. have discovered that positively charged pectins can prevent milk from flocculating by forming coacervate-like aggregates with negatively charged casein micelles.[63,64] Complex coacervation also has been applied in pharmaceutical encapsulation as a promising carrier for drug or other biomolecule delivery.[6,60–62] Vecchies *et al.* have designed complex coacervates forming by a lactose-modified chitosan with hyaluronic acid as a pH-responsive drug carrier with significant scavenging activity.[60] Surface coatings are also another promising application for complex coacervates.[18,27,53–56]

Researchers have shown that coacervate-based hydrogels[53,65,66] and films[67] can be applied in low biofouling coatings.

Since complex coacervation is an electrostatically-induced phenomenon, most of the coacervate-based materials are very sensitive to the change of pH, ionic strength, and temperature. Therefore, complex coacervates have a great potential as a stimuli-responsive carrier. As a result, in order to design coacervate-based materials for different applications, we need to develop a more comprehensive understanding of the underlying physics of the behavior of complex coacervates. In this thesis, we will address the behavior of complex coacervation from the molecular level, with a goal of establishing design principles for the creation of coacervate-based materials for different applications.

1.4 Phase Behavior of Complex Coacervates

Complex coacervation is a liquid-liquid phase separation phenomenon driven by the electrostatic and entropically-driven complexation of oppositely charged polyelectrolytes. The resulting two phases consist of a polymer-rich complex coacervate phase and a polymer dilute phase.[17,68] This macroscopic phase separation will gradually decrease with increasing salt concentration, with all phase separation being suppressed above a critical point.[11,18] This sensitivity to salt makes complex coacervates a promising material platform as a stimuli-responsive material, especially for potential applications under different biological conditions. Thus, understanding the phase behavior is critical to the material development of complex coacervates for various applications. A phase diagram is commonly utilized to describe the phase behavior of complex coacervates. Figure 1.4 shows a generalized phase diagram for complex coacervation calculated using the Voorn-Overbeek theory. A typical coacervate system consists of four different components: polycations P, polyanions Q, water, and salt.[18,68] While the limitations of the Voorn-Overbeek theory have been widely discussed in the literature (*i.e.*, this theory does not take into account the connectivity between polymer chains or the physical size of molecules), the overall

shape of the phase diagram is generally correct.[18,69] The phase boundary for the complex coacervate system can be mapped out to a three-dimensional curved surface. Compositions lying underneath this surface will phase will undergo phase separation to form polymer-rich complex coacervation and polymer-poor supernatant. More commonly, coacervation is considered for a system at a known, stoichiometric composition, and a two-dimensional phase diagram showing total polymer concentration vs. salt concentration is used (Figure 1.4c).

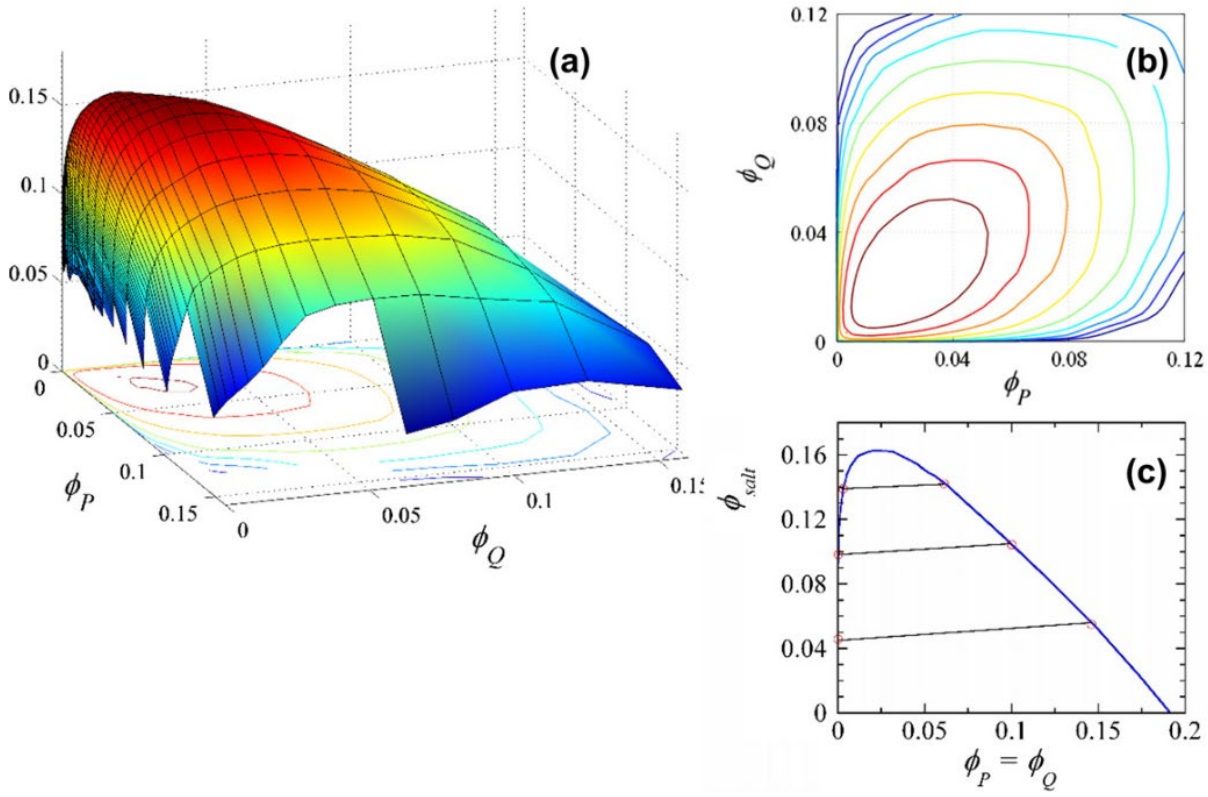

Figure 1.4. (a) Three-dimensional phase diagram for complex coacervation calculated by Voorn-Overbeek theory. (ϕ_P: volume fraction of polycation, ϕ_Q: volume fraction of polyanion, ϕ_{salt}: volume fraction of salt; N_p=N_Q=100) (b) Two-dimensional phase diagram of complex coacervation (c) Binodal curve and tie-lines fo stoichiometric mixing polymers.[18] Adapted from *Journal of Colloid and Interface Science,* 361 (2), Gucht, J. van der; Spruijt, E.; Lemmers, M.; Cohen Stuart, M. A. Polyelectrolyte complexes: Bulk phases and colloidal systems, 407–422. Copyright (2011), with permission from Elsevier.

1.5 Theory of Complex Coacervation

The original theory to describe the phase behavior of complex coacervation was proposed by Voorn and Overbeek. This theory is based on several assumptions, such as the interaction between charges only through the Debye−Hückel attraction that arises in unconnected, dilute electrolytes.[11,68,70,71] Although Voorn-Overbeek theory failed to take molecular-level details such as connectivity, the differences of charged species (polyelectrolytes and salts), and excluded volumes into account, it has been shown to provide reasonable agreement with experimental measures of the phase behavior. Work by Radhakrishna *et al.* indicated this coincident match is from the fortuitous cancellation of polymer chain connectivity and excluded volume effects.[72]

Recently, our collaborators Lytle and Sing have proposed a new "Transfer matrix theory" to predict the phase behavior of complex coacervation in a way that reflects these important molecular features.[69,73,74] Informed by simulation results, this model keeps track of the oppositely charged ions and polyelectrolytes surrounding a test polyelectrolyte, by mapping to an monomeric adsorption model and translating this information into a binodal phase diagram (Figure 1.5). This transfer matrix approach has been supported by our experimental results and we will discuss more details in Chapter 3.

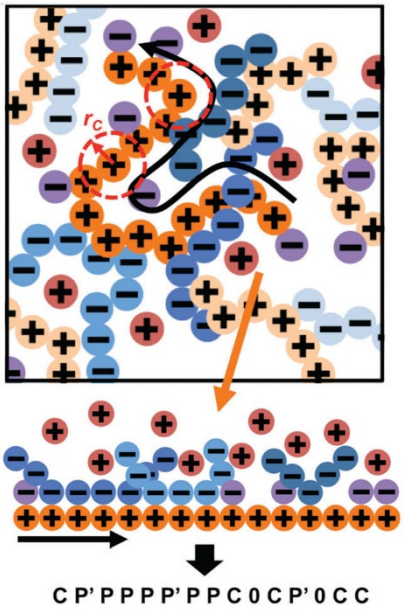

Figure 1.5. Transfer matrix theory uses statistical thermodynamics to correlate how oppositely charged polymers and small-molecule ions interact with a test polymer chain (orange) in a 1-D adsorption model (Lytle and Sing, *Soft Matter*, 2017).[69]

1.6 Summary

Nature has shown that the properties of complex coacervates can be tuned by changing the sequence and chemistry of monomers present in the complexing polymers. As a result, in order to design complex coacervate-based materials with precisely tunable properties to meet various applications, there is a need to develop more comprehensive design principles that are able to address the molecular-level details. Sequence control of polymers is a tremendously powerful approach that looks to be the future of materials design. However, few efforts have been made in this area to date due to the difficulty of synthesis sequence-controlled polymers. In this thesis, we will take advantage of the advanced development of solid-phase polypeptide synthesis to facilitate the preparation of sequence controlled polymers to address the question of sequence effects on complex coacervation. In Chapter 2, we examine how regular patterns of charge can influence the phase behavior of complex coacervation, and identified how these patterns affect the thermodynamic driving force for complexation. We expand our studies to include more arbitrary

polymer sequences in Chapter 3, and the concept of sequence control in the self-coacervation of polyampholytes in Chapter 4. In Chapter 5, we discuss how the identity of different salts can alter the thermodynamics of complex coacervation. Throughout this work, our experimental efforts are supported by simulation and theory in collaboration with Prof. Charles Sing's group at the University of Illinois at Urbana Champaign. This combination of efforts has allowed us to have a deeper understanding of the underlying physics, and develop more comprehensive design principles for the role of chemical sequence in complex coacervation.

CHAPTER 2

SEQUENCE AND ENTROPY-BASED CONTROL OF COMPLEX COACERVATES*

2.1 Abstract

Biomacromolecules rely on the precise placement of monomers to encode information for structure, function, and physiology. Efforts to emulate this complexity via the synthetic control of chemical sequence in polymers are finding success; however, there is little understanding of how to translate monomer sequence to physical material properties. Here we establish design rules for implementing this sequence-control in materials known as complex coacervates. These materials are formed by the associative phase separation of oppositely charged polyelectrolytes into polyelectrolyte dense (coacervate) and polyelectrolyte dilute (supernatant) phases. We demonstrate that patterns of charges can profoundly affect the charge–charge associations that drive this process. Furthermore, we establish the physical origin of this pattern-dependent interaction: there is a nuanced combination of structural changes in the dense coacervate phase and a 1D confinement of counterions due to patterns along polymers in the supernatant phase.

* Part of this work has been published: L.W. Chang, T.K. Lytle, M. Radhakrishna, J.J. Madinya, J. Vélez, C.E. Sing, S.L. Perry, *Sequence and Entropy-Based Control of Complex Coacervates*, Nature Communications, (2017), **8**, 1273, DOI: 10.1038/s41467-017-01249-1.

2.2 Introduction

Polymer properties follow primarily from their one-dimensional nature, with their length distinguishing them from other soft materials. This length is due to the end-to-end connection of monomer units; the precise sequence of these monomers is capable of encoding information along the backbone.[75,76] However, interactions between these long chains are typically described in synthetic polymers by coarse-grained effective interactions between immediate neighboring molecules.[77] Polymer physics relies on the use of the these interactions, described by a parameter χ, which has its origins in average, pairwise, short-range interactions.[77,78] Biological materials, however, use a richer array of polymer–polymer interactions where this sort of 'averaging' may obscure relevant physical properties[79] and limit our ability to understand the complicated biological structure–function relationships encoded at the molecular level. The use of charge in sequence-controlled biopolymers is ubiquitous.[8,80,81] For example, charge sequence is shown to dictate the conformational behavior of intrinsically disordered proteins (IDPs),[9] and theoretical work has similarly connected IDP sequence to charge-driven phase separation.[82] Sequence is correspondingly a key aspect of intracellular compartmentalization via membrane-less organelles6.

While solid-phase synthesis methods[83,84] have long been used to prepare sequence-controlled polymers, recent advances in synthetic polymer chemistry have expanded the palette of sequence-defined polymerization methods.[75,76,85–87] For instance, advances in chemical synthesis have enabled the evaluation of precise charge spacing effects in ionomers.[47,88] However, a general understanding of the physics of sequence-defined polymer materials remains underdeveloped.

Initial efforts have begun to elucidate how monomer sequence physically influences polymer material properties. In particular, the continuum of behaviors between block and random co-polymers has been probed in terms of equilibrium properties (*e.g.*, phase behavior,[44,89] compatibilization[46]) using coarse-grained modeling and theory. These works consider portions of a vast sequence parameter space, using monomer sequence correlations (*i.e.*, blockiness),[44,89]

sophisticated machine learning methods,[46] or sequence gradients.[45] These situations focus on short-range dispersive interactions, where monomers interact primarily with their immediate neighbors. Charge interactions differ from short-range interactions, leading to different types of design rules; this difference can be tied to both the long-range nature of electrostatic interactions, and the complementarity between positive and negative charges suppressing like interactions and promoting partner interactions.

In this chapter, we demonstrate that sequence specificity of charged monomers can be used to precisely control the self-assembly and thermodynamics of a class of materials known as complex coacervates.[17,68] Charge-based sequence control allows for dramatic modulation of polymer–polymer interaction strengths without changing the overall monomer composition. We experimentally and computationally demonstrate the effects of charge patterning, and establish the physical picture and design rules necessary to show why charge patterning has such a profound effect on coacervate phase behavior.

2.3 Materials and Methods

2.3.1 Materials

Abbreviations for reagents are as follows: tert-butoxycarbonyl (Boc); 9-fluorenylmethoxylcarbonyl (Fmoc); t-butyl (tBu); trifluoroacetic acid (TFA); triisopropylsilane (TIPS); N,N-dimethylformamide (DMF); dichloromethane (DCM); N,N-diisopropylcarbodiimide (DIC); lysine (Lys or K); glutamate (Glu or E); glycine (Gly); ethyl (hydroxyimino)cyanoacetate (Oxyma).

Sequencing grade DMF, GC/MS grade DCM, TFA, ethyl ether anhydrous (BHT stabilized), methanol and acetonitrile (HPLC grade) were purchased from Fisher Scientific. Piperidine, α-cyano-4-hydroxycinnamic acid, isopropanol (99%) was purchased from Sigma Aldrich. DIC (99%), TIPS (98%) was purchased from Acros Organics. Rink amide MBHA resin

(loading level 0.32 mmol/g), Fmoc-*L*-Lys(Boc)-OH, Fmoc-*D*-Lys(Boc)-OH, Fmoc-*L*-Glu(tBu)-OH, Fmoc-*D*-Glu(tBu)-OH, Fmoc-Gly-OH, Oxyma were all purchased from Peptide Solutions, LLC. Contrad 70 was purchased from Decon Labs, Inc. All water was dispensed from a Milli-Q water purification system at a resistivity of 18.2 MΩ.cm

2.3.2 Peptide Synthesis

Polypeptides were prepared using standard Fmoc-based solid-phase synthesis on a Liberty Blue automated microwave peptide synthesizer from CEM, Ltd.[90] Deprotection and coupling were performed under microwave irradiation on a Rink amide MBHA resin with 0.2 M Fmoc and Boc protected lysine (Fmoc-*L*-Lys(Boc)-OH, Fmoc-*D*-Lys(Boc)-OH), Fmoc and tBu protected glutamate (Fmoc-*L*-Glu(tBu)-OH, Fmoc-*D*-Glu(tBu)-OH), and Fmoc protected glycine (Fmoc-Gly-OH) in DMF. 20% piperidine in DMF was used for Fmoc deprotection. DIC and Oxyma at a 0.5 M and 1 M concentration in DMF were used as activator and base, respectively.

Cleavage from the resin and side-chain deprotection was performed using 10 mL of TFA/water/TIPS in the ratio of 95/2.5/2.5 for 3 hours at room temperature while bubbling with carbon dioxide The cleaved product and resin were separated by filtration. The crude peptide was then precipitated into 40 mL of cold (stored at -80°C) anhydrous ethyl ether. The mixture was then centrifuged for 5 min at 5,000 rpm (Sorvall Legend X1R Centrifuge, Thermo Fisher Scientific, Inc.). The supernatant was decanted and a second round of precipitation and centrifugation was performed. The crude product was then dried *in vacuo* in a desiccator overnight.

Characterization of the final product was performed via a Bruker UltrafleXtreme (Fremont, CA, USA) matrix-assisted laser desorption/ionization time of flight mass spectrometery (MALDI-TOF). Samples of the peptide were mixed with matrix solution (approximately 50 mg/mL of α-cyano-4-hydroxycinnamic acid dissolved in 1:1 mixture of water and acetonitrile with 0.05% TFA) in 1:1 ratio to reach a final concentration of approximately 7.5 mM peptide.

Poly(glutamate) with degree of polymerization $N = 50$ was synthesized using amino acids of alternating chirality (*D* and *L*) to mitigate inter-peptide hydrogen bond formation.[23,91,92] Sequence-defined poly(lysine-co-glycine) peptides were synthesized with a degree of polymerization $N = 50$. Thus, all peptides include the charge-patterned blocks of 48 amino acids described by the block size τ, and are capped on each terminus by a single amino acid (K or G, Table 2.1). For $\tau = 16$, the lysine portions of the peptide were synthesized using amino acids of alternating chirality (*D* and *L*) to mitigate inter-peptide hydrogen bond formation.[23,91,92] This use of alternating chirality was only implemented for the longest block size because of the tendency for complexing peptides to form β-sheets when a continuous run of more than 7-8 chiral amino acids is present.[23,92]

Table 2.1. Molecular sequence for poly(lysine-co-glycine) peptides with degree of polymerization $N = 50$.

Block Size	Polypeptide Sequence
$\tau = 2$	$(KG)_{25}$
$\tau = 4$	$G(KKGG)_{12}K$
$\tau = 8$	$G(K_4G_4)_6K$
$\tau = 16$	$G(K_8G_8)_3K$

2.3.3 Coacervate Preparation

Polypeptide stock solutions were prepared gravimetrically using Milli-Q water at a concentration of 10 mM with respect to the total number of amino acids. For the case of the poly(lysine-co-glycine), 10 mM with respect to the total number of amino acids corresponds to 5 mM with respect to the number of charged monomers present in solution. All solutions were adjusted to pH = 7.0 using concentrated solutions of HCl and NaOH, as needed. Monomer

concentration was chosen as the experimental basis in order to easily enable direct stoichiometric comparison of the number of positively and negatively charged units present in solution, regardless of pH. A stock solution of NaCl was prepared gravimetrically at a concentration of 2 M and adjusted to pH = 7.0, as above.

Complexation was performed using stoichiometric quantities of positively and negatively charged polypeptides at a total charged residue concentration of 1 mM, 5 mM, and 50 mM at pH 7.0. Under these conditions, it is a reasonable approximation to describe all of the residues on both polypeptides as fully charged. Samples were prepared by first mixing a concentrated solution of NaCl with MilliQ water in a microcentrifuge tube (1.5 mL, Eppendorf), followed by the polyanion. The resulting mixture was then vortexed for 5 s before addition of the polycation (2 times of the volume as the polyanion to reach the charged balance between positively and negatively charged residue) to a final volume of 120 mL. The final mixture was vortexed for at least 15 s immediately after the addition of polycation to ensure fast mixing. The resulting phase separation causes the sample to take on a cloudy, or opalescent appearance, due to the formation of small droplets of the complex coacervate phase. Samples were then pipetted in triplicate into 384-well plates (FALCON, Corning, Inc.) with 32 μL per each well for subsequent analysis.

We also examined the effect of solvent dielectric by preparing samples at 1 mM total charged residue concentration in a 45/55 v/v% mixture of isopropanol and water (Figure 2.1). Sample preparation and analysis was the same as described above, except that the mixture of isopropanol and water were combined first, followed by salt, and the various polypeptide solutions.

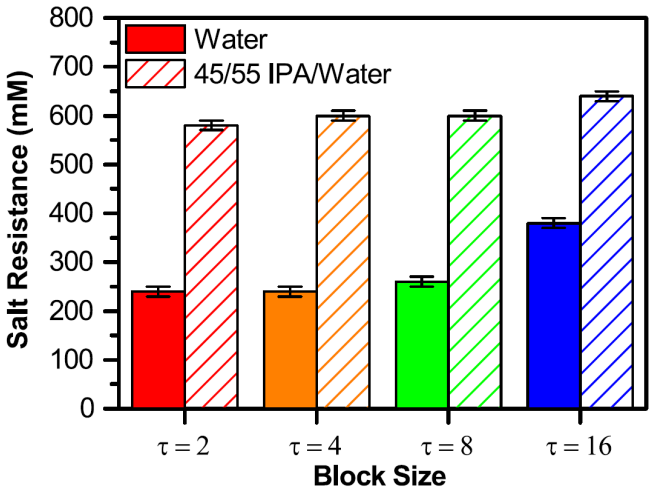

Figure 2.1. The salt resistance for sequence-defined coacervates at 1 mM charged monomer concentration in both water and a 45/55 v/v% mixture of isopropanol (IPA) and water.

2.3.4 Turbidimetry and Optical Microscopy

A plate reader equipped with a UV spectrophotometer (Synergy H1, BioTek, Inc.) was employed at a wavelength of 562 nm for the turbidity measurements. None of the polymers absorb light at this wavelength; thus, turbidity is due to light scattering from suspended coacervate droplets. The turbidity is defined by $-\ln(I/I_0)$, with I_0 = incident light intensity and I = intensity of light passed through the sample volume. Turbidity was used to estimate the salt resistance for a given sample. Direct examination of samples via optical microscope (EVOS XL Core, Fisher Scientific) was then used to confirm the salt resistance as the salt concentration above which no phase separation occurs. All samples were imaged within 1 h of preparation.

2.3.5 Isothermal Titration Calorimetry (ITC)

ITC experiments were performed at 25°C on a MicroCal Auto-iTC200 system (Malvern Instruments, Ltd.) All experiments were performed by injecting a 5 mM solution of the charge-patterned polycation (with respect to the number of lysines) into the sample cell containing 0.625 mM polyanion (with respect to the number of glutamates). Both solutions were prepared at a salt concentration of 25 mM NaCl and pH = 7.0 so as to minimize interference associated with heats of

dilution. An initial injection of 0.5 μL was performed, followed by 3 injections of 2 μL each, 24 injections of 1 μL each, and then 4 injections of 2 μL each. This injection protocol was chosen to sample the various regions of the titration curve. An injection duration of 2 s followed by a 180 s equilibration time was used. Constant stirring speed is applied at a rate of 1000 rpm. All experiments were performed in triplicate.

The heat of dilution associated with injection of the charged-patterned polycation into the sample cell was measured in a separate reference experiment performed under identical conditions (pH = 7.0, 25 mM NaCl), in the absence of polyanion in the cell. The measured heats of dilution were very small and were neglected in the subsequent data analysis.

Following each experimental run, a rigorous cleaning procedure was implemented. To clean the sample cell, the empty cell was briefly allowed to soak in a solution of 10% Contrad 70 detergent in water at 25°C. The pipette was cleaned by rinsing with water and methanol, followed by a drying step. Finally, the transfer tubing was cleaned with detergent, water, and methanol, followed by a drying step.

Analysis of ITC data was performed using the method reported previously by Priftis *et al.*[4]

2.3.6 ITC Data Analysis of Complex Coacervation

2.3.6.1 List of Variables

- V_o – Volume of the cell (in units of µL, assume 200 µL for the ITC-200 and 1440 µL for the VP-ITC)
- ΔV – The volume injected into the cell, also representing the excess volume added to the cell (in units of µL)
- C_{inj} – Concentration of the solution in the syringe (in units of mM)
- C_{cell} – Concentration of the solution in the cell (in units of mM)

- X_t – Concentration of the material injected by the syringe that is now in the cell (in units of mM)
- X_t^o – Hypothetical concentration of the material injected by the syringe that is now in the cell if dilution effects could be ignored (in units of mM)
- $[X]$ – Concentration of injectant not complexed during ion pairing (units of mM)
- M_t – Concentration of the material originally in the cell after dilution by injection from the syringe (in units of mM)
- M_t^o – Concentration of the material in the cell at the beginning of the experiment (in units of mM)
- $[M]$ – Concentration of the material in the cell not complexed during ion pairing (units of mM)
- $[MX]$ – Concentration of the ion paired material in the cell (units of mM)
- *ratio* – The molar ratio of material from the syringe compared to material in the cell
- k_{on} – The reaction rate for the formation of ion pairs (units of L/mmol-s or $mM^{-1}s^{-1}$)
- k_{off} – The reaction rate of ion pair dissociation (units of s^{-1})
- K_a – Association binding constant (units of L/mmol, or mM^{-1})
- n_{IP} – The stoichiometry for the ion pairing step
- n_{coac} – The stoichiometry for the coacervation step
- Θ_{IP} – The fraction of sites involved during ion pairing
- Θ_{coac} – The fraction of sites involved in coacervation
- ΔH_{IP} – The characteristic change in enthalpy due to ion pairing (units of kJ/mol)

- ΔH_{coac} – The characteristic change in enthalpic due to coacervation (units of kJ/mol)
- Q_{IP} – The heat associated with ion pairing (units of kJ/mol)
- Q_{coac} – The heat associated with coacervation (units of kJ/mol)
- ΔQ_{IP} – The change in heat associated with ion pairing (units of kJ/mol)
- ΔQ_{coac} – The change in heat associated with coacervation (units of kJ/mol)
- f – The fractional composition of titrant added to the mixture
- f_{coac} – The fractional composition of the mixture at maximum coacervate formation
- α_{coac} – A parameter describing the full-width, half-maximum for a Gaussian curve
- ΔG_{IP} – The characteristic change in Gibbs free energy due to ion pairing (units of kJ/mol)
- ΔS_{IP} – The characteristic change in entropy due to ion pairing (units of kJ/mol-K)
- T – Temperature (units of K)

2.3.6.2 Initial Data Analysis by MicroCal

Raw ITC data is in the form of the volume of material injected into the cell and the resultant power output in terms of μcal/injection. Given the volume of the cell (V_o), the volume of injectant added to the cell (ΔV), and the concentration of the solutions in the cell (C_{cell}) and in the syringe (C_{inj}) we can calculate all of the necessary parameters for data analysis.

The ITC cell itself is assumed to have a volume (V_o), which is completely full at the beginning of the experiment. A volume (ΔV) is added via injection from the syringe, and represents the excess volume of liquid that has overflowed the cell into the inactive communication tube where it does not participate further in the calorimetry experiment (Figure 2.2)

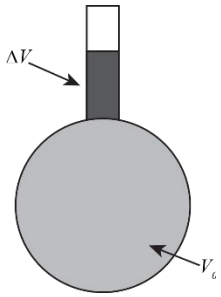

Figure 2.2. Schematic of the ITC cell geometry. Figure adapted from the iTC-200 manual.

To begin with, it is necessary to calculate the concentration of the material injected by the syringe into the cell (X_t). For an injection (ΔV), the hypothetical concentration of injectant in the cell (X_t^o) is defined by the concentration of solution in the syringe and the characteristic volumes. This value is equal to the actual number of moles of injectant, modified by the number of moles of injectant lost into the overflow volume. Rather than using a straight mole balance, the MicroCal manual describes the concentration in the overflow volume as the average between the starting concentration of the injectant in the cell (which is zero) and the hypothetical concentration.

$$X_t^o V_o = X_t V_o + \frac{1}{2} X_t^o \Delta V \tag{2.1}$$

Where

$$X_t^o = \frac{C_{inj} \Delta V}{V_o} \tag{2.2}$$

Rearranging Eq. (2.1) gives an expression for X_t.

$$X_t = \frac{C_{inj} \Delta V}{V_o} \left(1 - \frac{\Delta V}{2V_o} \right) \tag{2.3}$$

Analysis of the units in Eq. (2.3) shows that X_t has the same units of concentration (mM) as does C_{inj}.

A similar analysis must be performed to determine the concentration of the species originally present in the cell (M_t) as it changes because of dilution from the injected volumes. In

this case, M_t^o represents the concentration of material present in the cell at the beginning of the experiment and M_t is the concentration of material after the addition of injectant. As above, the amount of material lost into the excess volume is calculated based on an average concentration between M_t and M_t^o.

$$M_t^o V_o = M_t V_o + \frac{1}{2}\left(M_t + M_t^o\right)\Delta V \tag{2.4}$$

Rearranging Eq. (2.4) gives an expression for M_t.

$$M_t = M_t^o \left(\frac{1 - \frac{\Delta V}{2V_o}}{1 + \frac{\Delta V}{2V_o}} \right) \tag{2.5}$$

The units of M_t are the same as M_t^o, and are concentration (mM).

The molar ratio of the injected species to that originally in the cell can thus be calculated from the values for X_t and M_t.

$$ratio = \frac{X_t}{M_t} \tag{2.6}$$

We then need to convert the experimentally measured heat values to enthalpies on a per mole basis. This is done by multiplying the measured enthalpy per injection by the volume of the injection and the concentration of the injectant and including unit conversions.

$$\frac{Enthalpy}{V_{inj} C_{inj}} \left(\frac{kJ}{mole} \right) \tag{2.7}$$

$$\left[= \right] \left(\frac{\mu cal}{injection} \right) \left(\frac{injection}{\mu L} \right) \left(\frac{L}{mmoles} \right) \left(\frac{10^6 \mu L}{L} \right) \left(\frac{10^3 mmoles}{moles} \right) \left(\frac{10^{-9} kJ}{0.23885 \mu cal} \right)$$

2.3.6.3 Two-Step Model for Complex Coacervation

2.3.6.3.1 Step One: Ion Pairing

Having obtained the data from the ITC instrument in a usable form, we now look to model coacervation as a two-step process. The first step, termed "Ion Pairing" is thought to involve the electrostatic complexation of soluble polyelectrolyte chains. The resulting "ion pair" remains in solution and exhibits both enthalpy associated with the chain complexation and entropy associated with the release of bound counterions. This step is modeled using the "Single Set of Identical Sites" model from MicroCal. We begin by defining the complexation reaction:

$$X + M \underset{k_{off}}{\overset{k_{on}}{\rightleftharpoons}} XM \tag{2.8}$$

Where the association binding constant (K_a) is defined as:

$$K_a = \frac{k_{on}}{k_{off}} = \frac{[MX]}{[M][X]} \tag{2.9}$$

where [M], [X], and [MX] are the concentrations of the unbound species in the cell and syringe, and the concentration of the ion paired complex, respectively.

However, only the total concentrations X_t and M_t are known. We must therefore eliminate [M], [X], and [MX] from our expressions. A total mole balance for both M and X, taking into account the stoichiometry of X binding to M (n_{IP}) gives:

$$X_t = [X] + n_{IP}[MX] \tag{2.10}$$

$$M_t = [M] + [MX] \tag{2.11}$$

We can also define the fraction of sites on M that are bound in an ion pair (Θ_{IP}).

$$\Theta_{IP} = \frac{[MX]}{M_t} \tag{2.12}$$

Combining Eqs. (2.11) and (2.12) we can write

$$[M] = M_t\left(1 - \Theta_{IP}\right) \tag{2.13}$$

Similarly, combining Eqs. (2.10) and (2.12) we obtain

$$[X] = X_t - n_{IP}\Theta_{IP}M_t \tag{2.14}$$

Rearranging Eq. (2.12) gives us an expression for the remaining unknown parameter, [*MX*]

$$[MX] = \Theta_{IP}M_t \tag{2.15}$$

Finally, substituting the expressions from Eqs. (2.13) and (2.15) into the expression for the association binding constant Eq. (2.9) gives

$$K_a = \frac{\Theta_{IP}}{(1-\Theta_{IP})[X]} \tag{2.16}$$

Further including Eq. (2.14) allows for the creation of an equation where the only unknown is Θ_{IP}.

$$K_a = \frac{\Theta_{IP}}{(1-\Theta_{IP})(X_t - n_{IP}\Theta_{IP}M_t)} \tag{2.17}$$

Expanding the quadratic and gathering terms we obtain

$$\Theta_{IP}^2 - \Theta_{IP}\left(1 + \frac{X_t}{n_{IP}M_t} + \frac{1}{K_a n_{IP}M_t}\right) + \frac{X_t}{n_{IP}M_t} = 0 \tag{2.18}$$

Solving this expression for Θ_{IP} gives

$$\Theta_{IP} = \frac{1}{2}\left[1 + \frac{X_t}{n_{IP}M_t} + \frac{1}{K_a n_{IP}M_t} - \sqrt{\left(1 + \frac{X_t}{n_{IP}M_t} + \frac{1}{K_a n_{IP}M_t}\right)^2 - \frac{4X_t}{n_{IP}M_t}}\right] \tag{2.19}$$

The choice of this solution for Θ_{IP} is straightforward because it provides the only physically meaningful answer (at low X_t and M_t the value of Θ_{IP} is small and asymptotically approaches 1 at large X_t and M_t.

The total heat content Q_{IP} of the solution in the cell (determined relative to zero for the unbound species) at a fractional saturation of Θ_{IP} and using a characteristic change in enthalpy for ion pairing (ΔH_{IP}) is:

$$Q_{IP} = \frac{n_{IP}\Theta_{IP}M_t\Delta H_{IP}V_o}{C_{inj}\Delta V} \tag{2.20}$$

which has units of kJ/mol.

$$Q_{IP}[=]\left(\frac{mmoles}{L}\right)\left(\frac{kJ}{mole}\right)\left(\frac{\mu L}{}\right)\left(\frac{L}{mmoles}\right)\left(\frac{}{\mu L}\right) \tag{2.21}$$

Substituting Eq. (2.19) into Eq. (2.20) gives the full expression for the molar heat of ion pairing.

$$Q_{IP} = \frac{n_{IP}M_t\Delta H_{IP}V_o}{2C_{inj}\Delta V}\left[1+\frac{X_t}{n_{IP}M_t}+\frac{1}{K_a n_{IP}M_t}-\sqrt{\left(1+\frac{X_t}{n_{IP}M_t}+\frac{1}{K_a n_{IP}M_t}\right)^2-\frac{4X_t}{n_{IP}M_t}}\right] \tag{2.22}$$

However, in modeling our experimental data we are interested in the change in heat from one injection to the next (ΔQ_{IP}). This calculation requires consideration of the values for Q_{IP} and ΔV after the i^{th} injection. We are also only considering the heat effects within the cell volume V_o, necessitating the inclusion of a correction term as in Eqs. (2.1) and (2.4).

$$\Delta Q_{IP}(i) = Q_{IP}(i) - Q_{IP}(i-1) + \frac{\Delta V}{V_o}\left(\frac{Q_{IP}(i)+Q_{IP}(i-1)}{2}\right) \tag{2.23}$$

2.3.6.3.2 Step Two: Complex Coacervation

Following the formation of soluble "ion pairs," we now describe a second step where a molecular rearrangement occurs, allowing the soluble ion pairs to aggregate and undergo phase separation to form the separate liquid coacervate phase. For this step we assume that the additional heat contribution to the system (Q_{coac}) is proportional to the amount of polymer present in the coacervate domains at a given composition. We define

$$Q_{coac} = \frac{n_{coac}\Theta_{coac}M_t\Delta H_{coac}V_o}{C_{inj}\Delta V} \tag{2.24}$$

Where Θ_{coac} is arbitrarily defined by a Gaussian with respect to the molar fraction *f* of the polymer being titrated into the system over the total polymer content. This choice was made because the Gaussian shape is similar to the shape of a turbidity curve as a function of polyelectrolyte stoichiometry.

$$f = \frac{X_t}{X_t + M_t} \tag{2.25}$$

$$\Theta_{coac} = \exp\left(-\frac{\left(f - f_{coac}\right)^2}{\alpha_{coac}^2}\right) \tag{2.26}$$

The parameter f_{coac} describes the composition of the mixture at the point of maximum coacervate formation in terms of the stoichiometry of binding n_{coac}.

$$f_{coac} = \frac{n_{coac}}{1 + n_{coac}} \tag{2.27}$$

α is related to the magnitude of the full-width at half-maximum (FWHM) for the Gaussian curve.

$$FWHM = 2\alpha\sqrt{\ln(2)} \approx 1.7\alpha \tag{2.28}$$

The change in heat for the coacervation step is calculated as a difference between titration steps, as above.

$$\Delta Q_{coac}(i) = Q_{coac}(i) - Q_{coac}(i-1) + \frac{\Delta V}{V_o}\left(\frac{Q_{coac}(i) + Q_{coac}(i-1)}{2}\right) \tag{2.29}$$

2.3.6.3.3 Summary:

This two-step model is intended to be used to fit experimentally obtained data from isothermal titration calorimetry (ITC). It consists of six fitting parameters: n_{IP}, n_{coac}, ΔH_{IP}, ΔH_{coac}, K_a, and α. Here are some suggestions for starting values for these parameters:

- n_{IP} – This corresponds to the ratio where the ion pairing transition (inflection point) occurs. This is typically near the middle of the range of ratios run for the experiment (assuming your data fills the entire range).

- n_{coac} – This corresponds to the ratio where the curve crosses the horizontal axis. All ratios below n_{coac} have a positive enthalpy change and all ratios above n_{coac} have a negative one (or visa versa). In physical terms, while adding a small amount of the injectant, you form more and more coacervate until you reach the ratio n_{coac}. After that, each injection causes the coacervate to gradually dissolve. This is also why n_{coac} is the ratio at which we observe the largest amount of coacervation formation. Typically this value is slightly higher than n_{IP}.

- ΔH_{IP} – Corresponds to the horizontal asymptote for the experimental data for the first couple of points during the titration experiment.

- ΔH_{coac} – This is a normalization value. While we would prefer to directly utilize the change in enthalpy per mole of polymer that is actually present in the coacervate phase, we have no way of determining this value. A starting guess is typically 10-20% of the value of ΔH_{IP}.

- K_a – Corresponds to the steepness of the slope of the overall curve (*i.e.*, at infinitely high K you would get a step function). Suggested starting values are in the range of 10^2 mM^{-1}.

- α – Corresponds to the width of the range over which coacervation occurs. It is directly proportional to the distance between the minimum and the maximum of ΔQ_{coac}. Typical starting value is approximately 0.02.

2.3.6.4 Analysis of Thermodynamic Parameters

The two-step model directly provides values for enthalpy of ion pairing and coacervation ($\triangle H_{IP}$, $\triangle H_{coac}$) as well as the association binding constant for the ion pairing step (K_a). From these parameters we can determine values for the Gibbs free energy ($\triangle G_{IP}$) and the entropy ($\triangle S_{IP}$) associated with ion pairing. By definition, the association binding constant is directly related to the Gibbs free energy.

$$\Delta G_{IP} = -RT\ln\left(K_a\right) \tag{2.30}$$

We can now calculate the value for the entropy ($\triangle S_{IP}$) using the definition for the Gibbs free energy.

$$\Delta G_{IP} = \Delta H_{IP} - T\Delta S_{IP} \tag{2.31}$$

$$\Delta S_{IP} = \frac{\Delta H_{IP} - \Delta G_{IP}}{T} \tag{2.32}$$

2.3.6.5 Data Analysis

Reported data are the average of three runs. An average of the last five points of each run was used to correct the baseline of each dataset. This approach assumes that the system has reached equilibrium by the end of the run, and that the observed change in enthalpy is zero.

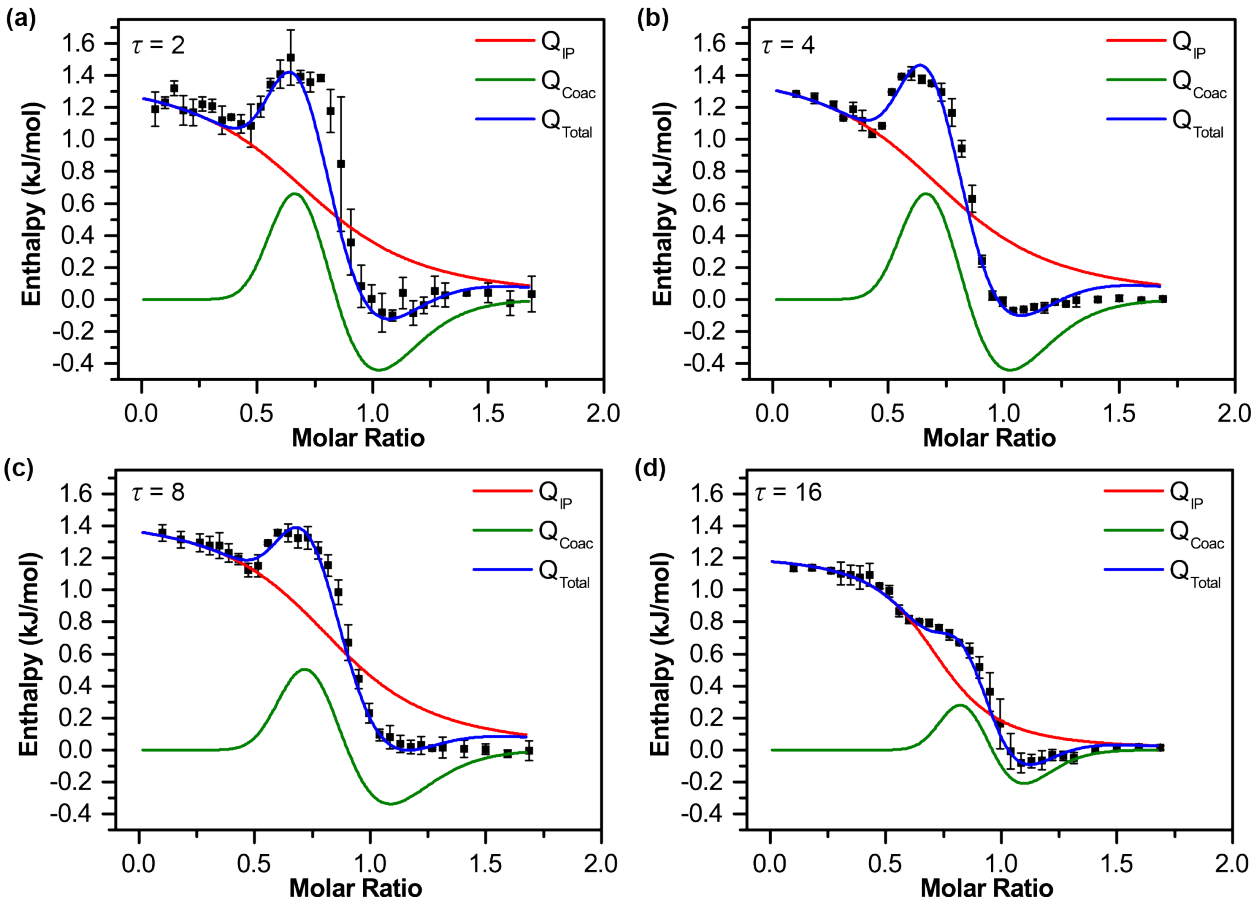

Figure 2.3. Experimental data for the molar enthalpy of complexation of sequence-patterned polypeptides in 25 mM NaCl and pH = 7.0 and the resulting fitting curves (blue line) for **(a)** τ = 2, **(b)** τ = 4, **(c)** τ = 8, and **(d)** τ = 16. The individual contributions from the ion pairing (red line) and coacervation (green line) parts of the model are shown in each graph. Values represent the average of three runs; error bars are the standard deviation.

ITC data analysis was performed in Microsoft Excel. Curve fitting to the model was performed via least-squared error minimization with six adjustable parameters (ΔH_{ip}, K_a, n_{ip}, ΔH_{coac}, α, n_{coac}) using the Solver add-on. Figure 2.3 shows the results of fitting the two-step model to our data. The single binding-site model used for the ion pairing step results in a smooth continuously decaying function (red line). The coacervation step shows the characteristic features of the derivative of a Gaussian peak, reflective of the formation and subsequent dissolution of the coacervate phase as a function of the mole ratio of the system. . shows a comparison of the data and the resulting curve fits as a function of block size.

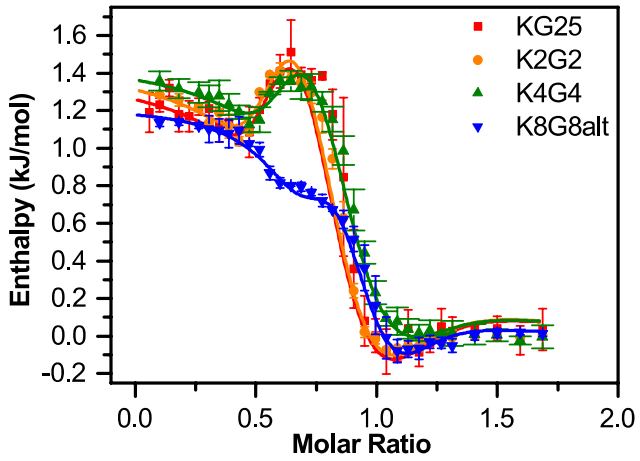

Figure 2.4. Results of curve fitting superimposed onto the raw ITC data for sequence-patterned polypeptides in 25 mM NaCl and pH = 7.0. Values represent the average of three runs; error bars are the standard deviation.

Table 2.2. Fitting parameters for ITC analysis for sequence-patterned polypeptides in 25 mM NaCl and pH = 7.0. Values represent the average of three runs. Calculated error is the result of curve fitting based on the minimum and maximum variation from the average defined by the standard deviation.

Block Size	ΔH_{ip} (kJ/mol)	K_a (L/mmol)	n_{ip}	ΔH_{coac} (kJ/mol)	α	n_{coac}
$\tau = 2$	1.38±0.074	18.5±0.11	0.80±0.014	0.196±0.0013	0.077±0.0017	0.85±0.036
$\tau = 4$	1.45±0.024	18.6±0.63	0.82±0.010	0.196±0.0010	0.077±0.0002	0.85±0.036
$\tau = 8$	1.46±0.004	25.0±0.62	0.89±0.008	0.143±0.0019	0.074±0.0009	0.90±0.011
$\tau = 16$	1.22±0.010	58.8±0.12	0.74±0.006	0.058±0.0001	0.051±0.0005	0.96±0.025

Table 2.3. Compiled thermodynamic data from ITC analysis for sequence-patterned polypeptides in 25 mM NaCl and pH = 7.0. Values represent the average of three runs. ΔH values are the sum of ΔH_{ip} and ΔH_{coac}.

Block Size	ΔH (kJ/mol)	$-T\Delta S$ (kJ/mol)	ΔG (kJ/mol)
$\tau = 2$	1.58±0.075	–25.7±0.09	–24.3±0.01
$\tau = 4$	1.64±0.025	–25.8±0.06	–24.3±0.08
$\tau = 8$	1.60±0.006	–26.4±0.06	–25.1±0.06
$\tau = 16$	1.28±0.010	–28.4±0.01	–27.2±0.01

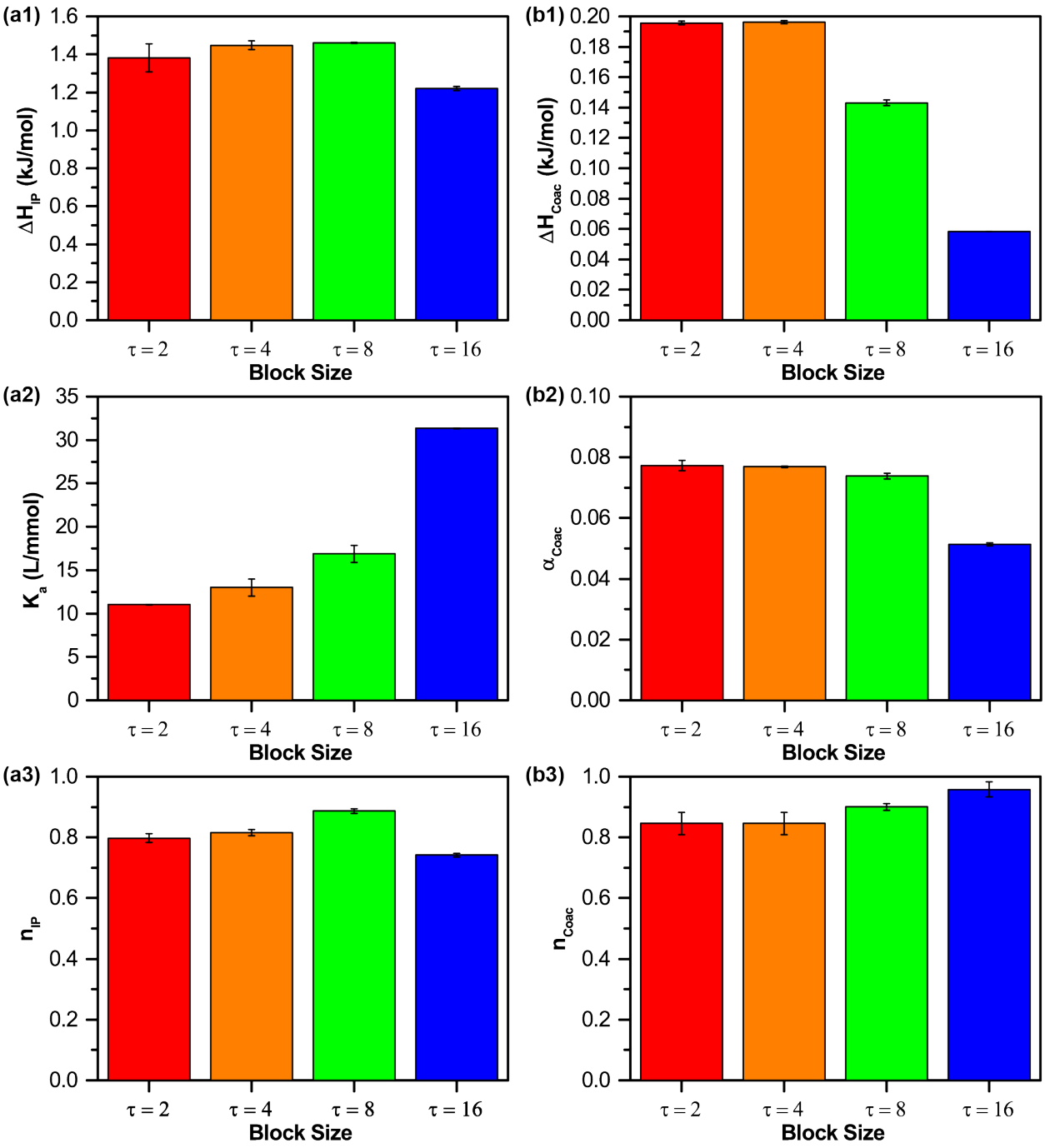

Figure 2.5. Fitting parameters from ITC analysis for the **(a)** ion pairing and **(b)** coacervation steps for sequence-patterned polypeptides in 25 mM NaCl and pH = 7.0. Values represent the average of three runs. Error bars are the result of curve fitting based on the minimum and maximum variation from the average defined by the standard deviation.

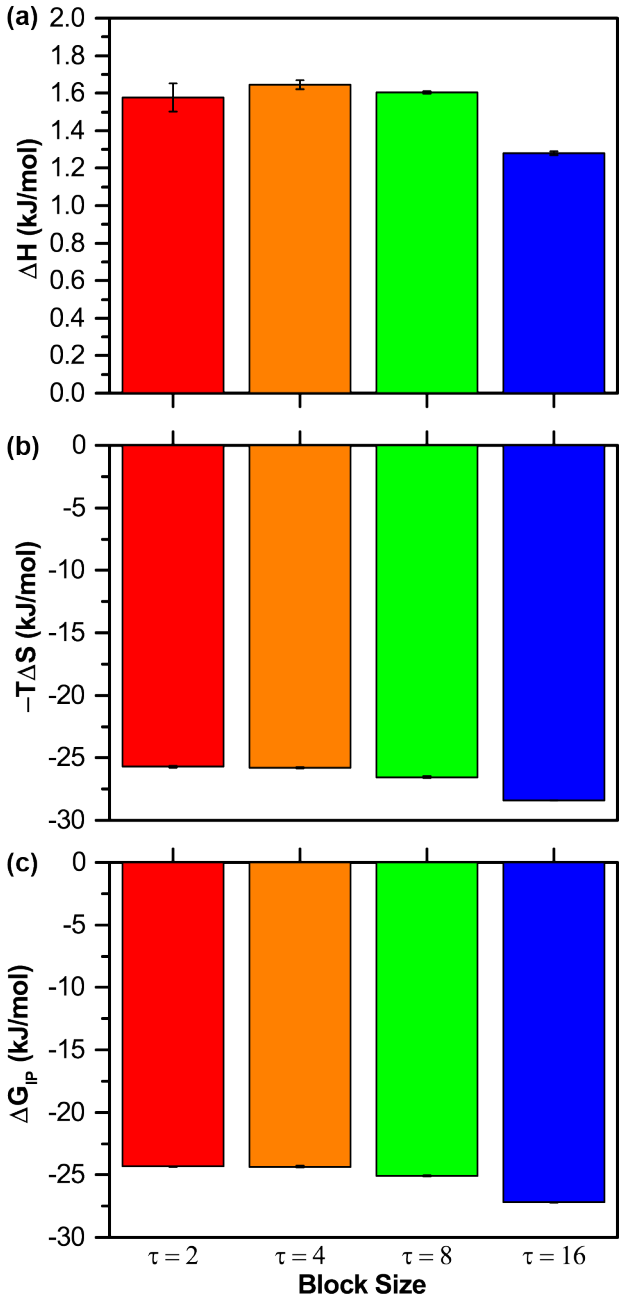

Figure 2.6. Compiled thermodynamic data from ITC data analysis for sequence-patterned polypeptides in 25 mM NaCl and pH = 7.0. Values represent the average of three runs. ΔH values are the sum of ΔH_{ip} and ΔH_{coac}.

2.3.6.6 Simulation Determination of Coacervate Phase Behavior

Our approach for simulating complex coacervation is related to methods developed in Lytle *et al.*[93] that use Monte Carlo (MC) simulations to tabulate the excess free energy, $f_{EXC}(\phi_P, \phi_S)$ as a function of polymer volume fraction ϕ_P and salt volume fraction ϕ_S. This molecularly-informed

function f_{EXC} can be incorporated into a Flory-Huggins like free energy expression, which can subsequently be used to calculate the phase behavior of the coacervation for a series of sequence-defined polycations and homopolyanions.

2.3.6.7 Restricted Primitive Model of Coacervation

MC simulations were performed in the NVT ensemble using the restricted primitive model (RPM),[94] which treats all charged species as beads that interact via hard core potentials and Coulombic interactions. Systems composed of n_{P+} polycations, n_{P-} polyanions, n_+ cations, and n_- anions at positions $\boldsymbol{r}_i$. Water is modeled as an implicit solvent with a relative dielectric constant ϵ_r = 78.5. We fix the degree of polymerization, N, to be 48 beads for all chains. Polycations are patterned with 24 neutral beads and 24 charged beads. n_{P+} is twice the value of n_{P-} to ensure the polymers are charge neutral without additional salt. Charge beads, including all salt ions and polymer charges, have a hard-core diameter $\sigma_{P+} = \sigma_{P-} = \sigma_+ = \sigma_- = 4.25$ A. Neutral beads have smaller diameters $\sigma_0 = 0.25\sigma_+$, motivated by the absence of a hydration shell that is implicitly included in the hard-core radius of the charged species in the RPM. Practically, the neutral beads' size does have a measurable effect on the magnitude of coacervate phase behavior; we have parameterized this value to match experimental and computational phase behavior.

2.3.6.8 MC Simulation of Coacervates

The MC simulation is updated based on the overall interaction energy U given by

$$U = \frac{1}{2}\sum_{i,j\neq i}^{N_{tot}}\left[U_{HS}(r_{ij}) + U_{ES}(r_{ij})\right] + \sum_{i}^{n}\sum_{j}^{N-1} U_B(r_{j,j+1}) + \sum_{i}^{n}\sum_{j}^{N-2} U_\theta(\boldsymbol{r}_j, \boldsymbol{r}_{j+1}, \boldsymbol{r}_{j+2}) \quad (2.33)$$

where $N_{tot} = N(n_{P+} + n_{p-}) + n_+ + n_-$, the total number of beads, and $n = n_{P+} + n_{p-}$ is the total number of polymer chains. $r_{ij} = |\boldsymbol{r}_i - \boldsymbol{r}_j|$ is the distance between beads i and j. The hard sphere interaction contribution, U_{HS}, is given by:

$$U_{HS}(r_{ij}) = \begin{cases} \infty \; if \; r_{ij} < (\sigma_i + \sigma_j)/2 \\ 0 \; if \; r_{ij} \geq (\sigma_i + \sigma_j)/2 \end{cases} \tag{2.34}$$

The polymer bonding potential contribution U_B is:

$$U_B(r_{ij}) = \begin{cases} 0 \;\; if \; \sigma_+ \leq r_{ij} \leq 1.1\sigma_+ \\ \infty \qquad otherwise \end{cases} \tag{2.35}$$

Here, the polymer bonds are all the same size regardless of the actual diameter of the monomer σ_i, and is set by the size of the polycation/polyanion bead. An angle potential contribution U_θ provides some stiffness for the chain:

$$U_\theta(\boldsymbol{r}_j, \boldsymbol{r}_{j+1}, \boldsymbol{r}_{j+2}) = \frac{1}{2}\kappa_\theta \theta_{j,j+1,j+2}^2 \tag{2.36}$$

where $\kappa_\theta = 3.3k_BT$ is the strength of the angle potential, k_B is the Boltzmann constant, T is the temperature, and $\theta_{j,j+1,j+2}$ is the angle between adjacent bond vectors. Finally, all charged beads interact through a Coulomb potential U_{ES}:

$$U_{ES}(r_{ij}) = \frac{q_i q_j}{4\pi\epsilon_0\epsilon_r r_{ij}} \tag{2.37}$$

where q_i is the charge on bead i, and ϵ_0 is the vacuum permitivitty. Ewald summation is used to calculate electrostatic interactions in the simulation.[95]

2.3.6.9 Widom Insertion to Calculate Free Energy Landscape

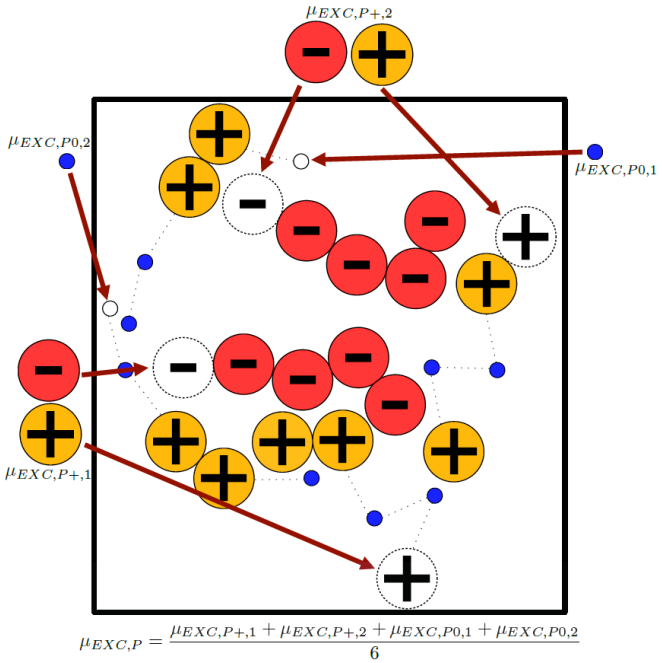

Figure 2.7. Example calculation for the polymer excess chemical potential with a $\tau = 4$ repeating pattern. Charged polycation monomers are orange, neutral polycation monomers are blue, and polyanion monomers are red. Bonds are denoted by dotted lines. Sequence- defined polycation chains are generated such that each bead in the repeating pattern is represented by a chain end. In this case, polycation chain ends correspond to the first charged bead, the second charged bead, the first neutral bead, and the second netural bead. Widom insertion is then performed on the different chain ends, and, if the inserted polycation monomer is charged then a polyanion monomer is also inserted. For this particular pattern, the four excess chemical potentials are $\mu_{EXE,P+1}$, $\mu_{EXE,P+2}$, $\mu_{EXE,P0,1}$, $\mu_{EXE,P0,2}$. These correspond to the insertion of the first charged polycation monomer with a polyanion monomer, the second charged polycation monomer with a polyanion monomer, the first neutral polycation monomer, and the second neutral polycation monomer, respectively. These excess chemical potentials are added together and divided by the total number of monomers inserted for all excess chemical potentials. This scheme can be generalized to any pattern size.

The excess chemical potentials, $\mu_{EXC,i}$ for all species $i = P+, P-, +, -, 0$ were calculated using Widom insertion.[95] Modification of the Widom insertion technique was necessary to calculate the polyelectrolytes' excess chemical potential, illustrated schematically in Figure 2.7. The polycation's pattern is shifted along the various chains in the system so each monomer in the charge pattern has representative chain ends. Widom insertion is performed on each of

the different types of chain ends, and, if the inserted polycation monomer is charged, a corresponding polyanion monomer is inserted. The chemical potentials thus calculated are added together and divided by the total number of monomers inserted for all of the chain ends. This gives each monomers' excess chemical potential. The salt excess chemical potential $(\mu_{EXC,+} + \mu_{EXC,-})/2$ was calculated by inserting a pair of oppositely-charged salt ions and halving this value, yielding the excess chemical potential for each salt ion. Thermodynamic integration of $\mu_{EXC,i}$ according to:

$$f_{EXC}(\phi_S, \phi_P) = \int_{\phi_S^0,\phi_P^0}^{\phi_S,\phi_P^0} \mu_{EXC,S}(\phi_S', \phi_P^0) d\phi_S' + \int_{\phi_S,\phi_P^0}^{\phi_S,\phi_P} \mu_{EXC,P}(\phi_S, \phi_P') d\phi_P' \quad (2.38)$$

This yields the excess free energy density, $f_{EXC}(\phi_P, \phi_S)$, as a function of ϕ_S and ϕ_P. This excess free energy density is used in a Flory-Huggins-like theory to determine the phase behavior of the system.

2.3.6.10 Phase Separation Theory

A Flory-Huggins inspired theory was developed to determine the coacervation phase diagrams. The system has an average polymer volume fraction, $\langle\phi_P\rangle$, and an average salt volume fraction, $\langle\phi_S\rangle$. At certain salt and polymer volume fractions, phase separation occurs creating a coacervate phase, α, with polymer volume fraction, $\phi_{P,\alpha}$, and salt volume fraction, $\phi_{S,\alpha}$. Coexisting with the coacervate phase is a supernatant phase, β, with polymer volume fraction $\phi_{P,\beta}$ and salt volume fraction $\phi_{S,\beta}$. Both phases are incompressible with a volume fraction of water given by $\phi_{W,i} = 1 - \phi_{P,i} - \phi_{S,i}$ where i denotes the phase. The free energy of the system is:

$$F = F_0 + F_{EXC} \quad (2.39)$$

Here, F_0 is the translational entropy contribution to the overall free energy, and F_{EXC} is the excess free energy contribution.

The entropy of mixing is given by:

$$F_0 = \frac{\Omega}{\langle\phi_P\rangle}\left\{\left[1-\frac{pN\langle\phi_P\rangle}{\Omega\phi_{P,\alpha}}\right]\left[\phi_{S,\beta}\ln\phi_{S,\beta}+\frac{\phi_{P,\beta}}{N}\ln\phi_{P,\beta}+\left(1-\phi_{P,\beta}-\phi_{S,\beta}\right)\ln\left(1-\phi_{P,\beta}-\phi_{S,\beta}\right)\right]\right.$$
$$+\frac{pN\langle\phi_P\rangle}{\Omega\phi_{P,\alpha}}\left[\left(1-\phi_{P,\alpha}-\phi_{S,\alpha}\right)\ln\left(1-\phi_{P,\alpha}-\phi_{S,\alpha}\right)+\phi_{S,\alpha}\ln\phi_{S,\alpha}\right.$$
$$\left.\left.+\frac{\phi_{P,\alpha}}{N}\ln\phi_{P,\alpha}\right]\right\} \tag{2.40}$$

Here, Ω is the total number of monomers in the system, and p is the total number of chains in the coacervate phase. The first term describes the entropy of mixing in the supernatant phase, and the second term describes the entropy of mixing in the coacervate phase. $\frac{pN\langle\phi_P\rangle}{\Omega\phi_{P\alpha}}$ gives the ratio of the coacervate phase volume to the total system volume, and $\Omega/\langle\phi_P\rangle\,\phi$ gives the total number of monomer-equivalent volumes in the system.

The excess free energy contribution is given by:

$$F_{EXC} = \frac{\Omega}{\langle\phi_P\rangle}\left\{\left[1-\frac{pN\langle\phi_P\rangle}{\Omega\phi_{P,\alpha}}\right]f_{EXC}\left(\phi_{P,\beta},\phi_{S,\beta}\right)+\frac{pN\langle\phi_P\rangle}{\Omega\phi_{P,\alpha}}f_{EXC}\left(\phi_{P,\alpha},\phi_{S,\alpha}\right)\right\} \tag{2.41}$$

Here, f_{EXC} is the excess free energy density obtained in Eq. (2.38). This allows any monomer-level features, such as the patterning to be included in the mixing enthalpy.

F is minimized with respect to $\phi_{P,\alpha}$, $\phi_{P,\beta}$, and $\phi_{S,\alpha}$. p can be calculated using $\langle\phi_P\rangle = \frac{pN\langle\phi_P\rangle}{\Omega\phi_{P\alpha}}\phi_{P,\alpha} + (1-\frac{pN\langle\phi_P\rangle}{\Omega\phi_{P\alpha}})\phi_{P,\beta}$ and the corresponding calculation for $\langle\phi_S\rangle$ can be used to calculate $\phi_{S,\beta,}$. The minimized value of F is compared to the free energy of a homogeneous state, F_{HOM}, given by:

$$F_{HOM} = \frac{\Omega}{\langle\phi_P\rangle}\left[\langle\phi_S\rangle\ln\langle\phi_S\rangle+(1-\langle\phi_P\rangle-\langle\phi_S\rangle)\ln(1-\langle\phi_P\rangle-\langle\phi_S\rangle)+\frac{\langle\phi_P\rangle}{N}\ln\langle\phi_P\rangle\right.$$
$$\left.+f_{EXC}(\langle\phi_P\rangle,\langle\phi_S\rangle)\right] \tag{2.42}$$

If the minimized value of F is less than F_{HOM}, the system undergoes phase separation to the concentration values which minimized F.

2.4 Results

2.4.1 Oppositely Charged Polymers Drive Self-assembly

Oppositely charged polyelectrolytes can undergo associative phase separation in an aqueous solution, forming a polymer-dense coacervate phase and a polymer-dilute supernatant phase.[17,68] This process is known as complex coacervation, which broadly describes any liquid–liquid phase separation due to oppositely charged species. Recent experimental work into the fundamental physics of polymer–polymer coacervation[3,11,20,27] is motivated by efforts to use this motif to drive self-assembly.[53,56,96–99] Similarly, advances in coacervate theory have led to a range of field theoretic[100–103] and phenomenological[104–107] models of coacervation.[108,109]

Figure 2.8a schematically illustrates a standard complex coacervate phase diagram, in the space spanned by salt concentration c_S and polymer concentration c_P. At low salt and polymer concentrations, in the coexistence region (2Φ) underneath the binodal curve, the system spontaneously undergoes a phase separation into the high-c_P coacervate phase and the low-c_P supernatant phase. The coacervate and supernatant states are connected along a tie line, which is sloped to denote a difference in c_S between the two phases. Beyond the coexistence region, the system becomes completely miscible. Previous work has demonstrated that this phase diagram is extremely sensitive to molecular-level structure.[72,110] Changes in bond length and charge size can drastically expand or shrink the coexistence region, reflecting differences in local charge correlations that arise between the highly connected, oppositely charged polyelectrolytes.[72] However, it is difficult to experimentally demonstrate these effects in a controllable fashion. Instead, changing charge monomer sequence provides both a way to experimentally observe the interplay

between electrostatics and molecular structure, and enables the sequence-driven design of coacervate-based materials.

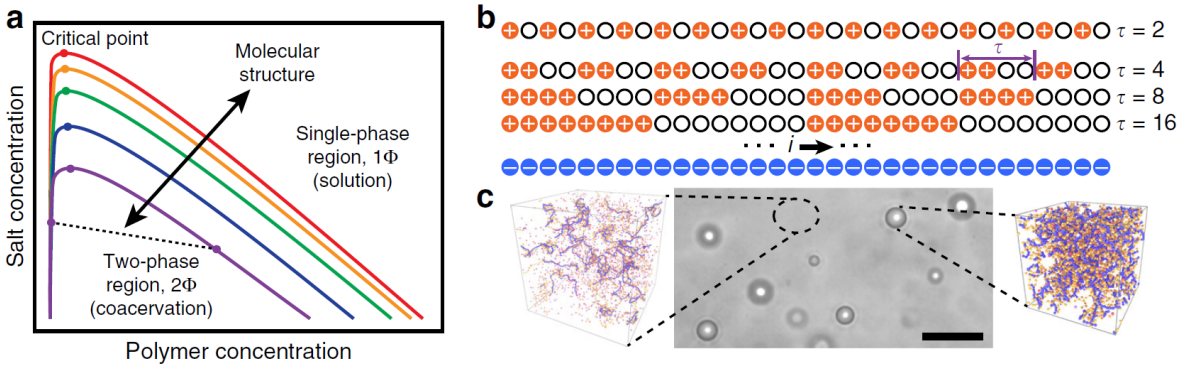

Figure 2.8. Molecular structure and sequence affects charge-driven phase separation. **(a)** Qualitative sketch of a typical phase diagram of complex coacervate-forming polyelectrolytes. Coacervation occurs at low salt and polymer concentrations, where oppositely charged polyelectrolytes undergo a liquid-liquid phase separation into polymer dense (coacervate) and polymer-dilute (supernatant) phases. The different curves qualitatively represent how the immiscible region changes with different molecular features (charge monomer sequence, spacing, ion size, degree of polymerization, valency, etc.). **(b)** We show that charge monomer sequence is a molecular feature, which can be used to tune coacervation behavior. This simulation and experimental result is based on coacervation between a homopolyanion and a series of model, sequence-defined polycations with half of their monomers charged. These polycations are characterized by the periodic repeat of the monomer sequence, τ. **(c)** Coacervation is experimentally observed as droplets of a polymer-dense 'coacervate' dispersed in a polymer-dilute 'supernatant' phase. Simulation images correspond to conditions (salt concentration, 25 mM and τ = 2) shown in Figure 2.9. Scale bar is 25 μm.

2.4.2 Tuning Molecular Interactions via Patterning

We use the 1D pattern of charged monomers along a polymer backbone to controllably tune the local arrangement of charges, and thus the strength of charge interactions between coacervate-forming chains. Experimentally, we consider coacervation between an anionic homopolymer of poly(glutamate) and sequence-specific cationic co-polymers of poly(glycine-co-lysine). These are prepared in aqueous solution with NaCl salt at pH 7.0. All polymers have the same degree of polymerization $N = 50$; because the sequence-specific polycations have a charge monomer fraction of $f = 0.5$, there are twice as many polycation molecules as polyanion molecules to balance the number of charges on these species.

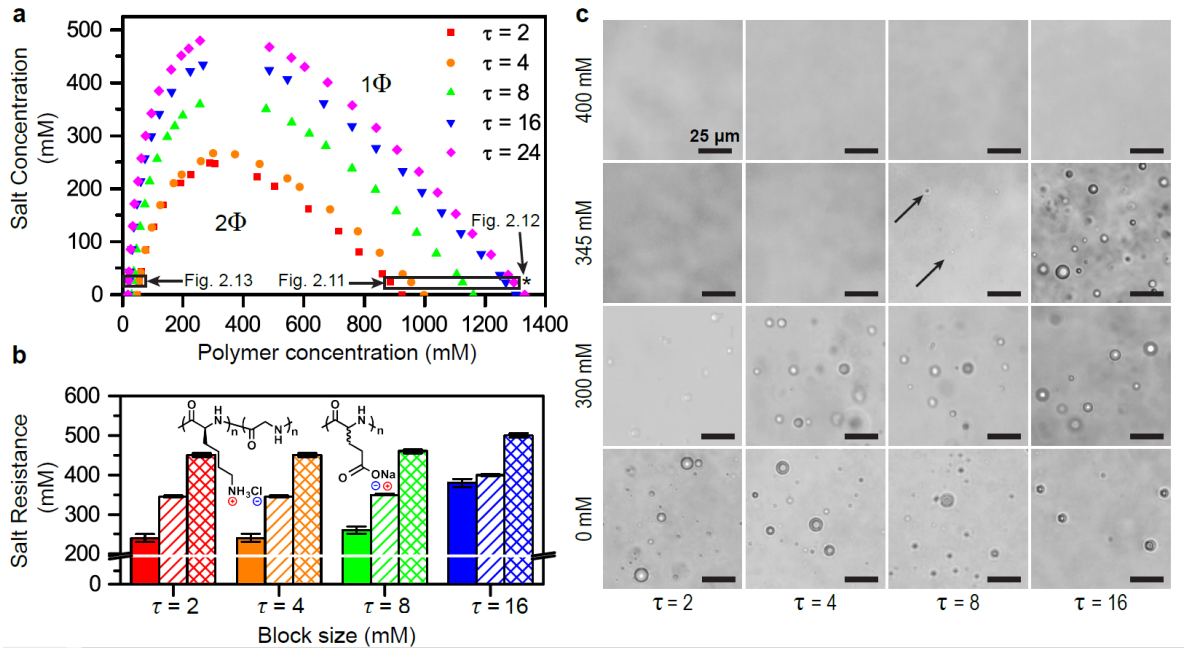

Figure 2.9. Coacervate phase behavior is affected by charge sequence in both simulation and experiment. **(a)** Simulations demonstrate that the size of the coexistence region 2Φ increases with τ. Simulation conditions for Figure 2.11–2.13 are specified by asterisks/boxes, which denote points along the binodal curves at 25 mM NaCl. These points are considered, because the salt concentration values correspond to those used for isothermal titration calorimetry. **(b)** The experimental salt resistance for sequence-defined coacervates at a variety of total charged monomer concentrations (solid 1 mM, stripes 5 mM, crosshatch 50 mM), plotted as a function their periodic block size (τ = 2 to τ = 24). Increasing τ leads to a marked increase in the salt resistance, qualitatively changing by as much as 50–150 mM, consistent with simulations in **(a)**. Error bars reflect the intervals between samples in these experiments. **(c)** A selection of optical micrographs corresponding to the data in **(a)**, highlighting that the region of coacervation increases with τ. Arrows indicate the presence of tiny coacervate drops. Scale bars are 25 μm.

In simulation, a restricted primitive model (RPM) representation is used for the polyelectrolytes and salt.[94] RPM coarse-grains atomistic features of charged systems, representing each species i as beads (salt) or connected beads (polymer) with hard core potentials of radius a_i and a charge of z_i. Water is a continuum solvent with dielectric constant $\epsilon = 78.5\epsilon_0$. There are well-established limitations to RPM, which does not account for Hofmeister effects or water structure;[111] however, RPM still accounts for the major trends seen in this chapter. See the Methods (Section 2.2) for a detailed description of the model. Figure 2.8 demonstrates our scheme for the homopolyanion and sequence-specific copolycation. The homopolyanion and copolycation both

consists of chains of N = 48; similar to experiment, twice as many polycations are present per polyanion. Copolycation sequences for both simulation and experiment are defined by their periodicity τ. A copolycation with a sequence that alternates between charged and neutral monomers would have a value τ = 2, while a copolycation that has eight charged monomers followed by a block of eight neutral monomers has a periodicity τ = 16 (Figure 2.8b). For all sequences, the copolycation has the same number of charged and neutral monomers.

Figure 2.9a shows the coacervation phase diagrams for a series of patterned copolycations interacting with unpatterned homopolyanions, calculated from simulation. These phase diagrams exhibit a drastic, monotonic increase in the size of the coexistence region. In fact, the salt resistance nearly doubles from τ = 2 to τ = 24. Changes in the size of the coexistance region determined from simulation are reflected experimentally by trends in salt resistance as a function of τ at a constant polymer concentration, (Figure 2.9b,c) with qualitative agreement. While matching between the simulation and experimental results is in part dependent on the choice of simulation parameters such as bead radii, the trend observed here persists regardless of the choice of reasonable parameterization values. We note that this effect persists even when the solvent is changed, with a similar effect of τ on the salt resistance in a water/isopropanol solvent mixture (Figure 2.1).

2.4.3 Thermodynamics of Sequence-defined Coacervation

We use isothermal titration calorimetry (ITC) as a tool to experimentally probe the thermodynamics of complex coacervation (Figure 2.10a).[112] A two-step model of coacervation enables analysis of ITC data and its separation into entropic and enthalpic contributions; 'ion pairing' between oppositely charged polymers is followed by a 'coacervation' step that results in phase separation (fit to raw data shown in Figure 2.3 and Figure 2.10a inset).[112]

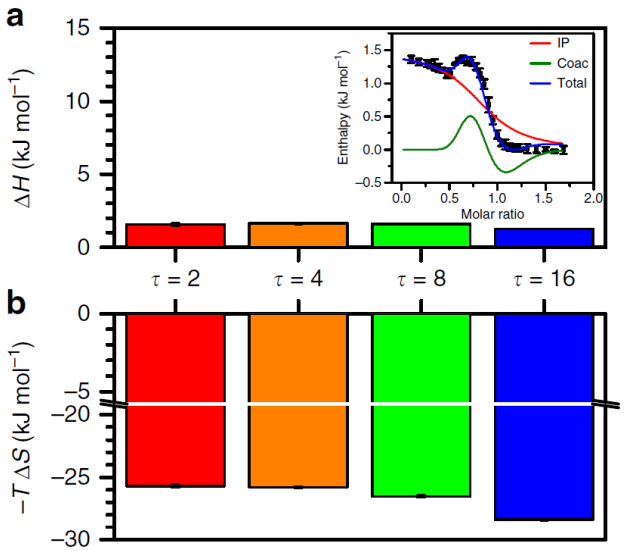

Figure 2.10. Isothermal titration calorimetry (ITC) shows that sequence effects in coacervation are entropically driven. **(a)** The enthalpic contribution to coacervation as a function of τ is small, positive, and does not show significant differences between sequences. Isothermal titration calorimatry captures this thermodynamic value via a fit to an established two-step coacervation model (inset) that distinguishes between enthalpic contributions from ion pairing (IP) and coacervation (Coac) steps.[112] **(b)** The entropic contribution to the coacervation free energy is large, negative, and attributed to counterion release. Clear differences are observed as a function of τ, with an increasing entropic driving force with increasing blockiness (larger τ).

ITC measurements show a small, positive enthalpic contribution to coacervation, consistent with the results of previous investigations (Figure 2.10).[106,112] Variations between different sequences are difficult to resolve due to the small magnitude of this term. In contrast, and as expected, entropy is the primary driving force for coacervation.[104,106,112] Calculated values for $-T\,\Delta\,S$ are both negative and an order of magnitude larger than the observed enthalpies. Furthermore, the entropic driving force for coacervation increases with increasing τ, concomitant with the changes in the width of the coexistence region and the salt resistance observed in simulation and experiment. Furthermore, the magnitude of the entropic differences are significant, spanning ~3 kJ mol^{-1}. This is on the order of thermal energy (~1–2k_BT), which can significantly compete against the translational entropy of the polymer chains. This is conceptually consistent with the observed differences in the phase behavior of the different sequences.

2.4.4 Correlations and Sequence Alignment in Coacervation

We use simulation to understand the role of charge sequence in determining molecular structure of the coacervate phase. We first consider pair correlations under conditions of constant salt concentration (25 mM) corresponding to the high polymer concentration points on the binodal curves (boxed points in Figure 2.9a). These polymer concentrations are relevant for the thermodynamics of coacervation, because they are obtained when coacervation occurs within the two-phase region. The polymer concentration thus depends on the sequence due to the changes in the phase diagram with τ. We focus on the polyanion–polycation correlations $\mathrm{g}_{P+/P-}(r)$ shown in Figure 2.11a. Peaks corresponding to chain connected structure are seen,[72,110] but there is no clear trend as τ is changed. This is consistent with a calcuation of the energy of coacervation in Figure 2.11b, calculated from $U_i = 2\pi\sum_j \rho_i \int_0^\infty dr\, r^2 v_{ij}(r)\mathrm{g}_{ij}(r)$.[94] This summates the energy that a species i 'feels' due to contributions from all other species j, each with a number density ρ_j and an interaction with i via a pair potential v_{ij}.[94] The overall change in energy $\Delta U = \Delta U_{P+} + \Delta U_{P-}$ for coacervation matches with experimental ITC measurements, demonstrating only a small, positive increase that does not depend on τ. This is consistent with the experimental observation that enthalpic effects tend to not dominate the coacervation process.[106,112]

While the coacervation process is not strongly affected by enthalpic effects, the structure of coacervates still exhibits non-trivial correlations associated with the monomer sequences. We use a second comparison where dense phases (denoted with an asterisk in Figure 2.9a) for all values of τ are considered at the same polymer and salt concentrations. This permits a direct comparison between systems with exactly the same components – such as the number of charged/neutral monomers and salt ions – with the only change being the order in which the monomers are connected. Pair correlations $\mathrm{g}_{P+/P-}(r)$ are shown in Figure 2.12a for all values of τ, demonstrating a distinct change in the second peak adjacent to the initial polyanion/ polycation pair.

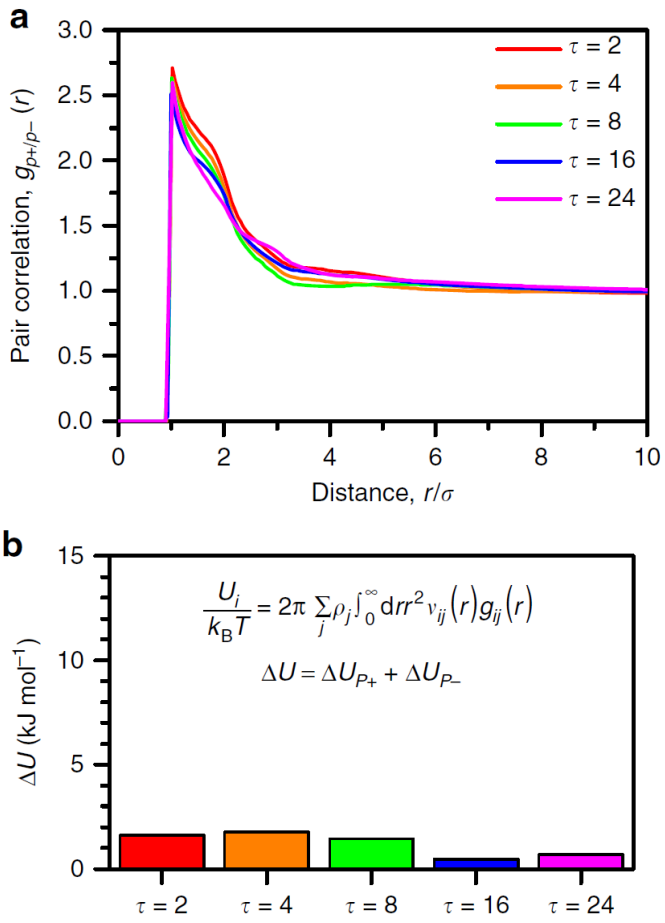

Figure 2.11. Phase separating coacervate structure and energy shows no significant sequence effect. **(a)** Polycation/polyanion pair correlation function for the coacervate phase at various τ (boxed points in Figure 2.9a). Correlations do not show strong dependence on τ. **(b)** Calculation of the change in electrostatic energy for the polycation (from $g(r)$ such as in **(a)**) show small, positive increases in energy during coacervation. This is qualitatively consistent with experimental data in Figure 2.10.

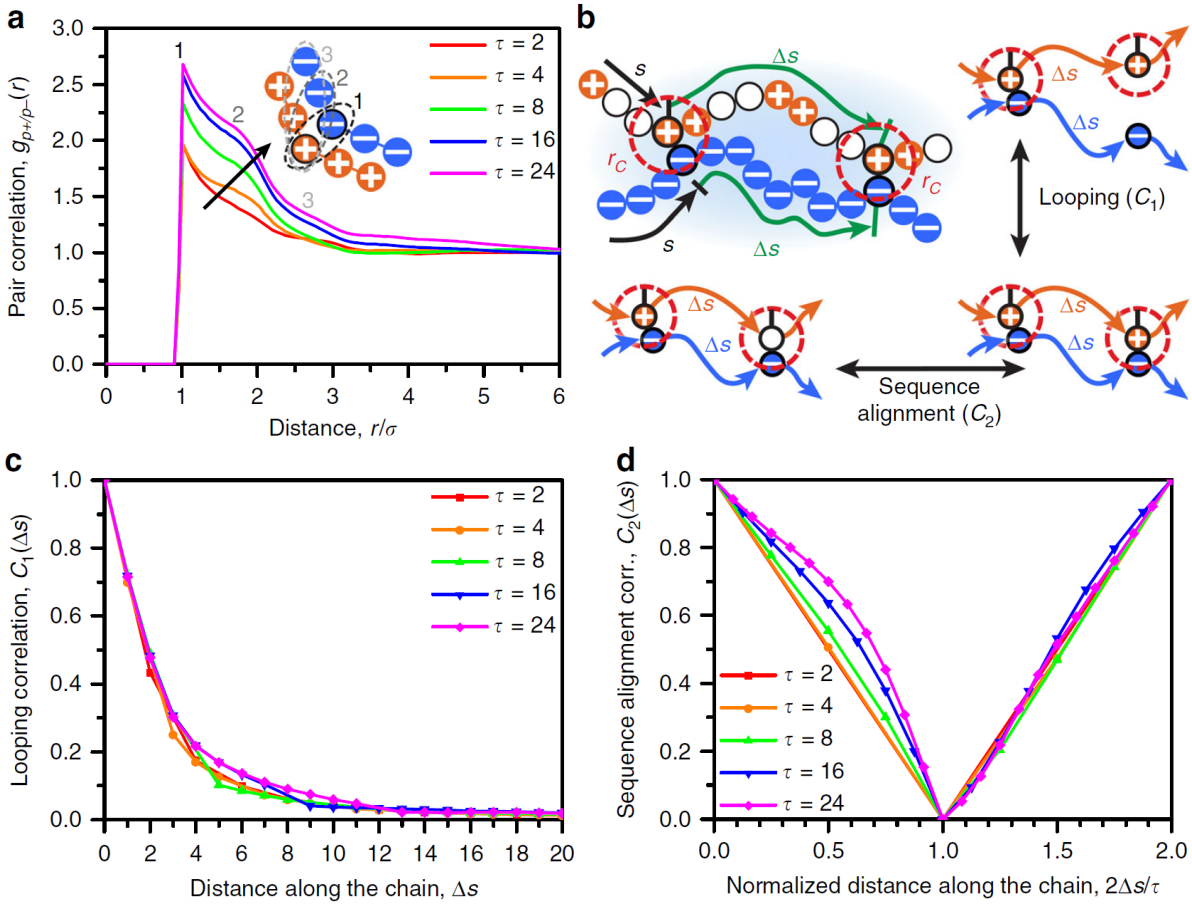

Figure 2.12. Blocky sequences exhibit strong charge correlations due to sequence alignment at the same concentration. **(a)** Polycation/polyanion pair correlations for the dense phase at a single salt/polymer concentration denoted with an asterisk in Figure 2.9a. When species concentrations are kept constant, there is a clear increase in polyelectrolyte correlations. **(b)** We use a set of pair correlations that capture the extent that two nearby chains interact; we follow their contour s and check for both spatial proximity within a cutoff r_C and monomer charge. C_1 determines the probability that charged monomers separated along their respective contours Δs loop. C_2 determines the probability that looped monomers are both charged. **(c)** Spatial looping correlations are measured by C_1, which demonstrates negligible differences between different values of τ. However, there is a tendency for interacting polyelectrolytes to feature runs of charged monomers, whose sequence alignment is quantified by C_2 **(d)** We attribute pair correlations in **(a)** to this effect.

The change in this peak can be interpreted through the use of a set of along-the-chain correlation functions $C_1(\Delta s)$ and $C_2(\Delta s)$, which are a function of the distance along a chain contour Δs described by the index s. We show schematics in Figure 2.12b and provide rigorous definitions in Supplementary Note 1. Both functions start with a pair of polycation/polyanion charges that are

within a cutoff radius r_C from each other, and measure conditional probabilities for two monomers that are Δs monomers away from original pair. $C_1(\Delta s)$ is the probability that these two new monomers are within r_C from each other given that they are both charged, while $C_2(\Delta s)$ is the probability that these two new monomers are both charged given they are within r_C from each other. Conceptually, C_1 is a measure of the contour length over which two nearby chains of opposite charge remain aligned, which we call a looping correlation. To contrast, C_2 is a measure of how much the charged monomers on the patterned chain prefer to be along segments aligned with the opposite polyelectrolyte, which we call a 'sequence alignment' correlation.

$C_1(\Delta s)$ shows a decrease in looping potential with increasing distance along the chain and very little dependence on the value of τ (Figure 2.12c). This indicates that neighboring chains align for approximately the same number of monomers regardless of sequence. A larger correlation effect is apparent in C_2 (Figure 2.12d). Here, the abscissa (Δs) has been normalized by $\tau/2$ in order to highlight the primary difference between values of τ, which is that the probability of finding another charged monomer after a shift of Δs initially decreases much more quickly with small values of τ. In the extreme, for $\tau = 2$, there is by definition no chance of finding a charged monomer for $\Delta s = 1$. To contrast, the likelihood of finding an adjacent charged monomer is very high for large τ, due to the blockier monomer sequence. Beyond this primary probabilistic effect, which is captured by the normalization of Δs, larger values of τ still show a slower C_2 decay. We attribute this secondary effect to a preference for aligned chain segments to include the charged portion of the patterns. Both of these behaviors are due to the electrostatic benefit of aligning charged monomer sequences, such that opposite charges are in close proximity.

These structural changes at the molecular level do not directly influence the macroscopic thermodynamics of coacervation, as evidenced by the small and τ-independent values of ΔU. Instead, C_2 shows that opposite polyelectrolytes tend to align, which entropically confines

polyelectrolyte chains in the coacervate phase. This entropic effect is best seen through the lens of counterion release, and is the main driving force for sequence-dependence in coacervation.

2.4.5 Tuning the Entropy of Counterion Release

The large entropy change upon coacervation observed in ITC is consistent with traditional counterion release arguments for coacervation.[104,113] In the dilute phase, counterions condense along the backbone of a highly charged polyelectrolyte to decrease the local electrostatic energy.[113] This counterion condensation occurs at the expense of the counterion translational entropy. During coacervation, oppositely charged polymers can condense upon each other, similarly lowering the local electrostatic energy. Meanwhile, the previously condensed counterions regain their translational entropy.[69,104,107,113] We use a modified version of this counterion release argument to explain how τ can strongly affect coacervation phase behavior.

We use simulation to characterize counterion condensation in the dilute phase. We use a method developed by Liu and Muthukumar,[114] where condensed counterions are located within a cutoff radius r_{CC} from any monomer along a dilute chain. Each condensed counterion is assigned to its nearest monomer, such that each monomer i has an average number $\langle n_i \rangle$ of counterions condensed (Figure 2.13b). The smaller, neutral monomers have a larger accessible counterion volume with this method. A number is therefore defined for each bead using the condensed counterions $\langle n_i^0 \rangle$ for an uncharged chain. The ratio $\langle n_i \rangle$ / $\langle n_i^0 \rangle$ thus gives a normalized measure of the condensed counterions. We relate this ratio to an effective energy $\epsilon_i = -k_B T \ln\big(\langle n_i \rangle / \langle n_i^0 \rangle\big)$ in a one-dimensional adsorption model that is suited to the high charged densities considered in this work (see Supplementary Note 2). The quantity $\ln\big(\langle n_i \rangle / \langle n_i^0 \rangle\big)$ is plotted as a function of monomer index i for a number of different values of τ (Figure 2.13a). The distribution of counterions along the backbone varies greatly, with low τ

polymers showing relatively uniform condensation while high τ polymers have condensed counterions clustered near the charge blocks (Figure 2.13c).

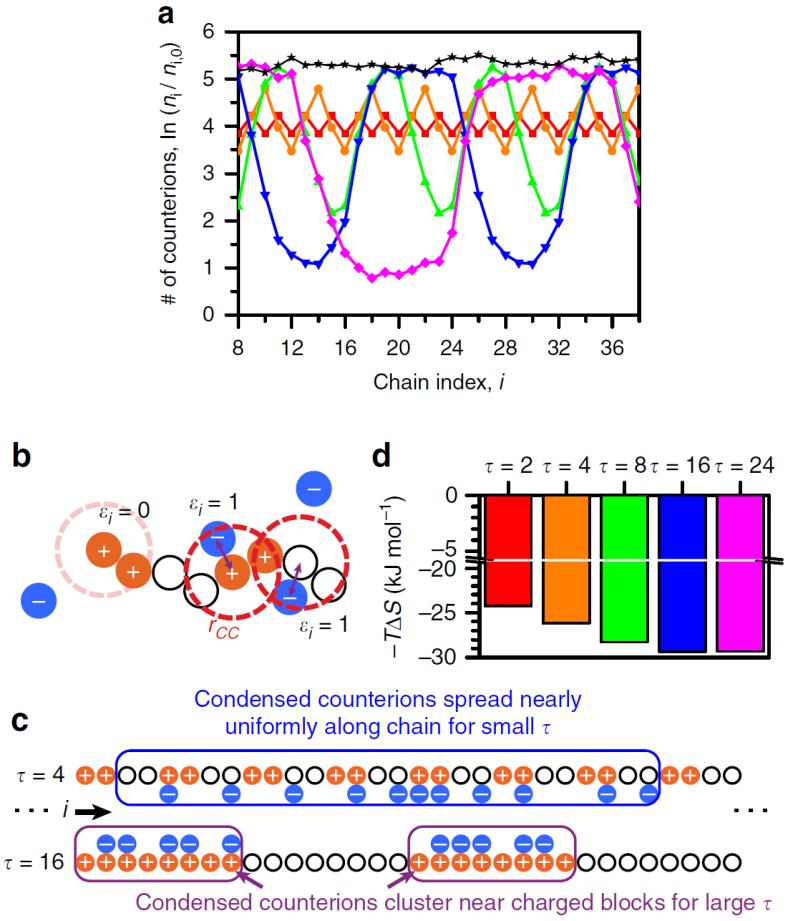

Figure 2.13. Charge sequence effects in coacervation can be explained by 1D counterion confinement entropy. **(a)** The number of counterions n_i condensed as a function of chain index i, relative to the counterions present near an uncharged chain, $n_{i,0}$. Salt concentration is 25 mM, at boxed supernatant points in Figure 2.9a. The value $\ln(n_i/n_{i,0})$ is related to an effective binding energy used in a 1D adsorption model. Colors are the same as Figure 2.9a,d, with a black curve for the homopolyanion. **(b)** The criterion for a condensed counterion is one that is within r_{CC} of a polyelectrolyte charge; it is 'condensed' along the nearest polymer bead of index i. **(c)** Conceptual schematic demonstrating the origin of the charge sequence effect on coacervation. Condensed counterions are uniformly distributed along polyelectrolyte chains with low τ, however at high τ these condensed counterions are confined along the chain contour near the charged blocks. This additional confinement increases the entropic driving force for counterion release. **(d)** This 1D confinement is reflected in the entropic contribution to the free energy, $-T\Delta S$, as calculated from the 1D adsorption model and in near-quantitative matching with ITC data (Figure 2.10b).

To evaluate the effect of this distribution of condensed counterions on the counterion release entropy, we use an expression for the entropy calculated from the same one-dimensional adsorption model (energies normalized by $k_B T$ denoted with a tilde):

$$\frac{S}{k_{\mathrm{B}}} = \sum_i \left[\ln\left(1 + \mathrm{e}^{-(\tilde{\epsilon}_i - \tilde{\mu})}\right) + \tilde{\epsilon}_i \left(\frac{\mathrm{e}^{-(\tilde{\epsilon}_i - \tilde{\mu})}}{1 + \mathrm{e}^{-(\tilde{\epsilon}_i - \tilde{\mu})}} \right) \right] \tag{2.43}$$

In this model, simulation data serves as the primary input of $\tilde{\epsilon}_i$, while the external chemical potential $\tilde{\mu}$ is set at a constant value for all τ and i for a given salt concentration.

Using a single value of $\tilde{\mu}$, we obtain values for the entropic contribution to coacervation in near-quantitative agreement with ITC data (Figure 2.13d). Thus, accounting for the distribution of counterions condensed onto individual polyelectrolytes in the supernatant phase yields a prediction for the sequence- dependence of coacervation. This is a one-dimensional confinement effect. Low-τ systems show an even distribution of condensed counterions along the length of the polyelectrolyte chain (Figure 2.13c; τ = 4). However, as τ is increased, the counterions are increasingly confined near the charged blocks (Figure 2.13c; τ = 16). Counterions that are more confined consequently gain more entropy upon release, leading to the increasingly negative values of $-T\Delta S$ with increasing τ observed in Figure. 2.10b and 2.13d.

2.5 Discussion and Conclusions

We used a combination of experiment, theory, and simulation to demonstrate the profound effect of polyelectrolyte monomer sequence on charge-driven materials structure and thermodynamics. Sequence-defined polypeptides were used to evaluate this monomer sequence effect, demonstrating qualitative matching with simulation. This sequence effect is due to differences in entropic confinement of condensed counterions along the polymer, which changes drastically with the blockiness of the sequence. Experimental thermodynamic measurements are

consistent with this picture, showing that entropy dominates coacervation while enthalpic contributions are negligible.

We emphasize that this charge patterning effect does not rely on subtle chemical or solvent-specific effects, and trends can be captured using coarse-grained electrostatic models. However, we note that such effects would be important to obtain quantitative predictions. Implications for these charge patterning effects extend from biological polymers to materials design. Sequences featuring runs of similarly charged macromolecules may provide a way to tune biophysical interactions, with long, charge-dense sequences exhibiting stronger charge interactions than patterns with less-blocky runs of the same charge.

For materials design, charge patterning represents a way to deliberately tune charge interactions in coacervate-driven assembly. This is one way that sequence information may be included into the backbone of a polymer chain that is distinct from, *i.e.*, random copolymerization or block copolymerization. This mechanism is not an averaging of dispersive effects, but rather a precise tuning of the local arrangements of charge. Indeed, by combining with the aforementioned sequence effects we envision a number of sequence-scales that can be used to tune charge-driven assembly. We foresee this as one way to utilize the development of sequence-specific synthesis to reach ever-more complex assemblies.

2.6 Supplementary Note 1

2.6.1 Along-the-chain Correlation Functions

We characterize the structure and sequence behaviors of charge sequences using a pair of correlation functions C_1 and C_2 that characterize spatial and sequence-based structure respectively. Both consider an initial pair of oppositely-charged monomers, i and j, that are separated by a distance less than or equal to a cutoff r_C. We then characterize properties of two beads a constant number of monomers Δs along the chain contour, $i + \Delta s$ and $j + \Delta s$.

$C_1(\Delta s)$ provides a structural measure of looping among neighboring polyelectrolytes. We calculate the probability that $i + \Delta s$ and $j + \Delta s$ are also within the cutoff r_C, *if* both monomers are charged. Formally, this is given by the equation:

$$C_1(\Delta s) = \frac{\langle \sum_i \sum_j \delta(z_i - 1)\delta(z_j + 1)\delta(z_{i+\Delta s} - 1)\delta(z_{j+\Delta s} + 1)\Theta(r_C - r_{ij})\Theta(r_C - r_{i+\Delta s, j+\Delta s})\rangle}{\langle \sum_i \sum_j \delta(z_i - 1)\delta(z_j + 1)\delta(z_{i+\Delta s} - 1)\delta(z_{j+\Delta s} + 1)\Theta(r_C - r_{ij})\rangle} \tag{2.44}$$

Here the function $\Theta(x)$ is the Heaviside function that is $\Theta\ x = 1$ for $x \geq 0$ and $\Theta\ x = 0$ for $x < 0$. The average denoted by the angle brackets $\langle \ldots \rangle$ represents ensemble averages taken over the course of a simulation, and $\delta(x)$ is the Dirac delta function. This is a measure of conformational correlations by determining the subset of polyelectrolyte charges that loop over a number of monomers Δs.

This measure of $C_1(\Delta s)$ between charged particles has some values that are necessarily 0 due to the periodicity of the pattern; these are removed from representations of this function for clarity.

$C_2(\Delta s)$ is a related measure of the sequence correlations:

$$C_1(\Delta s) = \frac{\langle \sum_i \sum_j \delta(z_i - 1)\delta(z_j + 1)\delta(z_{i+\Delta s} - 1)\delta(z_{j+\Delta s} + 1)\Theta(r_C - r_{ij})\Theta(r_C - r_{i+\Delta s, j+\Delta s})\rangle}{\langle \sum_i \sum_j \delta(z_i - 1)\delta(z_j + 1)\delta(z_{i+\Delta s} - 1)\delta(z_{j+\Delta s} + 1)\Theta(r_C - r_{ij})\rangle} \tag{2.45}$$

The difference in this correlation function is that we are now considering the subset of loops that consist of charged monomers. For this work, we set $r_C = 1.5\sigma_+$.

2.7 Supplementary Note 2

2.7.1 One-dimensional Adsorption Model

We can use simulation data of a single, dilute polyelectrolyte chain in a salt solution to calculate the entropic driving force for counterion release. To do this, we map simulation data to a

one-dimensional adsorption model where each monomer of the polyelectrolyte chain is a 'site' that can contain a condensed counterion. These adsorbed counterions are in equilibrium with the external solution that is a constant chemical potential μ reservoir of salt *ions*. Each adsorbed ion 'feels' an effective binding energy ϵ_i that is due to the electrostatic characteristics of the chain and the surrounding condensed charges, and is a function of the chain index i. The grand canonical partition function for adsorption on to a chain of length *N* is thus:

$$\Xi = \prod_{i}^{N} \left(1 + e^{-\beta(\epsilon_i - \mu)}\right) \tag{2.46}$$

Standard statistical mechanics leads to expressions for both the average number of adsorbed counterions $\langle n_i \rangle$ at a given index i and the overall entropy of the adsorbed counterions S_{ads}:

$$\sum_i \langle n_i \rangle = k_B T \left(\frac{\partial \ln \Xi}{\partial \mu}\right)_T = \sum_i \frac{e^{-\beta(\epsilon_i - \mu)}}{1 + e^{-\beta(\epsilon_i - \mu)}} \tag{2.47}$$

$$S_{ads} = k_B \left(\frac{\partial T \ln \Xi}{\partial T}\right)_{\tilde{\mu}} = k_B \left[\sum_i \ln\left(1 + e^{-\beta(\epsilon_i - \mu)}\right) + \frac{\epsilon_i}{k_B T}\left(\frac{e^{-\beta(\epsilon_i - \mu)}}{1 + e^{-\beta(\epsilon_i - \mu)}}\right)\right] \tag{2.48}$$

This calculation requires determining the parameters of this model; namely, the values of the energy ϵ_i along the chain and the chemical potential of the reservoir. We use simulation to determine the former, and keep the latter as a parameter that is constant for all systems at a given salt concentration.

2.7.2 Determination of Counterion Condensation

We first determine the number and distribution of condensed counterions. We use a methodology described in Liu and Muthukumar[114] to characterize the extent of counterion condensation along a dilute polyelectrolyte chain. In this methodology, a cutoff distance r_{CC} is chosen to represent the near-chain region; salt ions that are within r_{CC} from a polyelectrolyte bead

are considered condensed. We choose r_{CC} = 1.5σ_{P+}. This is somewhat arbitrary, however we find that our results are not strongly affected by the specific choice of r_{CC}. We schematically demonstrate this method in Figure 2.12b. Condensed counterions are assigned to an index i, which is the nearest polyelectrolyte chain monomer. Averaged over a simulation run, we obtain a value of $\langle n_i \rangle$.

The size difference between charged and neutral beads causes the value of $\langle n_i \rangle$ to be significantly different for a fixed r_{CC}. $\langle n_i \rangle$ for a charged bead will typically be smaller than for a neutral bead because there is less unoccupied volume. This does not, however, represent a physically meaningful difference, but rather due to the arbitrary definition of r_{CC}. Rather than vary r_{CC}, we choose to normalize $\langle n_i \rangle$ to remove this disparity by calculating a value $\langle n_i^0 \rangle$ that is determined from simulations where the polyelectrolyte charge is taken to z_{P+} = 0. This establishes the number of counterions that would fit the definition of a condensed charge for a neutral chain, which also varies with the different-sized beads. Indeed, this variation introduces the same effect as for a charged chain, so a ratio $\langle n_i \rangle$ / $\langle n_i^0 \rangle$ removes effects due to the difference in unoccupied volumes between the two bead types.

2.7.3 Effective Binding Energy

We can convert the number of counterion beads into an effective ϵ_i. We do so using the previously determined relationship:

$$\langle n_i \rangle = \frac{e^{-\beta(\epsilon_i - \mu)}}{1 + e^{-\beta(\epsilon_i - \mu)}} \tag{2.49}$$

The effective energy ϵ_i is defined as the effect of the charged polyelectrolyte chain and the condensed counterions. We can thus set $\epsilon_i \rightarrow 0$ for the uncharged polyelectrolyte chains, leading to the relationship:

$$\langle n_i^0 \rangle = \frac{e^{\beta\mu}}{1 + e^{\beta\mu}} \tag{2.50}$$

We can thus define the ratio:

$$\frac{\langle n_i \rangle}{\langle n_i^0 \rangle} = \frac{\left(1 + e^{\beta\mu}\right)e^{-\beta(\epsilon_i - \mu)}}{(1 + e^{-\beta(\epsilon_i - \mu)})e^{\beta\mu}} \tag{2.51}$$

The quantities $e^{\beta\mu} \ll 1$ and $e^{-\beta(\epsilon_i - \mu)} \ll 1$ for the cases we consider in this paper (an *a posteriori* observation). We can thus simplify the relationship to the following expression for the effective ϵ_i:

$$\epsilon_i \approx -k_B T \ln(\langle n_i \rangle / \langle n_i^0 \rangle) \tag{2.52}$$

This enables the calculation of the entropy of counterion condensation, via Eq. (2.48), via the conversion of simulation data for n_i to the effective binding energy. This is the procedure used to calculate the values used in Figure 2.12 of the main manuscript.

CHAPTER 3

DESIGNING ELECTROSTATIC INTERACTIONS VIA POLYELECTROLYTE MONOMER SEQUENCE*

3.1 Abstract

Charged polymers are ubiquitous in biological systems because electrostatic interactions can drive complicated structure formation and respond to environmental parameters such as ionic strength and pH. In these systems, function emerges from sophisticated molecular design; for example, intrinsically disordered proteins leverage specific sequences of monomeric charges to control the formation and function of intracellular compartments known as membraneless organelles. The role of a charged monomer sequence in dictating the strength of electrostatic interactions remains poorly understood despite extensive evidence that sequence is a powerful tool biology uses to tune soft materials. In this article, we use a combination of theory, experiment, and simulation to establish the physical principles governing sequence-driven control of electrostatic interactions. We predict how arbitrary sequences of charge give rise to drastic changes in electrostatic interactions and correspondingly phase behavior. We generalize a transfer matrix formalism that describes a phase separation phenomenon known as "complex coacervation" and provide a theoretical framework to predict the phase behavior of charge sequences. This work thus provides insights into both how charge sequence is used in biology and how it could be used to engineer properties of synthetic polymer systems.

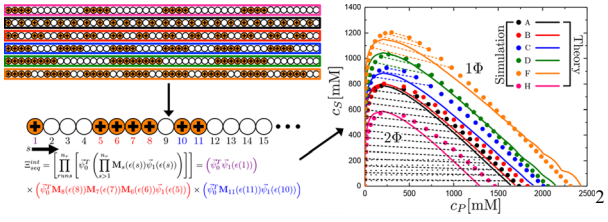

* Part of this work has been published: T.K. Lytle, L.W. Chang, N. Markiewicz, S.L. Perry, C.E. Sing, *Designing Electrostatic Interactions via Polyelectrolyte Monomer Sequence*, ACS Central Science, (2019), **5**, 709-718, https://pubs.acs.org/doi/10.1021/acscentsci.9b00087. Further permissions related to the material excerpted should be directed to the ACS.

3.2 Introduction

Understanding the role of monomer sequence on the physical properties of long-chain macromolecules remains a grand challenge in the field of polymer science,[75,115] due to the utility of sequence as a tool to store information and drive structure formation in biological polymers such as proteins, RNA, and DNA.[76] This takes place in a number of ways; for example, molecular storage of genomic data is encoded in DNA via a sequence of four different base pairs which can then be read by the protein machinery of the cell. Proteins leverage sequences incorporating any number of roughly 20 amino acids, that then often undergo hierarchical assembly into highly complex and precise three-dimensional structures. A subclass of proteins known as intrinsically disordered proteins (IDPs) are subtly different, in that they tend not form secondary or higher-order structures; however, IDPs remain crucial to biological structure and function.[30,116] Despite this lack of hierarchical order, recent work has shown that the precise sequence of charged amino acids still plays a defining role in the structure and function of IDPs.[8,9,36–41] This suggests that the physical effects of charged monomer sequences are generally relevant for a broad range of polymeric materials, not limited to biological molecules; however, the underlying physics of these sequence-dependent electrostatic interactions is not well understood.

Many recent efforts to understand sequence-dependent polymers have focused on biological systems, in particular, intracellular structures known as membraneless organelles or biomolecular condensates.[37,117–123] Membraneless organelles are intracellular compartments that consist largely of IDPs[37,117–119,121,122,124] and are often driven by interactions with oppositely charged polymers such as RNA.[8,125–127] A flurry of recent simulation and theory work has begun to model this class of biomacromolecular systems, mostly focusing on uncovering correlations between physical quantities over a vast and complex amino acid parameter space.[9,38,79,82,128–132] Despite this progress, there remains a need to develop bottom-up theory and simulation that can elucidate the physics of sequence-dependent phase behavior and to do so generally enough that the promise of sequence-defined polymers can be realized in nonbiological systems.[42,43,133,44–51]

In this spirit of understanding sequence-dependent interactions in nonbiological systems, we turn to a class of polyelectrolyte solutions known as *polymeric complex coacervates*, which are considered analogous to membraneless organelles. Coacervates consist of oppositely charged polymers (a polycation and a polyanion) in an aqueous salt solution.[18,134,135] The charge-driven association between the polyelectrolytes drives a phase separation process, forming a polymer-dense coacervate phase and a polymer-dilute supernatant phase (Figure 3.1a inset). This phase behavior is commonly plotted on a salt concentration versus polymer concentration phase diagram (Figure 3.1a),[11,68,70] with coacervation occurring in a two-phase region at low salt and polymer concentrations. A tie line in this region connects the polymer-dense coacervate (Figure 3.1a, α) to the polymer-dilute supernatant phase (Figure 3.1a, β).[5,70,72,73]

Sequence effects similar to those found in IDPs and membraneless organelles are indeed observed in coacervate-forming systems.[136] The effects of sequence on coacervation were explored using mixtures of a homopolyanion with different sequence-specific polycations containing a 50% mixture of charged and uncharged monomers.[136] Regular polycation sequences, ranging from fully alternating to "blocky" copolymers exhibited significant differences in phase behavior and thermodynamics as determined by both experiment and simulation.[136] This established a clear connection between charged monomer sequence and coacervate thermodynamics, but prior work has only explored a very limited area of sequence space;[136] there is a need to develop predictive tools to connect arbitrary sequences to the strength of electrostatic interactions.

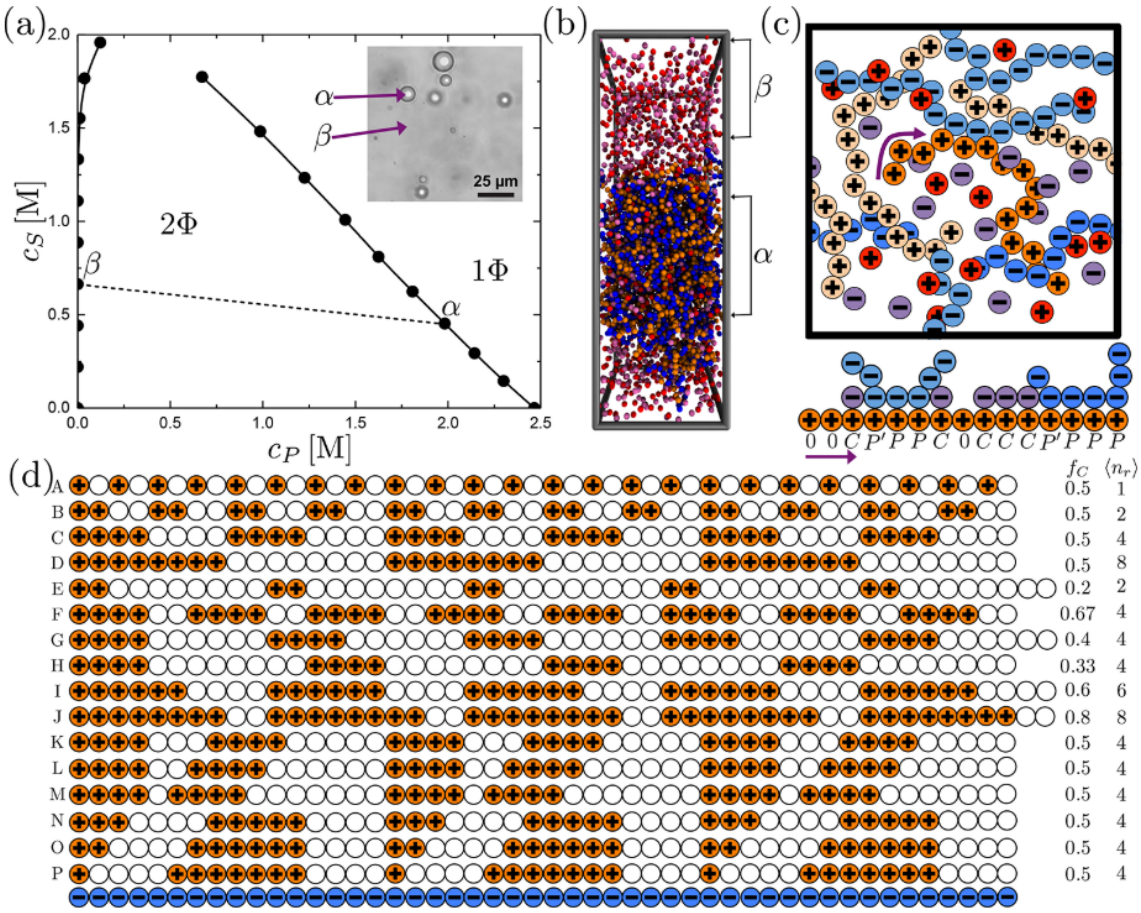

Figure 3.1. (a) Example coacervate phase diagram, calculated from the transfer matrix theory of Lytle and Sing[69] described in Eq 3.1. The area in the bottom left half of the plot is a two-phase (2Φ) region where coacervation occurs along tie lines that connect the polymer-dense coacervate phase (α) to a polymer-dilute supernatant phase (β). The negative slope of the tie line reflects the preferential partitioning of salt to the supernatant phase. The inset shows an optical micrograph of this phase separation, formed from sequence-controlled peptides of poly(lysine-co-glycine) and poly(glutamate) with the coacervate α and supernatant β phases indicated. **(b)** Simulation snapshot of coacervation, showing the polymer-dense coacervate phase α and polymer-dilute supernatant phase β, at concentrations that reflect the indicated tie line in **(a)**. **(c)** Schematic of a coacervate phase, showing a test polycation (orange). The transfer matrix theory in this Chapter is concerned with the adsorption of oppositely charged species to this chain, as shown in the simplified representation shown at the bottom. **(d)** The sequences used in this Chapter (A–P), along with the homopolyanion (blue) that is partnered with the polycation sequences. Sequences can be characterized by parameters such as charge fraction f_C and average "run" length $\langle n_r \rangle$; however, sequences are not uniquely characterized by these two parameters.

Theory is an ideal tool to rapidly explore and understand this sequence space; however, historical efforts to theoretically describe complex coacervation are not well-suited to

understanding or predicting the effect of charged monomer sequence. The original coacervation theory developed by Voorn and Overbeek accounted for charged interactions only through the Debye−Hückel attraction that arises in unconnected, dilute electrolytes.[11,68,70,137] Increasingly sophisticated field theoretic methods have since made an effort to address these shortcomings,[99–102,138–140] with parallel efforts using liquid state theory,[110,141,142] blob arguments,[143–146] and other related theoretical[107,147,148] and computational[149–151] methods. While these assorted theoretical efforts have all contributed to the basic understanding of experimental results on coacervates,[46,74-87] they struggle to resolve monomer-level details important for considering monomer to monomer sequence in coacervation.

We have demonstrated the sensitivity of coacervation to monomer-level structure in previous studies,[14,72,74] which show how polymer charge spacing, stiffness, and architecture can play a marked role in determining phase behavior (example snapshot in Figure 3.1b). Informed by our simulation results, we have developed a new transfer matrix approach that predicts coacervation in a way that reflects these important molecular features.[69,73,74] This model keeps track of the oppositely charged ions and polyelectrolytes surrounding a test polyelectrolyte, by mapping to an adsorption model; here, the test polyelectrolyte is a series of monomeric adsorption sites to which the oppositely charged species bind (see schematic in Figure 3.1c).[69] The resulting free energy expression for coacervation is thus:[69]

$$\frac{\mathcal{F}_{\mathrm{TM}}}{Vk_{\mathrm{B}}T} = \sum_i \frac{\phi_i}{N_i} \ln \phi_i + \frac{\phi_P}{2N_P} \ln[\psi_0^{\mathrm{T}} \mathbf{M}_0^{N_P} \psi_1] + \zeta \left(\sum_{i \neq W} \Lambda_i \phi_i \right)^3 \tag{3.1}$$

This expression is comprised of three terms; the first term is the translational entropy of all the species *i*, the second term is the transfer matrix expression for the interactions between charged polymers and their surroundings, and the final term is a phenomenological expression for the non-pairwise excluded volume. The subscript $i = P, S, W$ denotes the polyelectrolyte, salt ion, and water species, respectively. A plus ("+") or minus "−") may be necessary to distinguish positively or

negatively charged species, if these are asymmetric. ϕ_i is the volume fraction of species i, N_i is the degree of polymerization, and Λ_i is a correction factor for the effective excluded volume. ζ is a phenomenological constant to account for the non-pairwise excluded volume. The transfer matrix $\mathbf{M_0}$ is comprised of the Boltzmann factors related to the adsorption of the various charged species (Figure 3.1c), counterions C, the initial oppositely charged monomers P', and subsequent monomers along the same chain P, and unpaired sites 0. By distinguishing P and P', we take into account the possibility of oppositely charged polyelectrolytes adsorbing sequentially along the test chain. In this way we can write the grand canonical partition function for the polyelectrolyte interaction with its surroundings, $\Xi^{\text{int}} = \vec{\psi}_0^{\text{T}}\, \mathbf{M}_0^{\text{N}_\text{P}}\, \vec{\psi}_1$, which is the term in the interaction term of $\mathcal{F}_{\text{TM}}$. The form of this matrix has been previously derived,[69,73,74] and we denote it with a subscript 0 to indicate that this is for an unpatterned, homopolyelectrolyte test chain:

$$\mathbf{M}_0 = \begin{bmatrix} CC & CP & CP' & C0 \\ PC & PP & PP' & P0 \\ P'C & P'P & P'P' & P'0 \\ 0C & 0P & 0P' & 00 \end{bmatrix} = \begin{bmatrix} A_0\phi_S & A_0\phi_S & A_0\phi_S & A_0\phi_S \\ 0 & 1 & 2 & 0 \\ B_0\phi_P & B_0\phi_P & B_0\phi_P & B_0\phi_P \\ D & D & D & D \end{bmatrix} \tag{3.2}$$

Here, the first version of the matrix shows the pair of sequences that the matrix element represents (*i.e.*, a C after a P' would be the CP' element). $D = e^{-\epsilon}$ accounts for the electrostatic energy penalty when charges along the test chain are "unpaired." The vector $\psi_1 = [C, P, P', 0]^T = \left[\mathrm{A}_0\phi_s, 0, B_0\phi_p, D\right]^T$ is the set of Boltzmann factors for the very first monomer on a chain, and ψ_0 is a vector of ones. The form of the terms $\mathrm{A}_0\phi_\mathrm{s}$ and $B_0\phi_p$ are described in previous work by Lytle and Sing.[69,73,74] In this chapter, we show how this approach can be generalized to account for coacervates formed from monodisperse but *arbitrary* sequences. We compare transfer matrix results directly with experiment and simulation, and observe qualitative agreement for a wide variety of test sequences. Subtle changes in monomer sequence can affect the strength of

electrostatic interactions between oppositely charged polyelectrolytes and the resulting phase behavior.

3.3 Materials and Methods

3.3.1 Monte Carlo Simulations

Monte Carlo simulations were performed for systems containing n_{p-} homopolyanions, n_{p+} patterned polycations, n_{s+} cations, n_{s-} anions, and water using the restricted primitive model; this is identical to the model considered in our previous work on charge patterning.[136] The water solvent was modeled as a continuum with relative dielectric constant ϵ_r = 78.5. Nonsolvent species were modeled as hard spheres, with charged species having a diameter $\sigma_{\pm}$ = 4.25 Å and neutral monomers in the polycation hard spheres, with charged species having a diameter $\sigma_{\pm}$ = 4.25 Å and neutral monomers in the polycation chain having a diameter $\sigma_0 = \sigma_{\pm}/4$. Polymeric species have a degree of polymerization *N*, and polycations have a charge fraction, f_C, which is the number of charged monomers divided by the total degree of polymerization. Schematically this is represented in Figure 3.2. The total potential of the system is given by:

$$U = U_{ES} + U_{HS} + U_B + U_\theta \tag{3.3}$$

Where U_{ES} is the electrostatic potential, U_{HS} is the hard sphere potential, U_θ is the bending potential, and U_B is the bonded potential. The electrostatic potential is a Coulomb potential given by:

$$U_{ES} = \sum_i \sum_{j>i} \frac{q_i q_j e^2}{4\pi\epsilon_0\epsilon_r r_{ij}} \tag{3.4}$$

In this equation, q_i is the valency of bead *i*, *e* is the charge of an electron, ϵ_0 is the vacuum permittivity, and r_{ij} is the separation between beads *i* and *j*. Electrostatic interactions are calculated using Ewald summation. The beads have excluded volume captured via a hard-sphere potential:

$$U_{HS} = \sum_i \sum_{j>i} \begin{cases} \infty & r_{ij} < (\sigma_i/2) + (\sigma_j/2) \\ 0 & r_{ij} \geq (\sigma_i/2) + (\sigma_j/2) \end{cases} \tag{3.5}$$

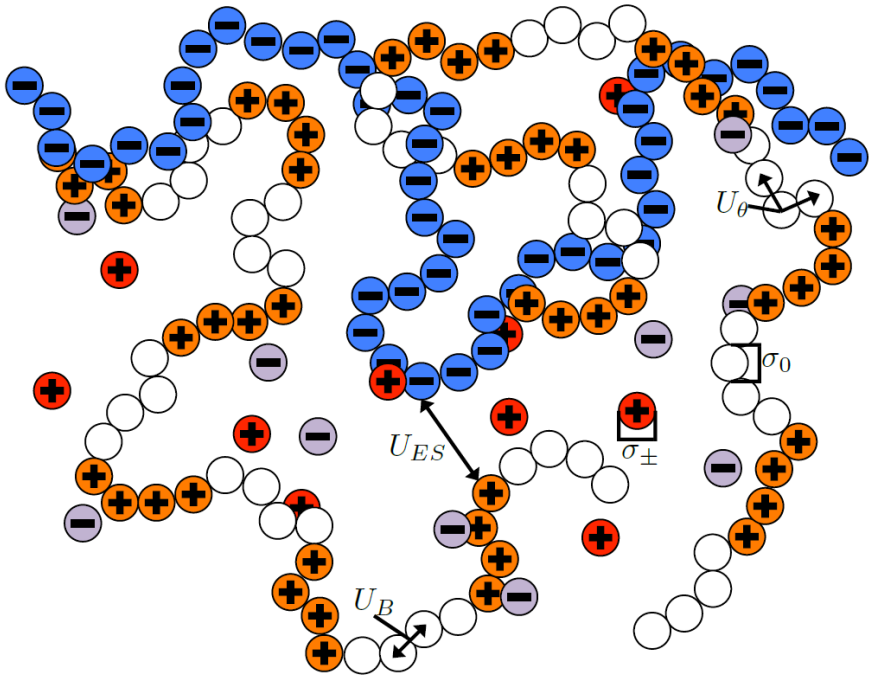

Figure 3.2. Schematic of restricted primitive model system. The polyanion chains are homopolymers with every monomer charged and colored blue. The polycation chains are copolymers of charged monomers (orange) and neutral monomers (white). The size of the neutral monomers is bigger than in the actual system for visual clarity. Cations are red, and anions are purple. Charged beads have a diameter $\sigma_\pm$, and neutral monomers have a diameter σ_0. Charged species interact with each other through a Coulomb potential, U_{ES}. Polymers are bound together with a bonding potential, U_B, and have a bending potential, U_θ.

Polymeric species are bound together using a square-well bonding potential:

$$U_B = \sum_i \begin{cases} \infty & r_{i,i+1} < \Delta_{\min} \\ 0 & \Delta_{\min} \leq r_{i,i+1} \leq \Delta_{\max} \\ \infty & r_{i,i+1} > \Delta_{\max} \end{cases} \tag{3.6}$$

where $\Delta_{\min}$ is the minimum bond length, and $\Delta_{\max}$ is the maximum bond length. The polymers also have some stiffness modeled using a bending potential as a function of the angle between two connected bonds, $\theta_{i,i+1,i+2}$, given by:

$$U_\theta = \sum_i \frac{\kappa}{2} \left(\theta_{i,i+1,i+2} - \theta_0\right)^2 \tag{3.7}$$

where κ determines the strength of the angle potential, and θ_0 is the equilibrium angle between adjacent bonds.

These simulations used degree of polymerizations $N = 48$ or 50, depending on the charge sequence of the polycation. Maximum and minimum bond lengths were set at $\Delta_{\min} = \sigma_\pm$ and $\Delta_{\max} = \Delta_{\min} + 0.01\sigma_\pm$. The angle potential strength is set at $\kappa = 3.30\ k_B\ T$, where k_B is Boltzmann's constant, and $T = 298$ K is the temperature. The equilibrium angle is $\theta_0 = 0$.

3.3.2 Monte Carlo Simulations of a Single Polyelectrolyte in Dilute Salt Solution

The above Monte Carlo model was used to determine the localization of salt ions near a single polyelectrolyte in a dilute salt system, represented schematically in Figure 3.3. A single polyelectrolyte was simulated with salt ions to determine the number density $n_C(s)$ of condensed salt ions as a function of monomer index s. During the simulation, the separation distance between monomers and salt ions were calculated. If this separation was within a cutoff distance, $r_C = 1.5\sigma_\pm$, then the salt ion was considered to be localized at the monomer. An additional simulation was

performed in the limit of no electrostatic interactions, and the number density of condensed salt ions $n_{C,0}(s)$ was again calculated. The ratio of these two numbers was used to calculate the monomer-dependent energy parameter $\epsilon(s)$. These simulations were performed using $\phi_S = 1.32 \times 10^{-4}$, which was taken to be sufficiently large that the polymer counterions represented only a small fraction of the overall number of salt ions in the system. We show two representative simulation snapshots in Figure 3.4 for charged (left) and uncharged (right) polymers.

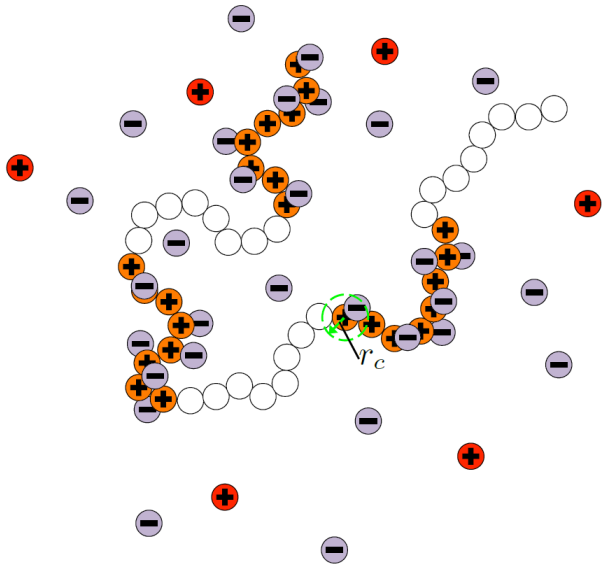

Figure 3.3. Schematic of the single chain Monte Carlo simulations. The polycation has orange beads representing charged monomers and white beads representing neutral monomers. Anions are purple, and cations are red. These simulations measure the number density of condensed counterions as a function of monomer index. A counterion is considered condensed if the separation between the counterion and monomers is less than a cutoff distance r_C . This cutoff distance is schematically represented as the dashed, green circle.

To determine the value of ϵ (s), we use a simplified expression for $n_C(s) \sim e^{-(\epsilon(s)-\mu)} / \left(1 + e^{-(\epsilon(s)-\mu)}\right)$ that is based on a simple, uncorrelated adsorption of counterions along a chain backbone. This approximates the value of ϵ as implicitly including the many-body interactions associated with the local chain environment in the simulation (*i.e.*, nearby monomers). This expression for n_C is dependent on the value of the chemical potential μ in this simple adsorption description, so we also ran Monte Carlo simulations in the absence of

electrostatic interactions to obtain a related $n_{C,0}(s) \sim e^{\mu} / (1 + e^{\mu})$. This number is non-zero, since there is *always* some concentration of opposite salt ions in the cutoff radius r_C. The ratio of these two number densities is $n_C(s)/n_{C,0}(s) = e^{-\epsilon(s)}$ in the limit that $e^{\mu} \sim \phi_s \ll 1$, which is true at low salt concentrations.[136]

To show that this procedure is, in this limit, insensitive to the choice of salt concentration, we show the value of ϵ(s) plotted for a wide range of concentrations (spanning ≈ 1.5 orders of magnitude in ϕ_S) in Figure 3.5. We plot sequences A and C, along with the homopolyanion used in this chapter, and emphasize that there is excellent agreement in ϵ(s) among the different values of ϕ_S.

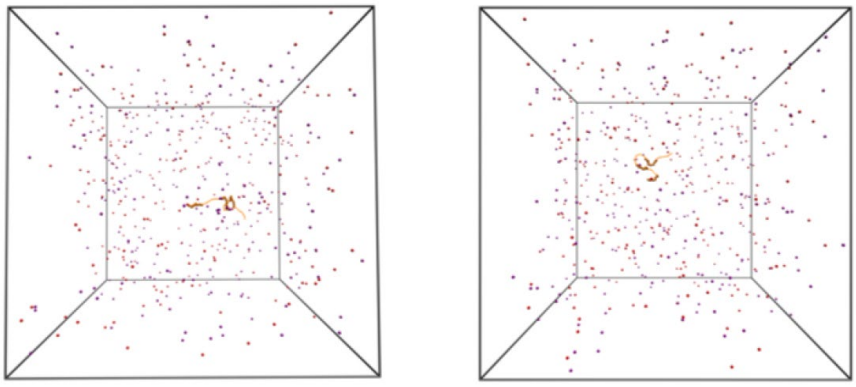

Figure 3.4. Snapshots of single-molecule simulations of sequence D used to determine ϵ(s), including simulations with charged (left) and uncharged (right) polymers.

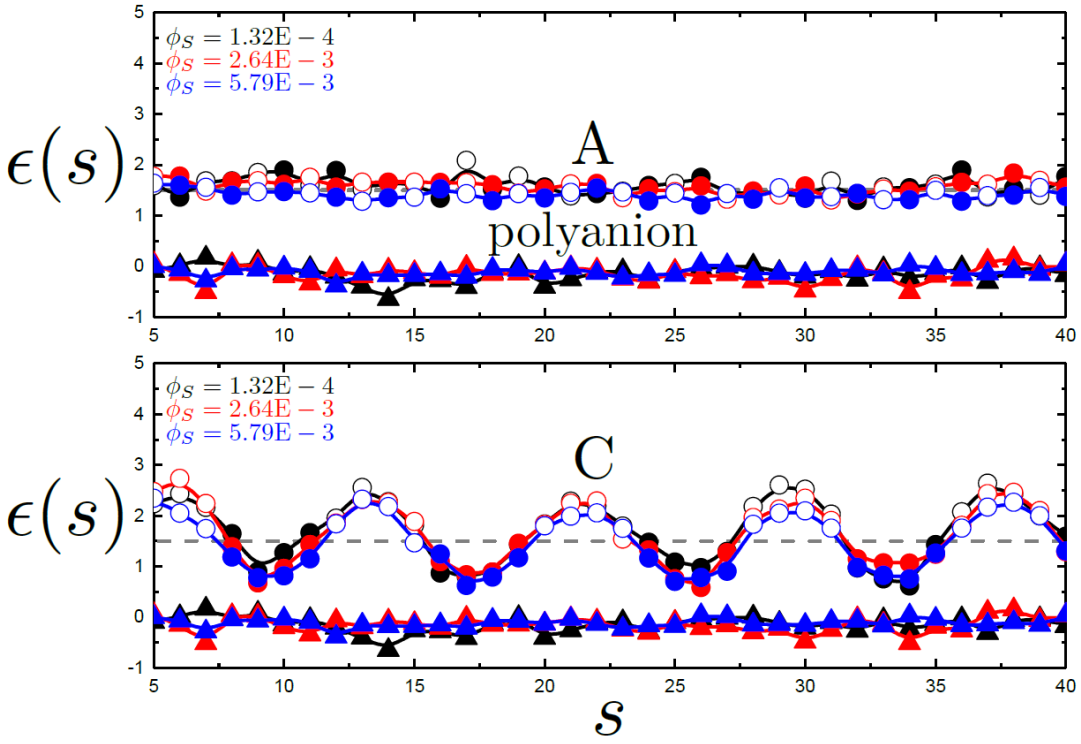

Figure 3.5. Monomer-dependent energy $\epsilon(s)$ as a function of the chain index s, measured by single-polyelectrolyte simulations over a range of dilute salt concentrations ϕ_S. Sequences A and C are considered, along with the corresponding homopolyanions, and exhibit nearly identical values of E regardless of the choice of ϕ_S.

3.3.3 Molecular Dynamics Simulations

Snapshots shown in Figure 3.9b were taken from molecular dynamics simulations using the above-described restrictive primitive model with alterations to the excluded volume and bonding potentials so that they are no longer discontinuous. Excluded volume is included in these simulations using a Lennard-Jones potential U_{LJ} given by:

$$U_{LJ} = \sum_i \sum_j 4\epsilon_{LJ} \left[\left(\frac{\sigma_{ij}^{LJ}}{r_{ij}} \right)^{12} - \left(\frac{\sigma_{ij}^{LJ}}{r_{ij}} \right)^{6} \right] \qquad r_{ij} < r_{ij}^{c} \tag{3.8}$$

ϵ_{LJ} is the depth of the potential well, σ_{ij}^{LJ} is the separation between beads i and j at which this potential becomes 0, and r_{ij}^{c} is the cutoff distance for U_{LJ}. The square-well bonding potential is replaced with a harmonic spring potential:

$$U_B = \sum_i \frac{\kappa_B}{2} \left(r_{i,i+1} - r_0\right)^2 \tag{3.9}$$

where U_B is the bond potential strength, and the equilibrium bond distance is r_0.

The bonding potential parameters are set as $U_B = 250 k_B T$ and $r_0 = 1.05\sigma_{\pm}$. The hard sphere potential is matched by setting the Lennard-Jones parameters as $\epsilon_{LJ} = 10.75\ k_B\ T$ and $\sigma_{ij}^{LJ} = r_{ij}^{c} = (\sigma_i + \sigma_j)/2$. Pair correlation functions were calculated for a number of concentrations of polymer and salt to show that the structure of molecular dynamics and Monte Carlo simulations match almost exactly.[73]

3.3.4 Pressure Calculation

Pressure, p, was calculated using phantom box volume changes[157] in Monte Carlo simulations with no salt ions. For each instance of calculating pressure both a compressive and expansive volume change is performed. These volume changes have the same magnitude, but different directions. Since these are phantom volume changes, the volume of the simulation box does not change throughout the simulation. Pressure can be calculated via:[157]

$$\frac{p\Delta V_+}{k_B T} = \left(N n_{P+} + N n_{P-}\right) \ln\left(1 + \frac{\Delta V_+}{V}\right) + \ln\left\langle \exp\left(-\frac{\Delta U_+}{k_B T}\right)\right\rangle - \ln\left\langle \exp\left(-\frac{\Delta U_-}{k_B T}\right)\right\rangle \tag{3.10}$$

Here V is the volume of the box. ΔV_i is the size of the volume change, and i denotes the direction of the volume change, with + being expansive and − being compressive. ΔU_i is the change in potential energy due to the volume change, i. The first term on the right hand of Eq. 3.10 is the pressure due to an ideal gas of monomers. The second and third terms are the monomer excess pressure, but the desired quantity is the chain excess pressure. This quantity allows thermodynamic integration to yield the excess free energy.

To accomplish this, we use arguments found in K.G. Honnell, *et al.*[158] The monomer excess pressure, p^m_{EXC}, is defined as:

$$p^m_{\mathrm{EXC}} = \ln\left\langle \exp\left(-\frac{\Delta U_+}{k_B T}\right)\right\rangle - \ln\left\langle \exp\left(-\frac{\Delta U_-}{k_B T}\right)\right\rangle \tag{3.11}$$

As the concentration approaches 0, the intermolecular forces should become negligible, which means the pressure should approach the value for an ideal gas of chains. For this to be true, Eq. 3.11 has to approach $\{[(n_{P+} + n_{P-})\, k_B T/V] - [(N n_{P+} + N n_{P-})\, k_B T/V]\}$ in this limit. If this expression is subtracted from Eq. 3.11, then the chain excess pressure, p^c_{EXC}, is recovered:

$$\begin{aligned} p^c_{\mathrm{EXC}} = {} & \ln\left\langle \exp\left(-\frac{\Delta U_+}{k_B T}\right)\right\rangle - \ln\left\langle \exp\left(-\frac{\Delta U_-}{k_B T}\right)\right\rangle \\ & - \{[(n_{P+} + n_{P-})\, k_B T/V] - [(N n_{P+} + N n_{P-})\, k_B T/V]\} \end{aligned} \tag{3.12}$$

This excess pressure can be used to calculate excess free energies.

3.3.5 Phase Diagram Calculation from Simulation Calculation

The excess free energy per volume can be defined as:

$$f_{\mathrm{EXC}}\left(\{\phi_i\}\right) = \frac{F_{\mathrm{EXC}}\left(\{\phi_i\}\right)}{Vk_BT} = \phi_P \int_{\phi_S^0,\phi_P^0}^{\phi_S^0,\phi_P} \frac{Vp^c_{\mathrm{EXC}}\left(\phi_S^0,\phi'_P\right)}{N_{\mathrm{pat}}k_BT\phi'_P} d\phi'_P + \int_{\phi_S^0,\phi_P}^{\phi_S,\phi_P} \mu_{\mathrm{EXC},S}\left(\phi'_S,\phi_P\right) d\phi'_S \tag{3.13}$$

where $N_{pat} = f_C\, n_{P+}\, N + (1 - f_C) n_{P+} N(\sigma_0/\sigma_\pm)^3 + n_{P+} N$. ϕ_i^0, with $i = S$ for salt and $i = P$ for polymer, is the reference volume fraction, which we set to 0, and, $\mu_{\mathrm{EXC},S}$ is the salt chemical potential, calculated via Widom insertion of a pair of salt ions.[159] This excess free energy can be used as an input into a total free energy expression:

$$\frac{\mathcal{F}}{Vk_BT} = \sum_i \frac{\phi_i}{N_i} \ln \phi_i + f_{\mathrm{EXC}}\left(\{\phi_i\}\right) \tag{3.14}$$

The first term on the right-hand side of this equation is the mixing entropy of all species, and the second term is the simulation-calculated excess free energy. This free energy can be used to calculate phase diagrams, shown in Figure 3.6 for patterns A-J as described in Figure 3.1d.

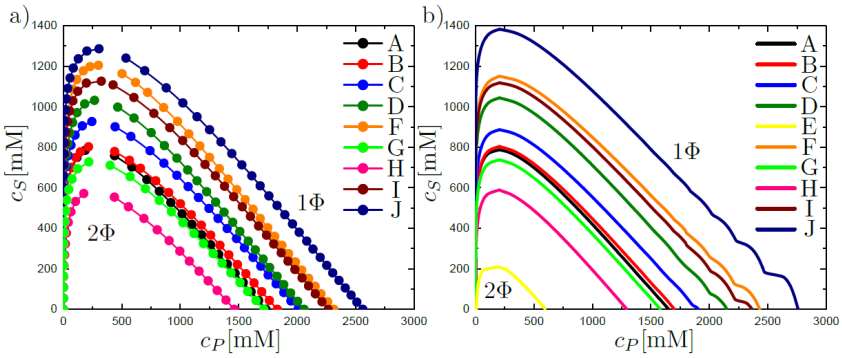

Figure 3.6. Phase diagrams for the investigated patterns. The 2Φ region is the immiscible part of the phase diagram, and the 1Φ region is the miscible part of the phase diagram. **(a)** Simulation phase diagrams calculated using equation 14. We note that sequence E did not exhibit phase separation in simulation. **(b)** Theoretical phase diagrams calculated using the transfer matrix theory. The letters corresponding to each phase diagram denote the pattern in Figure 3.1d. Both simulation and theory show alterations in phase behavior as charge fraction and the average length of the run of charged monomers is changed.

Comparison of these phase diagrams with those contained in Chapter 2[1] reveals some differences. We attribute the discrepancy to the different techniques used to calculate the excess free energy. Previously, the excess free energy was calculated via:

$$f_{\mathrm{EXC}}\left(\{\phi_i\}\right) = \int_{\phi_S^0,\phi_P^0}^{\phi_S^0,\phi_P} \mu_{\mathrm{EXC},P}\left(\phi_S^0,\phi_P'\right) d\phi_P' + \int_{\phi_S^0,\phi_P}^{\phi_S,\phi_P} \mu_{\mathrm{EXC},S}\left(\phi_S',\phi_P\right) d\phi_S'$$

(3.15)

Here, excess chemical potentials are calculated for the polymer using incremental Widom insertion.[160] In order to adapt this technique to the patterned polycation, the pattern is shifted along the polymer backbone to capture the contribution of the charged and neutral monomers to the excess chemical potential.[136] This resulted in phase diagrams with a larger polymer concentration in the supernatant phase compared to the current results. However, both techniques qualitatively capture the observed patterning trends.

3.3.6 Peptide Synthesis

Polypeptides with were prepared using standard Fmoc-based solid-phase synthesis[90] on a Liberty Blue automated microwave peptide synthesizer from CEM, Ltd. using methods reported previously.1 Briefly, peptides were synthesized on a Rink amide MBHA resin (Peptide Solutions) using Fmoc-L-Lys(Boc)-OH, Fmoc-D-Lys(Boc)-OH, Fmoc-L-Glu(tBu)-OH, Fmoc-D-Glu(tBu)-OH, and Fmoc-Gly-OH (Peptide Solutions, LLC). 20% piperidine (Sigma Aldrich) in N,N-dimethylformamide (DMF, sequencing grade, Fisher BioReagents) was used for Fmoc deprotection, while 0.5 M N,N-diisopropylcarbodiimide (DIC, 99% Acros Organics) and 1 M ethyl (hydroxyimino)cyanoacetate (Oxyma, Peptide Solutions) in DMF were used as activator and base, respectively. Cleavage from the resin and side-chain deprotection was performed in 95/2.5/2.5 trifluoroacetic acid (TFA, Fisher)/water (MilliQ 18.2 MΩ.cm, Milli- pore)/triisopropylsilane (98%

Acros Organics) for 3 hours at room temperature. The resulting peptides were precipitated into cold anhydrous ethyl ether (BHT stabilized, Fisher Scientific). The final product was characterized by matrix-assisted laser desorption/ionization time of flight mass spectrometer (MALDI-TOF, Bruker UltrafleXtreme).

Poly(glutamate) with degree of polymerization N = 50 was synthesized using amino acids of alternating chirality (D and L) to mitigate inter-peptide hydrogen bond formation.[23,91,92,136] Similarly, all patterned poly(lysine-co-glycine) peptides were synthesized using amino acids of alternating chirality (D and L), with the exception of sequences A-C. Lysine peptides are present as TFA salts, while glutamate has a sodium counterion.

3.3.7 Preparation of Stock Solutions

Polypeptide stock solutions were prepared gravimetrically using Milli-Q water at a concentration based on the total number of amino acids present. For instance, a stock solution of the homopolyanion poly(glutamate) of 10 mM amino acid would be used in parallel with a stock solution of a half-charged poly(lysine-co-glycine), also at 10 mM with respect to the total number of amino acids, or 5 mM with respect to the number of charged monomers present in solution. All solutions were adjusted to pH = 7.0 ± 0.03 using concentrated solutions of HCl and NaOH, as needed. Monomer concentration was chosen as the experimental basis in order to easily enable direct stoichiometric comparison of the number of positively and negatively charged units present in solution.

Sodium chloride (NaCl) was purchased as a powder from Sigma Aldrich. A stock solution was prepared gravimetrically at 0.5 M and adjusted to pH = 7.0, as above.

3.3.8 Coacervate Preparation

Complexation was performed using stoichiometric quantities of positively and negatively charged polypeptides at a total charged residue concentration of 1 mM at pH 7.0. Under these

conditions, it is a reasonable approximation to describe all of the residues on both polypeptides as fully charged. Samples were prepared by first mixing a concentrated solution of NaCl with MilliQ water in a microcentrifuge tube (1.5 mL, Eppendorf), followed by the polyanion. The resulting mixture was then vortexed for 5 s before addition of the polycation. The final mixture was vortexed for at least 15 s immediately after the addition of polycation to ensure fast mixing. The resulting phase separation causes the sample to take on a cloudy, or opalescent appearance, due to the formation of small droplets of the complex coacervate phase.

3.3.9 Determination of Salt Resistance ($c_{S,E}^{0}$)

Samples were examined using brightfield optical microscopy (EVOS XL Core, Fisher Scientific) to determine the 'salt resistance' ($c_{S,E}^{0}$), or the salt concentration above which no phase separation occurs. All samples were imaged within 1 h of preparation. Error bars on measurements of the salt resistance correspond to the salt concentration intervals over which samples were examined.

3.3.10 Salt Resistance ($c_{S,E}^{0}$) versus Critical Salt Concentration (c_{S}^{0})

In this chapter, we simultaneously use salt resistance $c_{S,E}^{0}$ as the experimental measure and the critical salt concentration c_{S}^{0} as the theoretical/computational measure of the strength of electrostatic interactions and thus coacervation. These values represent different parts of the phase diagram, and therefore have *different* numerical values. The motivation to use different values stems from practical or theoretical challenges in each method:

Experimental efforts rely on solid-phase synthesis of polypeptides, which produces small quantities of highly-precise, sequenced polymers that also have a relatively short degree of polymerization $N \approx 50$. The limits on the *amount* lead to practical challenges in characterizing the entire coacervate phase diagram, where the critical point for these polymers is predicted to be at

rather high polymer concentrations $c_P \approx 100 - 500$ mM. Instead, we find the location of the binodal at much lower polymer concentration of $c_P = 1$ mM where less overall polymer material is required, providing the value of $c_{S,E}^0$ used in the chapter.

Simulation determination of the binodal uses thermodynamic integration (described earlier) to calculate the phase diagram. To perform this calculation, a discrete number of simulations were carried out at regularly spaced salt/polymer concentrations, where excess chemical potentials and pressures were calculated. Polynomial surface fits to these discrete data points were used in the integration, over the entire range of c_P and c_S. While we numerically observe that these fits provide an excellent description of the free energy landscape, the low end of the binodal is expected to be the *most* sensitive to the nature of this fit due to its dependence on only a few of the original discrete simulations. As we will show later, we are still able to obtain excellent qualitative agreement with trends and even nearly quantitative agreement with experimental observations. We expect the critical salt c_S^0 to be a more robust measure of the overall free energy landscape and consequent phase diagram we obtain.

Theoretical determination of the binodal is limited by the assumptions in the transfer matrix theory. A major assumption, outside the local arrangement of correlated charges that is described by the ion-pairing in the adsorption picture, is that the local environment of the polymer and salt species is well-described by a mean field. This type of assumption is known to be inaccurate, due to the existence of 'paired' polyelectrolytes at low c_P; here, the local concentration of the oppositely-charged polymer is significantly enhanced over the mean field prediction. In our model, this manifests as a difference in the effective translational entropy of the polymer; in the mean-field approximation, each polymer exhibits full translational degrees of freedom, while the established presence of paired complexes in the dilute regime[140] would result in each *pair* exhibiting full translational degrees of freedom. This means that the theory, while qualitatively capturing the same competition between translational entropy in the supernatant and pairing energy and entropy in the

coacervate, slightly over-predicts the c_S location of the dilute-branch of the binodal at a given c_P. This effect is significant in the region for which $c_{S,E}^0$ is used, motivating our use of the critical salt concentration c_S^0 as a more accurate metric that is seen in Figure 3.9 to match well with simulation predictions.

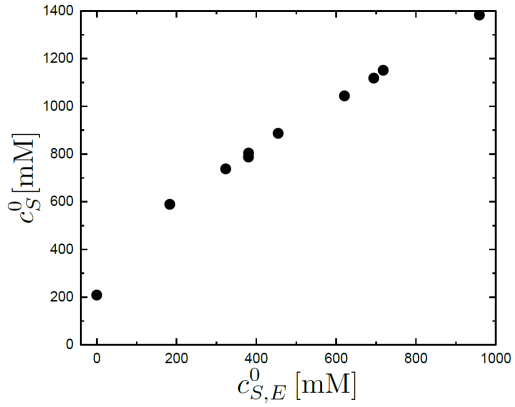

Figure 3.7. The values of the critical salt concentration c_S^0 versus the salt resistance $c_{S,E}^0$ for theoretical predictions of the entire set of sequences considered in this chapter. We demonstrate a linear correlation between these values, except at the lowest c_S^0, where the binodal is always $c_P > 1$ mM.

While the values $c_{S,E}^0$ and c_S^0 are numerically different, we can demonstrate that these values are both highly correlated. We plot in Figure 3.7 both values for the theoretical phase diagrams, for which we have the most data for both $c_{S,E}^0$ and c_S^0. While there is not a one-to-one numerical matching (which is not expected), we do demonstrate that there is an extremely linear correlation so long as the binodal passes below $c_P = 1$ mM. Therefore, trends in one value correspond *directly* to trends in the other.

We can further demonstrate that the parameterization that we use for simulation and theory predicts phase diagrams that are *numerically* similar to the experimental observations. This is slightly obscured by the use of $c_{S,E}^0$ versus c_S^0, which we motivated in the preceding paragraphs. To demonstrate this connection, we plot the value of $c_{S,E}^0$ for both simulation and experiment in Figure 3.8. We note, as previously discussed, that the values of $c_{S,E}^0$ for simulation are not predicted to be as precise as c_S^0. Nevertheless, the numerical values are similar to those obtained in experiment.

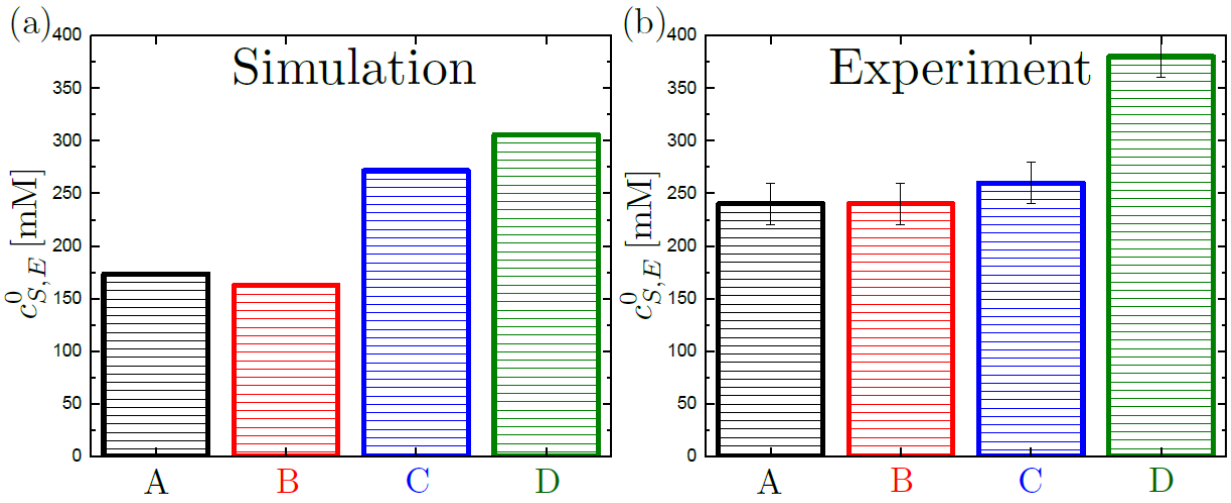

Figure 3.8. The values of the salt resistance $c^0_{S,E}$ for **(a)** simulation predictions and **(b)** experiment for sequences A-D. We note that, for our parameterization scheme, these exhibit reasonable numerical matching. We note that this measurement is not *precise* for simulation, motivating our use of c^0_S.

3.4 Results and Discussion

3.4.1 Polycation Sequence Space

We show in Figure 3.1d a schematic of the total range of polycation sequences we use in this chapter, along with the fully charged homopolyanion that was paired with the polycations in each coacervate. Experimentally, these sequences were prepared using solid phase synthesis of poly(lysine-co-glycine) and poly(glutamate). All of these sequences have between 48 and 50 monomers, with a variety of charge fractions f_C and an average length "run" of charged monomers $\langle n_r \rangle$, indicated on Figure 3.1d. We note that these types of averaged variables do not uniquely define a sequence; for example, sequences C, L, M, and N have the same total number and type of runs, only spaced out with different combinations of neutral monomer runs or "spacers." Therefore, to identify the different sequences, we assign a letter to them in Figure 3.1d that will be used to denote points associated with a given sequence later in the chapter. We do point out a few sequence-based trends that we will focus on: (Blockiness) we change the periodicity of sequence polymers with the same number of charged, neutral monomers in runs (A−D). This trend was the basis of our

prior work.[136] (Constant Runs) we examine a constant set six runs of four adjacent, charged monomers and change how the neutral spacer monomers are distributed in-between (C, K−M, D). (Constant Spacers) we keep a constant set of six runs of four neutral monomer spacers and change how the charged monomers are distributed in- between (C, N−P, D). Finally, (Constant Runs, Constant Number of Charges) we keep a constant set of runs of four adjacent, charged monomers and change the number of neutral monomer spacers while keeping the overall number of charges per chain constant (not included in Figure 3.1d, but represented later). We note that, for this chapter, all polymers are monodisperse in size *and* sequence in both theory and simulation, and have very low polydispersity in experiments.

3.4.2 Simulation and Experiment Exhibit Sequence-Dependent Coacervation

In looking to understand the nuanced effects of chemical sequence, we first performed a direct comparison between simulation and experiment. Coacervate phase diagrams were calculated using thermodynamic integration of Monte Carlo simulations[95] using a combination of box size-changes[157,158] and Widom insertion[158,159] to calculate the excess free energy along both the polymer (polyanion and sequenced polycation) and salt species respectively. This approach uses the same simulation model as reported previously.[72–74,136] This model uses a bead−rod representation of charged polymers in an implicit solvent, which is a standard coarse-grained approach that highlights the physical effects due primarily to electrostatics and is agnostic to any specific chemistry. We can qualitatively compare the binodal phase diagrams resulting from these simulations to experimentally determined measures of the phase behavior (Figure 3.9).

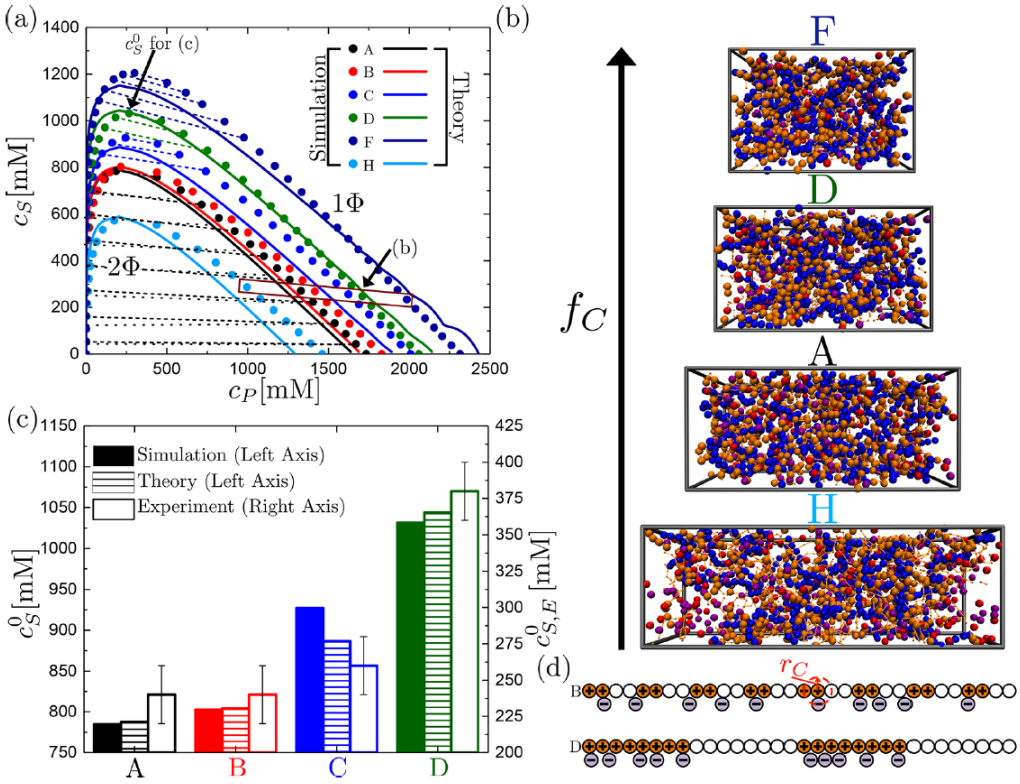

Figure 3.9. (a) Salt concentration c_S versus polymer concentration c_P phase diagram of coacervation measured from simulation (points) and transfer matrix theory (lines) for polycations with sequences A−D, F, and H interacting with a homopolyanion. An example set of tie lines are shown for sequence A (dashed line, simulation and dotted line, theory), with both exhibiting a small negative slope consistent with prior literature.[72,151] Simulation tie lines are also shown for other sequences at concentrations outside the binodal of sequence A, demonstrating that sequence does not alter the sign of the slope. The critical salt concentration as measured by theory c_S^0 is measured at the largest concentration of salt observed in the supernatant phase for each sequence. **(b)** Simulation snapshots representative of the points in **(a)** for sequences H, A, D, and F. The polycation is orange, the polyanion is blue, the cation is purple, and the anion is red. Neutral beads for the polycation are shown with smaller beads connected by rods. **(c)** Simulation and theory values for salt resistance (left axis, c_S^0) qualitatively compare well with experimentally measured values of $c_{S,E}^0$ obtained at 1 mM polymer for sequences A−D, showing that we can use theory and simulation to capture sequence variations described by an increase in charge block size (Blockiness). **(d)** Schematic highlighting counterion localization for two different sequences. For a sequence with a large $\langle n_r \rangle$ (D), the counterions are locally confined near the charged blocks. In contrast, counterions are more uniformly localized along the chain for sequences with a small $\langle n_r \rangle$ (B). The red circle represents the cutoff radius, r_C. If a salt ion is within this r_C of a monomer, the salt ion is considered localized.

The phase boundaries in Figure 3.9a exhibit the same trend observed in Chapter 2,[136] with minor differences due to the different methods for calculating phase diagrams. Our results highlight that an increase in blockiness $\langle n_r \rangle$ and charge fraction f_C generally leads to a marked increase in the two-phase region of the phase diagram, indicating that phase separation is enhanced by stronger electrostatic attractions. Figure 3.9b shows characteristic snapshots from simulations performed at a constant number of charged monomers for sequences H, A, D, and F, visually highlighting how an increased value of c_S^0 leads to stronger phase separation and a denser coacervate phase.

Further analysis of simulation results also suggested that electrostatic cooperativity resulting from an increase in $\langle n_r \rangle$ enhances the localization of counterions at high charge-density locations along the polyelectrolyte chain (Figure 3.9d). An important consequence of this increase in counterion confinement is a commensurate increase in the entropy resulting from the release of these bound counterions upon complexation with an oppositely charged polymer.[136]

Because of the correlation between increases in the strength of the electrostatic attraction, counterion localization, and the size of the two-phase region, we can use the highest salt concentration where we observe phase separation, c_S^0, as a simple descriptor of the system (Figure 3.9a). This parameter also allows for comparison with experimental data, via the "salt resistance" $c_{S,E}^0$ which is the salt concentration at which miscibility is observed for a fixed overall polymer concentration c_P = 1 mM. c_S^0 and $c_{S,E}^0$ represent different parts of the phase diagram and thus have different numerical values; however we show in Section 3.2 that they are highly correlated and can be used to compare qualitative trends. The reasoning for using these different quantities is discussed in Section 3.2, along with the demonstration that direct comparison of simulation and experimental values of the same metric ($c_{S,E}^0$) indeed yields similar numerical results. Figure 3.9c demonstrates that the size of the two-phase region, as measured by either the salt resistance $c_{S,E}^0$ from experiments or c_S^0 from simulations, systematically increased with increasing blockiness $\langle n_r \rangle$ for constant charge fraction f_C, (*i.e.*, sequences A−D).

The results in Figure 3.9a also include example tie lines connecting coexisting coacervate and supernatant phases. It is noteworthy that we observe tie lines with a negative slope, indicating that the coacervate phase has a lower salt concentration than the supernatant.[69,72–74,151,161] This preferential partitioning of salt out of the dense, polymer-rich coacervate phase has been previously attributed to the excluded volume of the polyelectrolyte species,[69,72–74,151,161] and has been confirmed experimentally.[72,151]

3.4.3 Theory of Monomer Sequence in Polymeric Complex Coacervation

Results from simulations suggested that we can capture the relevant physics dictating the effects of charge sequence on coacervate phase behavior by considering how counterions interact with a single polymer chain. Therefore, we extend the transfer matrix theory of complex coacervation to include the effects of charged monomer sequence.[69,73,74] This method is particularly applicable because, for most coacervates, the concentration of charged species is sufficiently high that standard Debye−Hückel or Poisson−Boltzmann electrostatics are no longer applicable,[72,137,162] and correlations are primarily due to charge connectivity and nearest-neighbor pairing.[72,163]

To extend the transfer matrix formalism to describe sequence effects in coacervation, the electrostatic association strength ϵ becomes a function of the specific monomer position along the test polycation chain. This accounts for the variation in local electrostatic environment, and specifically the energetic penalty for an unpaired ion, for a particular monomer sequence.[69,73] Thus, the $D_{\text{homo}} = D_0 e^{-\epsilon_1(s)}$ that in the homo-polyelectrolyte theory contains a constant ϵ_0, now is written with a contribution ϵ_1 that depends on the monomer index s, $D_{\text{pattern}} = D_{homo} e^{-\epsilon_1(s)}$.

To calculate the value of $\epsilon_1(s)$, we use Monte Carlo simulations of single polyelectrolytes in a dilute salt solution to determine the adsorption characteristics of a test polyelectrolyte it in a reservoir of salt ions. The localization of salt ions near charged polycation blocks, and thus the local strength of electrostatic interactions, is calculated by defining a region around the chain

defined by a cutoff radius r_C (Figure 3.9d).[114] This charge localization is energetically favorable due to electrostatic attractions,[114,164,165] and there is thus an increased number density $n_C(s)$ of opposite charges within r_C at a given chain monomer s.[136] We define an electrostatic energy that accounts for this increase in local correlations as the aforementioned $\epsilon = \epsilon_0 + \epsilon_1(s)$. We demonstrate that $\epsilon(s)$ can be determined from simulation using the relationship $\epsilon(s) = -\ln n_C(s)/ n_{C,0}(s)$, where $n_{C,0}(s)$ is the number density of opposite charges within r_C in the absence of electrostatic interactions. This method thus only requires two single-chain simulations (one with electrostatics and one without) at low (but nonzero) salt concentrations, and we show in Section 3.2 that the value of $\epsilon(s)$ is independent of the choice of salt concentration in this limit. Figure 3.10a shows typical landscapes ($\epsilon(s)$) for patterns A−D, as well as the homopolyanion, where we denote charged monomers with closed symbols and neutral monomers with open symbols. We take $D_0 = 1$ and $\epsilon_0 = 0$, in agreement with the theory for homo-polyelectrolyte coacervates.[69]

As expected, there is a large variation in electrostatic attraction along the contour of the chain due to the precise sequence of monomers. For the sequences plotted in Figure 3.10a, sequence D exhibits the most marked variations in $\epsilon(s)$. In this case, long runs of adjacent, charged monomers (*e.g.*, s = 16−23 and s = 32−39) have a value of $\epsilon(s)$ that is similar to $\epsilon(s)$ for a homopolymer. As the sequence transitions from a charged run to a neutral spacer (*e.g.*, s =22−26), there is a concomitant increase in $\epsilon(s)$ that we attribute to the weakening of the driving force for charge localization. $\epsilon(s)$ decreases once more as the neutral spacer transitions back to a charged run (*e.g.*, s = 30 to 34). In contrast, short runs of charge or isolated, charged monomers (such as in sequences A or B) show weak localization. This is indicated by a larger value of $\epsilon(s)$ with weaker oscillations. These energy landscapes $\epsilon(s)$ inform our model of sequence effects in complex coacervation.

We define a new transfer matrix, that now depends on the monomer index via the sequence-dependent epsilon:

$$\mathbf{M}_s(\epsilon(s)) = \begin{bmatrix} A_0\phi_S & A_0\phi_S & A_0\phi_S & A_0\phi_S \\ 0 & 1 & 2 & 0 \\ B_0\phi_P & B_0\phi_P & B_0\phi_P & B_0\phi_P \\ D_0e^{-\epsilon(s)} & D_0e^{-\epsilon(s)} & D_0e^{-\epsilon(s)} & D_0e^{-\epsilon(s)} \end{bmatrix} \tag{3.16}$$

This transfer matrix is specifically for monomers that contain a *charge*, in contrast to neutral monomers along the chain. We consider neutral monomers to only affect the free energy of coacervation through (i) excluded volume of the monomer units and (ii) through their spacing of charges and its effect on $\epsilon(s)$ for those monomers. Neutral monomers are otherwise not required to "pair" with an opposite charge, and their contribution to the transfer matrix calculation is as an identity matrix $\mathbf{M}_n = \mathbf{I}$. We can use this set of matrices to write a new *grand canonical partition function* $\Xi_{\text{seq}}^{\text{int}} = \prod_s^{N_p}(\mathbf{M}_s(\epsilon(s))(1-\delta_{Z_s}) + \mathbf{M}_n\delta_{Z_s})$. This can be simplified, since when $\delta_{Z_s} = 1$ for neutral monomers, the product is simply an identity matrix. This means that the system can be divided into a product over a series of charge "runs", or adjacent charges, of length n_r.

$$\Xi_{\text{seq}}^{\text{int}} = \left[\prod_{\text{runs}}^{n_r}\left[\vec{\psi}_0^{\,T}\left(\prod_{s>1}^{n_r}\mathbf{M}_s(\epsilon(s))\vec{\psi}_1(\epsilon(s))\right)\right]\right] \tag{3.17}$$

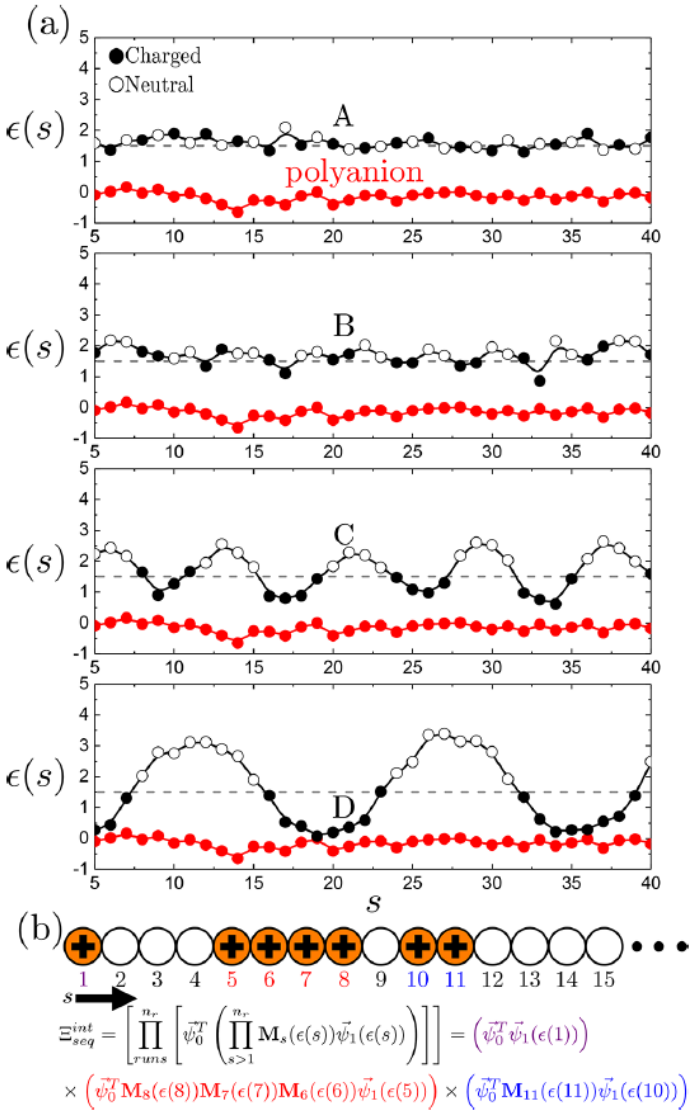

Figure 3.10. (a) Monomer-dependent energy $\epsilon(s)$ as a function of the chain index, measured by single-polyelectrolyte simulations in dilute salt solution. Variations in $\epsilon(s)$ reflect the different electrostatic environments associated with monomers in different positions along the chain. $\epsilon(s)$ is plotted here for sequences A−D, which reflects variation in sequence periodicity ranging from alternating charged/uncharged monomers (A) to blocks of eight charged/uncharged monomers (D). Filled symbols represent charged monomers in the sequence, and open symbols represent neutral monomers. The homopolyanion is also plotted as the dark red line in each graph. We note that, for the blockiest polycation sequences, $\epsilon(s)$ approaches the homopolyanion behavior in the center of the block. **(b)** Schematic illustrating how the variation in $\epsilon(s)$ is incorporated into the transfer matrix theory. $\Xi_{\text{seq}}^{\text{int}}$ is the grand canonical partition function associated with polymer-polymer interactions. It is composed of products of "runs" of charge, as shown explicitly in the expression given below the schematic; here, the colors are associated with the indicated charged monomer runs: 1 (purple), 5−8 (red), and 10−11 (blue).

We schematically show how this calculation is carried out in Figure 3.10b. The new interaction free energy contribution for a patterned polymer (in this case, a polycation) is $\mathcal{F}_{\mathrm{seq}}^{\mathrm{int}}(\{\epsilon(s)\}/(Vk_BT) = \phi_{P+}\ln(\Xi_{\mathrm{seq}}^{\mathrm{int}})/2f_CN_{P+}$. We thus use the free energy for the overall system:

$$\frac{\mathcal{F}_{\mathrm{seq}}}{Vk_{\mathrm{B}}T} = \frac{\phi_{P+}}{N_{P+}}\ln\phi_{P+} + \frac{\phi_{P-}}{N_{P-}}\ln\phi_{P-} + \phi_W\ln\phi_W + \phi_{S+}$$
$$\ln\phi_{S+} + \phi_{S-}\ln\phi_{S-} + \frac{\phi_{P+}}{2f_CN_{P+}}\ln[\Xi_{\mathrm{seq}}^{\mathrm{int}}(\{\epsilon(s)\})]$$
$$+ \frac{\phi_{P-}}{2N_{P-}}\ln[\psi_0^T\mathbf{M}_0^{N_P-}\psi_1] + \zeta(\phi_S + \Lambda_{P+}\phi_{P+} + \Lambda_{P-}\phi_{P-})^3 \quad (3.18)$$

Here, the sequence-dependence is almost completely contained within the interaction term for the polycation, while the homopolyanion is treated as in the previous transfer matrix theory.[69] In this chapter we use the parameters A_0 = 35.0, B_0 = 11.5, $\Lambda_{P+} = \Lambda_{P-}$ = 0.84375, and ζ = 16.0; these are similar to values in prior work[69,73] but with small changes reflecting slight differences in how we model Λ. The same parameters are used for all sequences considered in this chapter.

3.4.4 Sequence-Based Transfer Matrix Theory Can Match Experimental and Computational Phase Behaviors

Full theoretical phase diagrams are calculated for the polyelectrolyte patterns. These demonstrate excellent, nearly quantitative matching with the full simulation phase diagrams shown in Figure 3.9a. In particular, we can capture how the phase diagram changes with increasing blockiness for the constant f_C = 0.5 sequences (A−D) in simulation, experiment, and theory. This is shown in Figure 3.9c. In particular, this matching includes the significant jumps in c_S^0 from B to C and C to D, concomitant with the emergence of significant variations in $\epsilon(s)$ in Figure 3.10a.

We showed this charge blockiness effect in simulation in Chapter 2,[136] which was attributed to the one-dimensional confinement of charges localized along the backbone. This emerges from our theory because the energetic parameter $\epsilon(s)$ (Figure 3.10a) corresponds to a local one-dimensional confinement potential for counterions along the chain.

We extend this matching to the entire set of sequences considered in Figure 3.1d. In Figure 3.11a, we plot the experimental $c_{S,E}^0$ as a function of the overall charge fraction f_C for sequences A–J, for coacervates formed in a NaCl salt solution from sequence-controlled polymers of poly(lysine-co-glycine) in complex with a homopoly(glutamate). We observe large variations in $c_{S,E}^0$, ranging from 160 to 580 mM NaCl, showing that charge patterns can significantly alter the strength of electrostatic interactions. We obtain the values of c_S^0 from simulation and theory for this same, extended set of sequences (full phase diagrams included in Figure 3.6) and also plotted versus f_C in Figure 3.11b. Both simulation and theory results exhibit nearly quantitative matching and exhibit qualitative matching with the experimental values observed in Figure 3.11a.

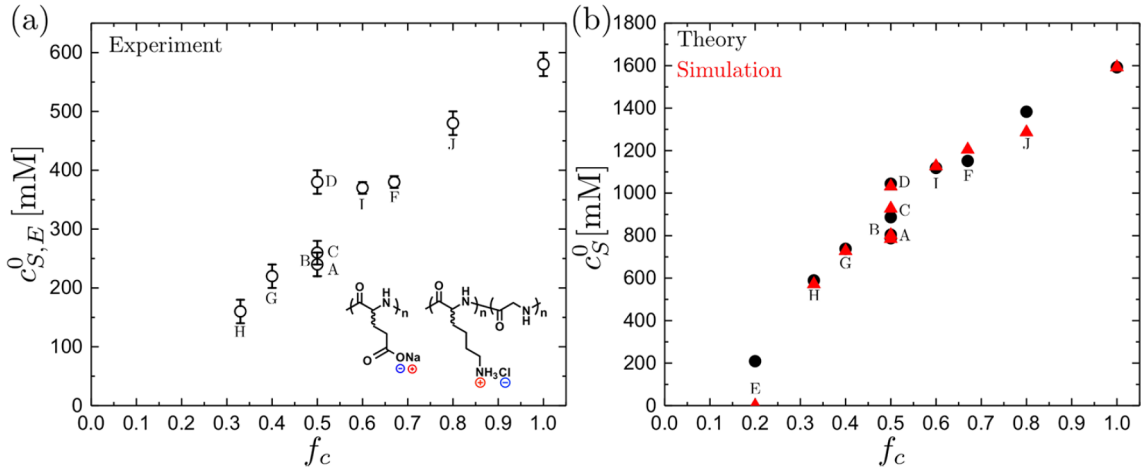

Figure 3.11. (a) Experimental salt resistance $c_{S,E}^0$ as a function of charge fraction f_C for sequences A–J, prepared using systems of poly(lysine-coglycine) in complex with poly(glutamate) in a NaCl salt solution (inset), and also a homo-polyelectrolyte coacervate f_C = 1. We note that experimental data for sequence E is not included, because only solid precipitation is observed and thus $c_{S,E}^0$ is not accessible. **(b)** Theoretical (black circles) and simulation (red triangles) salt resistance c_S^0 as a function of charge fraction f_C for sequences A–J. We note that simulation and theory are in nearly quantitative agreement, and both qualitatively agree with the experimental trends in **(a)**.

Experiment, theory, and simulation all exhibit the same trends. Broadly speaking, high values of f_C lead to larger values of $c_{S,E}^0$ (experiment) and c_S^0 (theory and simulation), corresponding to higher strengths of electrostatic interactions. This is expected, given that there are

more charges per chain and thus more electrostatic attraction to the oppositely charged polymeric species. Nevertheless, we note that even among the same charged fraction there can be a wide variation in $c_{S,E}^0$ and c_S^0, as apparent in the blockiness trend at f_C = 0.5. The opposite situation is also true, with similar values of c_S^0 being observed for different values of f_C. For example, we note that the trio D, I, and F or the pair G and A show a similar value of $c_{S,E}^0$ despite having different charge fractions. These particular cases generally represent a trade-off between blockiness and charge fraction, with less f_C needed if the sequences have longer blocks. We are able to accurately capture this effect of precise charge sequence on the phase behavior of complex coacervates with both theory and simulation because our theory considers the particular charge sequence rather than average sequence metrics such as charge fraction f_C or blockiness $\langle n_r \rangle$.

3.4.5 Sequence-Based Trends

Having looked at the effect of blockiness, we tested the ability of this theory to capture nonregular sequences. In particular, we show this by keeping the total charge fraction f_C = 0.5 constant and maintaining constant runs of four charges while varying neutral spacers (sequences C, K−M, and D, *i.e.*, constant runs). These systematically shrink the length of one neutral spacer while increasing the length of another (see schematic in Figure 3.12a). We do this for charge runs of length n_r = 4, which represents a transition between $\langle n_r \rangle$ = 4 and $\langle n_r \rangle$ = 8 (sequences C and D) at the extremes. Despite controlling for both f_C and $\langle n_r \rangle$, this variation results in a marked change in the values of c_S^0 and $c_{S,E}^0$ for theory and experiment. This is plotted in Figure 3.12a (circular symbols) as a function of the larger neutral linker length ν and demonstrates that there is a transition from C to D where intermediate values of c_S^0 are observed. We attribute this change to the proximity of charge runs, which still affect each other even when separated by a few neutral monomers, a cooperative effect that decreases with increasing length of the neutral spacer. Indeed, this is observed in both experiment (open, black points, $c_{S,E}^0$) and theory (filled, red points, c_S^0).

The next set of sequences we highlight are C, N−P, and D. This example of a constant spacers series is the inverse of the constant run trend and is characterized by constant spacer length (four neutral monomers) with variation in charged runs at a constant $\langle n_r \rangle$ = 4 and f_C = 0.5. Here we observe a similar transition between the limiting sequences C and D, plotted in Figure 3.12a as triangular symbols.

We note for both the constant run and constant spacer series, the increase in $c_{S,E}^0$ and c_S^0 is more abrupt as the longer charge-run length ν is increased from ν = 7 to ν = 8, which is again observed in both experiment and theory. This demonstrates that there is a large differential effect of moving an isolated charged (P to D) or neutral monomer (M to D) in a larger run of the other monomer type. This is especially apparent in the P to D transition, which we attribute to the lack of electrostatic cooperativity of the isolated charged monomer with respect to its neighbors in P; upon "promoting" that monomer to be in the long, charged block in D it gains the cooperative electrostatic attractions associated with these blocks.

We consider a final constant runs, constant number of charges series, where runs of four adjacent charges along the polycation have differing numbers of neutral monomers, only now the chain length N_{P+} is increased to have a constant number of charged positive charges along the polycation. This runs from two to eight monomers between groupings of four charged monomers. We plot $c_{S,E}^0$ and c_S^0 for these sequences in Figure 3.12b and show that they decrease with the number of neutral monomers ν for both the experiment and theory values. This further clarifies that the values of nr and the total number of charges per chain do not, by themselves, dictate the strength of electrostatic interactions. The neutral spacers, despite not being directly involved with the electrostatic interactions, affect the local charge correlations sufficiently to cause significant changes in c_S^0 and correspondingly the strength of the electrostatic attractions between the oppositely charged polyelectrolytes.

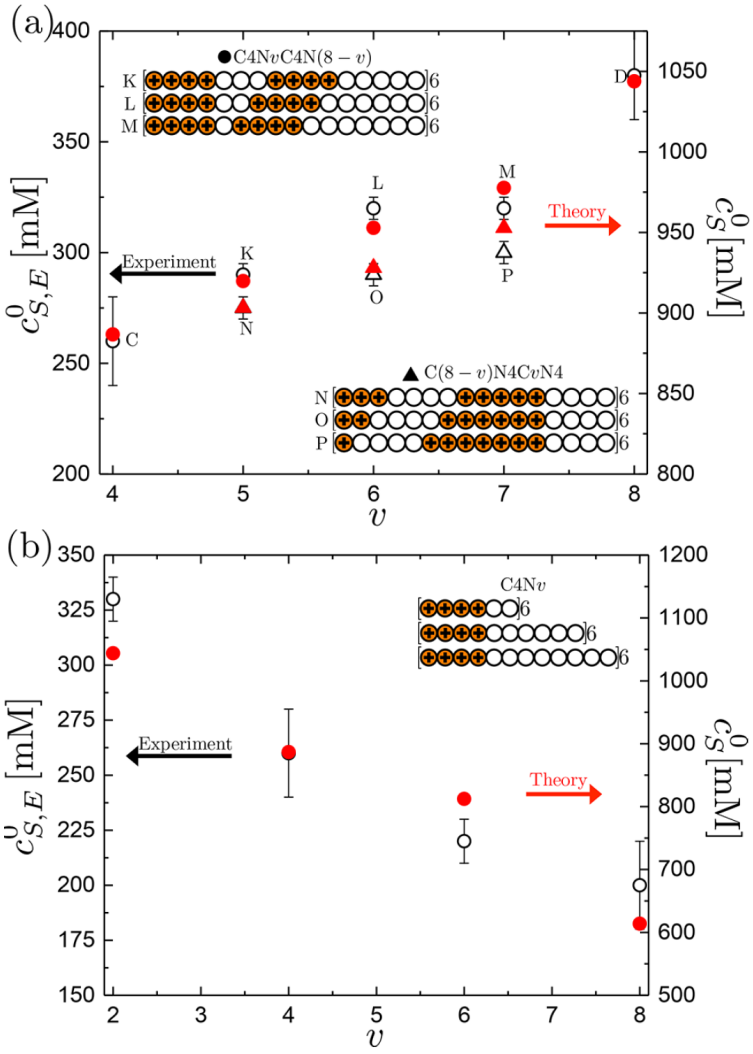

Figure 3.12. (a) Salt resistance c_S^0 for $f_C = 0.5$ with varying length neutral spacers, denoted by v and $8 - v$, between runs of four charges (circles) and with varying length charge blocks, denoted by v and $8 - v$, separated by spacers of four neutral monomers (triangles). Experiment (black), using sequence-controlled poly(lysine-co-glycine) in complex with a homo-poly(glutamate) and theory (red) exhibit qualitative matching, showing the complicated interplay between charge block separation and length. **(b)** Salt resistance for polycations with 24 total charged monomers, separated by increasingly long neutral spacers, denoted by v.

3.5 Conclusions

We have developed a theoretical framework for understanding the role of polyelectrolyte charge sequence in complex coacervates. This framework builds on a transfer matrix approach[69] that explicitly accounts for the local electrostatic environment along a sequenced polyelectrolyte via an effective energy $\epsilon(i)$. We can capture the effects of sequence in complex coacervates,

including charge fraction and charge blockiness, as well as the more subtle variations in charge associated with nonregular sequences. Furthermore, we show close matching between experiment, simulation, and theory for the wide range of sequences considered. The emerging physical picture is that there is a trade-off between the number of charges per chain and the blockiness of the sequence; however, the relative position of these blocks also plays a significant role in determining phase behavior.

This computational, experimental, and theoretical effort provides the foundation to study a whole range of polyelectrolytes and bio-polyelectrolytes with charge sequence. The next step is to incorporate other molecular interactions, such as hydrogen bonding, short-range χ-interactions and hydrophobicity, and ion-π interactions, into this theoretical framework. This is particularly relevant to biological systems such as IDPs, which are known to form phase-separated structures in the cell that are sensitive to sequence. However, this may also open the door to engineering charge sequence in synthetic polymers and to inform the self-assembly or phase behavior of soft materials.

CHAPTER 4

SEQUENCE-DEPENDENT SELF-COACERVATION IN HIGH CHARGE-DENSITY POLYAMPHOLYTES*

4.1 Abstract

Polyampholytes, which contain both positive and negative charges along the backbone, represent a classical model system for certain types of 'intrinsically-disordered proteins' (IDPs). IDPs can possess biological functionality, even in an unfolded state, including the formation of phase-separated regions within a cell; while driven by a number of interactions, electrostatic attractions are thought to be key to forming these structures. This process of electrostatically-driven liquid–liquid phase separation, known as 'complex coacervation,' can also be observed in simpler polymer or biopolymer systems. In this paper, we use a series of model polyampholytic polypeptides of increasing blockiness, that undergo 'self-coacervation' due to charge attraction between polycation and polyanion blocks along the same polymer chain. We show that these polypeptides undergo complex coacervation when sequences have at least 8–12 adjacent like charges, with increasing blockiness leading to a larger two-phase region. We simultaneously develop a theory built on the transfer-matrix formalism developed by Lytle and Sing, to show how blockiness increases the strength of electrostatic interactions and subsequently promotes phase separation. We explore a tradeoff that emerges due to the presence of 'charge-pattern interfaces' where the sequence of polyampholyte charges switches sign, and how these contrast with chain-ends in equivalent homopolyelectrolyte coacervates.

* Part of this work has been published: J. Madinya, L.W. Chang, S.L. Perry, C.E. Sing, *Sequence-Dependent Self-Coacervation in High Charge-Density Polyampholytes*, Molecular Systems Design & Engineering, (2020), (in press), DOI: 10.1039/C9ME00074G. Reproduced by permission of The Royal Society of Chemistry.

4.2 Introduction

Intrinsically disordered proteins (IDPs) are proteins that do not spontaneously fold into stable structures.[28,29] IDPs can take on a number of metastable conformations in solution, ranging from stretched coils to collapsed globules.[166] This is in contrast to globular proteins, which fold into relatively ordered structured states that correspond to their specific biological function.[167,168] This folding process proceeds from a random coiled state to the native folded structure through a kinetic 'protein folding funnel,'[169] where the final folded structure represents a global free energy minimum state that is governed by the specific peptide sequence.[170] IDP peptide sequences differ from their globular counterparts in that they tend to have fewer hydrophobic residues and have a higher proportion of charged and polar groups.[29,171] Many IDPs contain both positive and negative charged residues and at least 75% of IDPs are polyampholytes.[9] IDPs can become biologically active by interacting with a 'folding partner' to produce an ordered state,[172–174] but may also interact with other proteins to yield a disordered or partially-disordered – yet still fully functional – state. These latter interactions are typically referred to as 'fuzzy' interactions.[175–178] Nevertheless, while IDPs are characterized by their disordered native structures, the distributions of the conformations sampled are not random and are governed in part by net charge,[179,180] and charge sequence.[9] This combination of conformational flexibility and diversity of interaction modes make IDPs particularly suitable for cell signaling and regulatory functions.[181–186]

Recently, there has been great interest in understanding the critical role IDPs play in the formation of membraneless organelles through a liquid–liquid phase separation process.[186,187] The solution properties that lead to solution demixing in IDPs are encoded within the sequence of the protein.[8,9,40,188] Post-translational modifications can also lead to phase separation in IDPs, for instance phosphorylation of residues along the polypeptide chain can change the electrostatic interactions leading to demixing.[189,190] It is clear that electrostatic interactions and polypeptide sequence together figure prominently in the solution behavior of IDPs. The challenge in trying to

understand IDP solution behavior, and ultimately their function, is to include the complex diversity of interactions and sequence effects into macromolecular models.

One common approach to understanding IDPs has been to study the physical properties of analogous, model polymer systems. Polyampholytes, which are polymers containing both positive and negative charges, are particularly useful in this role due to the abundance of charged amino acids in IDPs. Polyampholyte models have long been considered in the polymer physics literature, with early work by Higgs and Joanny,[191] combining Debye–Hückel and scaling theory to develop an analytical model. Even here, the definition of the monomer sequence was a key attribute, with this case being a random distribution of negative and positive charges. Systematic study of this distribution by Dobrynin and Rubenstein[192] included a charge asymmetry parameter and an effective temperature in a Flory-type theory.

The distribution of charge sequence has taken center stage in the IDP literature, where IDP conformation can be described using a sequence charge decoration (SCD) metric[193,194] that captures the blockiness of charge. Coarse-grained simulations have been used to show connections between this SCD and single-molecule properties such as the conformational size and coil–globule transition,[195–198] and bulk phase behavior.[199–201] Similarly, recent use of random phase approximation (RPA) theory to describe polyampholyte bulk phase behavior has demonstrated that the propensity to undergo phase separation is correlated with the 'blockiness' of the charge pattern.[202,203] This has recently been extended by efforts from Danielsen, *et al.*[204] to use field-theoretic simulations capable of describing phase-separation in blocky polyampholytes. Indeed, this work is built on the key observation that polyampholyte phase separation is essentially equivalent to the associative phase separation between two separate, oppositely-charged polymers, a process known as polymer complex coacervation.[204–207] Inspired by this connection, polyampholyte phase separation is sometimes called self-coacervation.[204,205]

Complex coacervation itself has also been used as a polymer analogy to IDP-based phase separation in biological systems;[34] indeed, the physical understanding of coacervate physics

developed by the community has striking similarities[28] to the development of polyampholyte physics. The earliest work in this area combined Flory–Huggins theory of polymer mixing with the Debye–Hückel theory of dilute electrolytes,[162] resulting in the Voorn–Overbeek model.[68,70] While this theory can be fit to experimental data, it has provided the starting point for a class of field theory models[99,101–103,138,205,208,209] that seek to shore up its known limitations.[3,11,20,135] Initial efforts to use RPA-based methods were able to predict the same general phase behaviors, whilst including the connectivity between charges along a polymer chain.[101,103,138,209] These are analogous to efforts for polyampholyte systems, and culminated in the development of field-theoretic models that have now been applied to both polyampholyte and coacervate phase separation.[202–207] Similar to the development of polyampholyte physics, molecular simulation has played a key role in developing a physical understanding; this is true both at the limit of dilute polyelectrolyte complexes between two chains, as well as for bulk phase separation.[104,114,149,150,210,211]

Recent work on complex coacervation, inspired in part by the relevance to IDPs, has seen the emergence of a number of modeling approaches beyond the continuing efforts in using simulation and field theory. These have sought to further examine and account for the limitations present in many of the field theoretic approaches, and particularly the original Voorn–Overbeek theory.[68] For example, liquid-state theory models have incorporated the effects of both connectivity and the excluded volume of the molecular species.[110,141,142] Scaling models have also been developed to detail the effects of charge density and connectivity in the limit of low-charge density.[143–146] Another class of models has recently shown promise, built on physical charge condensation arguments; here, coacervation is driven by the release of salt ions that localize near isolated polyelectrolytes, but are 'released' when charge neutralization can occur through interactions with an oppositely-charged polyelectrolyte chain instead.[212] This class of models has a number of manifestations, including a semi-phenomenological 'ion equilibrium' model used by Larson and Qin[148] and a ladder conformation-based model developed by Muthukumar.[147]

Lytle and Sing have recently developed a model inspired by the concept of charge condensation, that is called the transfer matrix (TM) theory of coacervation.[14,73,74,213,214] This theory accounts for the localization of oppositely-charged small molecule ions or polyelectrolytes near a test polyelectrolyte chain, and maps this localization to a 1-D adsorption model. This versatile model has provided insights into how coacervation is affected by a number of molecular features, including charge spacing,[213] polymer stiffness and architecture,[14,74] and salt valency[74] as well as how charged block-copolymers can self-assemble via coacervation.[215] Recently, it was demonstrated that this model can be extended in a hybrid simulation/ theory scheme to arbitrary monomer sequences for one of the polyelectrolytes.[214] The effect of charged monomer sequence on coacervation predicted by this theory is consistent both with molecular simulation and results from experiment.[214]

With the exception of field theoretic and scaling models,[143–146,202–207] most of the recent insights into coacervation have yet to be applied to self-coacervation. In part, this is complicated by the key role that sequence plays in self-coacervation, which may not be resolved by many of the coacervate models. With the advent of the sequence-dependent model in the transfer matrix theory,[214] there is now an opportunity to develop a new theory of polyampholyte self-coacervation that specifically takes into account the effect of sequence. In this chapter, we extend the transfer matrix theory to consider the effect of sequence on self-coacervation, and compare to experimental trends that demonstrate the presence of a critical charge 'blockiness' where coacervation begins to be observed. The trends we observe are largely consistent with the simulation efforts by Danielsen, *et al*.,[204,216] however our alternative approach[213] is specifically designed to consider high charge-density polyelectrolytes; this limit is challenging to resolve in the field theoretic approach, due to the assumption of Gaussian-smeared charges and excluded volume that does not resolve the local charge correlations (that give rise to *e.g*. counterion condensation and ion pairing) important for modeling high charge-density polyelectrolyte systems.[204] Additionally, we demonstrate that our theoretical predictions match qualitatively with the observations from experiments on a set of

model sequence-controlled polypeptides. Our results have implications for the phase behavior of IDPs, showing that the sequence of charges in these biomacromolecules, along with environmental parameters such as salt concentration, can strongly impact phase behavior. This could also have general implications for electrostatic interactions between globule species, such as proteins or micelles. More fundamentally, we demonstrate via experiment and simulation-informed theory how electrostatics (and specifically charge patchiness) gives rise to polymer phase separation.

4.3 Materials and Methods

4.3.1 Transfer Matrix Theory

Previous work on coarse-grained simulation models of polyelectrolyte coacervation by Sing and coworkers has shown that correlations between the charged species in the coacervate phase are short-ranged.[72] This observation suggests that the thermodynamics of coacervation can be effectively captured by considering only the nearest neighbors of a test polyelectrolyte chain. This led to the development of the transfer matrix theory of coacervation.[213] Here we apply this model for polyampholyte self-coacervation. We consider a test polyampholyte chain in the presence of charged ions and other polyampholyte chains. We approximate the interactions between the particles as a 1-D adsorption model in which the monomers along the test chain are the adsorption sites onto which the oppositely-charged ion or monomers can adsorb to (Figure 4.1). This results in the following expression for the free energy of coacervation:

$$\frac{\mathscr{F}}{Vk_{\mathrm{B}}T} = \sum_i \frac{\phi_i}{N_i}\ln\phi_i + \frac{\phi_{\mathrm{p}}}{2N_{\mathrm{p}}}\ln\left[\psi_0^T \mathbf{M}_0^{N_{\mathrm{p}}}\psi_1\right] + \zeta\left(\sum_{i\neq W}\Lambda_i\phi_i\right)^3 + \sum_{ij}\chi_{ij}\phi_i\phi_j \tag{4.1}$$

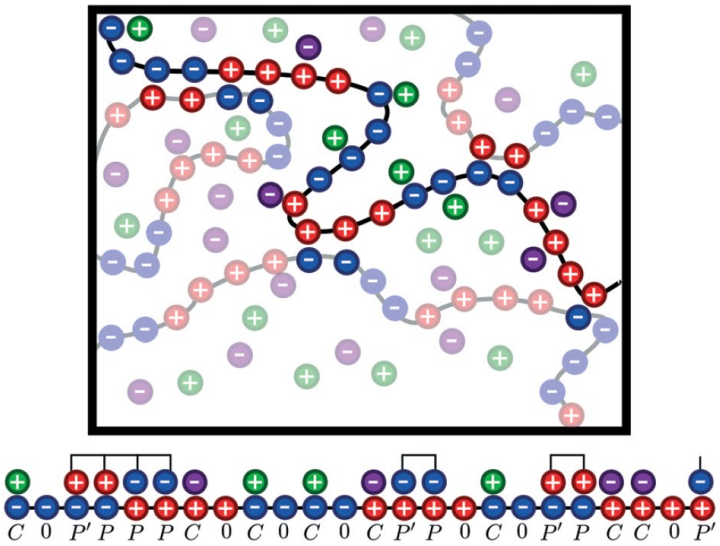

Figure 4.1. Schematic illustrating the coacervate phase of a polyampholyte solution. The opaque species represent the test the chain and its nearest neighbors. The monomers along the test chain are treated as adsorption sites onto which salt ions or monomers from other polyampholyte chains can adsorb. Walking along the test chain, each monomer is assigned an adsorption state for a salt ion C, an initial adsorbed monomer from a polyampholyte chain P', a subsequent monomer from an already adsorbed polyampholyte chain P, or no adsorbed species 0. It is preferential for the adsorbed chain to be in the coacervate phase as it allows for many more configurations of adsorption states due to the higher density of charged species.

The first term of this expression is the translational entropy of all the species $i = P, S, W$ (representing the polyampholyte, salt, and water respectively) with degree of polymerization N_i. In this work, only the polymeric (*i.e.*, the block polyampholyte and homopolyelectrolyte) species have $N_i > 1$. The second to last term is a phenomenological cubic term to capture the non-pairwise excluded volume with a magnitude governed by the parameter $\zeta = 19.0$, which is constant for this paper and parameterized based on previous simulation results.[213] The final term is the standard Flory χ term, accounting for short-range, non-electrostatic interactions. In this chapter, only the polymer and solvent interact via this Flory term with prefactor χ_{pw}; for most of the paper the value of χ_{pw} is set to zero unless explicitly stated. The prefactor Λ_i accounts for differences in per-molecule excluded volumes, and is set to $\Lambda = 0.6785$, as justified in previous works.[213,214]

The second term is the interaction free energy of the polyampholyte, and the primary result of the transfer matrix theory. This interaction free energy is derived from the grand canonical partition function, Ξ^{int}, for the polyampholyte chain interacting with its local environment. This partition function is expressed using the transfer matrix formalism, $\Xi^{\text{int}} = \left[\psi_0^T \mathbf{M}_0^{N_p} \psi_1\right]$, where $\mathbf{M_0}$ is the transfer matrix that accounts for the incremental contribution to the partition function for growing a polyampholyte chain by a single monomer. This matrix contains the Boltzmann factors for the various possible adsorption states, given the previous adsorption state. We denote an adsorbed salt ion as C, an adsorbed polyampholyte monomer as P and an empty adsorption side as 0. We must also distinguish between the initial monomer of a polyampholyte chain P', and subsequent monomers of that adsorbed polyampholyte chain P. For instance $C0$ denotes a state in which the current monomer has a salt ion adsorbed, and the previous monomer has no adsorbed species. The form of the transfer matrix is as follows:

$$\mathbf{M}_0 = \begin{bmatrix} CC & CP & CP' & C0 \\ PC & PP & PP' & P0 \\ P'C & P'P & P'P' & P'0 \\ 0C & 0P & 0P' & 00 \end{bmatrix} = \begin{bmatrix} A_0\phi_s & A_0\phi_s & A_0\phi_s & A_0\phi_s \\ 0 & F & G & 0 \\ B_0\phi_p & B_0\phi_p & B_0\phi_p & B_0\phi_p \\ D & D & D & D \end{bmatrix} \tag{4.2}$$

The Boltzmann factor for having a salt ion adsorb is written, as in previous work, as $A_0\phi_s$, and similarly the Boltzmann factor for having the initial monomer of polyampholyte chain adsorb is set to $B_0\phi_P$. The prefactors for these Boltzmann factors were previously parameterized to match coarse-grained simulation when A_0 = 20.5 and B_0 = 12.2.[213] We assign an electrostatic energy penalty to charged monomers that are un-paired $\varepsilon(s)$, which is dependent on the monomer index s. This is used in the quantity $D = e^{\varepsilon(s)}$. Finally, the Boltzmann factors for the case of having a subsequent monomer following a newly adsorbed chain and a previously adsorbed chain, G and F respectively, depend on the probability of the current monomer along the adsorbed chain being the counter-ion to the current monomer of the test chain. The vector $\psi_1 = [C, P, P', 0]^T =$

$\left[A_0\phi_s, 0, B_0\phi_{\mathrm{P}}, e^{\varepsilon(0)}\right]^T$ is comprised of the Boltzmann factors for the first monomer along the chain. The vector ψ_0 is a vector of all ones.

In this transfer matrix theory, the charge sequence effects are manifested in the Boltzmann factors D, F and G. For this work, we will consider polyampholytes with zero net charge that are comprised of alternating blocks of opposite charge and equal size. In this case, the charge pattern of the chain can be described by a single value, τ, which represents the length of one repeat unit comprised of one polycation block followed by one polyanion block. The form of the Boltzmann factors F and G depends on whether or not the specified monomer along the chain is at a charge-sign interface, meaning it is followed by a monomer of the opposite charge. For monomers away from the charge-sign interface, $F = (\tau - 4)/(\tau - 2)$ and $G = 2 - 4/\tau$. In the case of F, where two consecutive monomers on an already adsorbed chain are both adsorbed onto the test chain, the probability that they are both counter-ions to the test chain is $(\tau/2 - 2)/(\tau/2 - 1)$. For monomers at the charge-sign interface, $F = (2)/(\tau - 2)$ and $G = 4/\tau$, with the exception in the case of $\tau = 2$ in which $F = 1.0$. In the limit as $\tau \to \infty$, the values for F and G approach their respective values for a homopolyelectrolyte. This leaves the Boltzmann factor D to be determined in order to evaluate the interaction partition function for the polyampholyte chain. The electrostatic energy penalty $\varepsilon(s)$ is determined from coarse grained simulations of a test chain in a dilute salt solution.

4.3.2 Single Polyampholyte Chain Coarse-grained Simulations

It is electrostatically unfavorable for a charged monomer not to be paired with an oppositely-charged salt ion or polyelectrolyte, especially in the limit of high linear charge density. Previous work has shown that the localization of opposite charges along a sequenced polyelectrolyte is profoundly influenced by the sequencing of the charges along the chain,[136,214] which we expect to be especially important in the case of polyampholytes that have a combination

of repulsive and attractive electrostatic interactions due to the presence of both positive and negative charges along the chain.

Previous work on sequence-defined polyelectrolytes have shown that single-chain simulations are a powerful way to inform the transfer matrix model,[136,214] allowing us to correlate the electrostatic energy penalty $\varepsilon(s)$ to monomer-specific salt ion localization. In this work, we consider a single fully extended and fixed, sequenced polyampholyte in a dilute salt solution. We note that this is subtly different from previous efforts that do not extend the polyelectrolyte chain.[214] In this work we do extend the chain to avoid self-collapse of the polyampholyte, and have verified that it does not noticeably alter the values of $\varepsilon(s)$ obtained. Monte Carlo (MC) simulations are performed for single polyampholyte chains in dilute salt solution using the restricted primitive model (Figure 4.2). The solvent, water, is modeled as a continuum with a relative dielectric constant ε_r = 78.5. Salt ions and polyampholyte monomers are modeled as charged hard spheres with a diameter σ = 4.25 Å. The total potential U is the sum of the electrostatic potential U_{ES}, and the hard-sphere potential U_{HS}.

$$U = U_{\mathrm{ES}} + U_{\mathrm{HS}} \tag{4.3}$$

The electrostatic potential is set to a Coulomb potential:

$$U_{\mathrm{ES}} = \sum_i \sum_{j>i} \frac{q_i q_j e^2}{4\pi\varepsilon_0 \varepsilon_{\mathrm{r}} r_{ij}} \tag{4.4}$$

where q_i is the valency of the bead i, e is the electron charge, ε_0 is the vacuum permittivity, and r_{ij} is the distance between beads i and j. The electrostatic interactions are evaluated using Ewald summation. The excluded volume of the ions and monomers are captured using a hard-sphere potential:

$$U_{\mathrm{HS}} = \sum_i \sum_{j>i} \begin{Bmatrix} \infty\, r_{ij} < \sigma \\ 0\, r_{ij} \geq \sigma \end{Bmatrix} \tag{4.5}$$

Each MC simulation is run for 10×10^6 MC timesteps. The number charge densities are evaluated after an equilibration period of 1×10^6 MC timesteps by counting the number of salt ions within a cutoff separation, $r_c = 1.5\sigma$, for each monomer. These simulations were performed at salt concentration of $\phi_s = 1.32 \times 10^{-4}$.

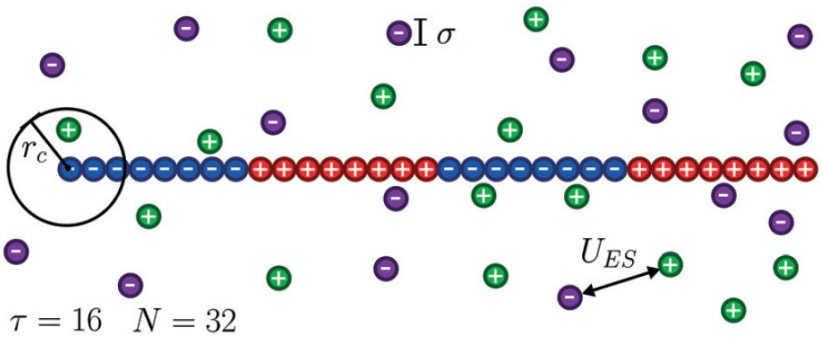

Figure 4.2. Schematic illustrating the restricted primitive model Monte Carlo (MC) simulation of single polyampholyte chain. The chain is stretched and fixed, with the charges distributed according to the 'blockiness' parameter τ. The salt ions are free to translate in the simulation box according to the potential U, which comprised of a Coulombic electrostatic potential U_{ES} and a hard sphere potential U_{HS} to account for the excluded volume of the various particles. The particle diameter is given by σ and the bond length is 1.05σ.

Salt ion localization for a given monomer in the sequence is quantified from MC simulations by evaluating the ratio of the local number charge density, $n_c(s)$, and the local number charge density in the case where electrostatic interactions are turned off, n_c^0(s). We can approximate $n_c(s)$ and n_c^0(s) using a simple, uncorrelated adsorption model, which gives the following expression:

$$n_c(s) \sim e^{-(\varepsilon'(s)-\mu)} \Big/ \left(1 + e^{-(\varepsilon'(s)-\mu)}\right)$$
$$n_c^0(s) \sim e^{\mu} \Big/ \left(1 + e^{\mu}\right) \tag{4.6}$$

In the dilute salt limit, such that $e^{\mu} \ll 1$, we can define an electrostatic association strength as, $\varepsilon'(s) = \ln[n_c(s)/n_c^0(s)]$. It has been previously shown that this quantity is independent of the simulation salt concentration ϕ_s in the appropriate limit.[214] For a given polyampholyte sequence,

we set a reference state as the average electrostatic association strength of a homopolyelectrolyte with the same degree of polymerization as the polyampholyte. Finally we set the electrostatic energy penalty in the Boltzmann factor D to be equal to the deviation of the electrostatic association energy of the polyampholyte from the reference state.

$$\varepsilon(s) = \left\langle \ln\left(\frac{n_{\mathrm{c,hp}}(s)}{n^{0}_{\mathrm{c,hp}}(s)} \right) \right\rangle - \ln\left(\frac{n_{\mathrm{c}}(s)}{n^{0}_{\mathrm{c}}(s)} \right) \tag{4.7}$$

To carry out this calculation for a polyampholyte, where the sequence is defined by the charge block size $\tau/2$ and the number of charge-blocks, three MC simulations are performed. The first simulation is for the sequenced polyampholyte chain, the second is for the homopolyelectrolyte with the same degree of polymerization as the polyampholyte, and the third is for a neutral chain with the same degree of polymerization as a single charged block. All simulations were repeated 10 times, and the average $\varepsilon(s)$ was calculated.

4.3.3 Polyampholyte and Polypeptide Synthesis

A series of lysine–glutamate polyampholytes with increasing blockiness (*i.e.*, $(K_8E_8)_3$, $(K_{12}E_{12})_2$, $(K_{15}E_{15})_2$, and $K_{24}E_{24}$), along with homopolypeptides corresponding to the individual blocks (*i.e.*, K_{12}, E_{12}, K_{15}, E_{15}). Both polyampholytes and homopolypeptides were prepared using standard Fmoc-based solid-phase synthesis105 on a Liberty Blue automated microwave peptide synthesizer from CEM, Ltd. using methods reported previously.[214136] Briefly, synthesis of polyampholytes and homopolypeptides was performed on low loading Rink amide Protide resin (0.19 mmol/g, CEM) and Rink amide MBHA resin (0.32 mmol/g, Peptide Solutions), respectively, using Fmoc-L-LysIJBoc)-OH, Fmoc-D-LysIJBoc)-OH, Fmoc-LGluIJtBu)-OH and Fmoc-D-GluIJtBu)-OH (Peptide Solutions, LLC). 20% piperidine (Sigma Aldrich) in N,N-dimethylformamide (DMF, sequencing grade, Fisher BioReagents) was used for Fmoc deprotection, while 0.5 M N,N-diisopropylcarbodiimide (DIC, 99% Acros Organics) and 0.5 M

ethyl (hydroxyimino)cyanoacetate (Oxyma, Peptide Solutions) in DMF were used as activator and base, respectively. Double coupling was applied to all lysine monomers in polyampholytes to increase peptide yield. Cleavage from the resin and side-chain deprotection was performed in 95/2.5/2.5% (v/v) trifluoroacetic acid (TFA, Fisher)/water (MilliQ 18.2 MΩ cm, Millipore)/triisopropylsilane (98% Acros Organics) for 3 hours at room temperature. The resulting peptides were precipitated into cold anhydrous ethyl ether (BHT stabilized, Fisher Scientific). The final product was characterized by matrixassisted laser desorption/ionization time of flight mass spectrometer (MALDI-TOF, Bruker UltrafleXtreme).

All peptides were synthesized using amino acids of alternating chirality (D and L) to mitigate inter-peptide hydrogen bond formation.[23,91,92] Lysine groups are neutralized by a TFA counter-ion. Glutamate groups are neutralized by sodium.

4.3.4 Preparation of Stock Solutions

Polyampholyte and homopolypeptide stock solutions were prepared gravimetrically using MilliQ water at a concentration based on the total number of amino acids present and adjusted to pH = 7.0 ± 0.03 using concentrated solutions of HCl and NaOH (Fisher Scientific), as needed. For instance, a stock solution of the homopolyanion poly(glutamate) of 10 mM amino acid would be used in parallel with a stock solution of an oppositely-charged poly(lysine), also at 10 mM with respect to the total number of amino acids. For polyampholytes, a stock solution of poly(lysine-co-glutamate) of 10 mM amino acid would consist of 5 mM lysine and 5 mM glutamate, respectively. Sodium chloride (NaCl) was purchased from Sigma Aldrich (ACS reagent). A stock solution was prepared gravimetrically at 4 M and adjusted to pH = 7.0, as above.

4.3.5 Coacervate Preparation and Characterization

Complexation was performed using stoichiometric quantities of positively and negatively charged polypeptides at a total charged residue concentration of 1 mM, 10 mM, 20 mM, 40 mM

and 50 mM at pH 7.0. Under these conditions, it is a reasonable approximation to describe all of the residues on both polyampholytes and polypeptides as fully charged. Homopolypeptide coacervate samples were prepared by first mixing a concentrated solution of NaCl with MilliQ water in a microcentrifuge tube (1.5 mL, Eppendorf), followed by the polyanion. The resulting mixture was then vortexed for 5 s before addition of the polycation. The final mixture was vortexed for at least 15 s immediately after the addition of polycation to ensure fast mixing. For polyampholyte samples, the peptide was added directly into the water–NaCl mixture, followed by vortexing as described above. Notably, the low levels of salt allowed for phase separation in our polyampholyte stock solutions. Therefore, it was critically important to ensure that the stock solution was well mixed prior to pipetting. Phase separation could be observed via an increase in the turbidity, and/or the opalescent appearance of the samples, due to the formation of small droplets of the complex coacervate phase.

4.3.5.1 Determination of Salt Resistance

Samples were then examined using brightfield optical microscopy (EVOS XL Core, Fisher Scientific) to confirm the liquid nature of the droplets, and to determine the 'salt resistance,' ϕ_P^s, or the salt concentration above which no phase separation occurs. All samples were imaged within 1 h of preparation. Error bars on measurements of the salt resistance correspond to the salt concentration intervals over which samples were prepared.

4.3.5.2 Fourier Transform Infrared (FTIR) Spectroscopy

Attenuated total reflectance Fourier transform infrared spectrometry (ATR-FTIR, Platinum ATR, Bruker Alpha, Billerica, MA) was used to analyze the secondary structure of complexes resulting from polyampholytes and homopolypeptides. The amide I carbonyl stretching vibration were measured by FTIR (1600–1700 cm^{-1}) to detect the formation of secondary structure of peptide-based complexes. All samples were prepared at a total charged residue concentration 65

mM at pH = 7.0. Lyophilized (Labconco, FreeZone Plus 2.5 Liter Cascade Console Freeze-Dry System, Kansas City, MO) complex samples then were examined by FTIR, and the resulting spectra were normalized at 1650 cm^{-1} to facilitate comparison.

4.4 Results and Discussion

Using the transfer matrix model, we evaluate the propensity for various sequences of model polyampholytes and their analogous homopolyelectrolytes to undergo self-coacervation or complex coacervation, respectively. The transfer matrix model is informed by Monte Carlo simulations that evaluate the sequence dependent electrostatic association strength for each monomer along the chain. The system free energy described in Eq. 4.1 is minimized to resolve the two-phase coexistence boundaries and compositions as a function of 'blockiness' as well as the number of charged blocks; these results are compared to experimentally-determined salt resistances for sequenced polyampholytic polypeptides and homopolypeptides.

4.4.1 Salt Ion Localization from MC Simulations

In our transfer matrix theory, electrostatic sequence effects are described by the electrostatic energy parameter $\varepsilon(s)$, as determined from single chain MC simulations. Therefore, we study the trends in this parameter as a function of sequence 'blockiness' τ. The polyampholyte sequences are characterized by the 'blockiness' τ as well as the number of charged blocks in the chain. In Figure 4.3, we show how the charge sequence affects salt ion localization around the chain by plotting $\varepsilon(s)$ for a polyampholyte chain with a degree of polymerization N_p = 48, and a homopolyelectrolyte with the same degree of polymerization. The homopolyelectrolyte exhibits a near-constant value of $\varepsilon(s) \approx 0$ along the center of the chain, which reflects the normalization condition in Eq. 4.7. Deviations only occur at the chain ends, suggesting that except for the 2–4 monomers at the chain end, the electrostatic environment around most homopolyelectrolyte monomers is similar to that of an infinite line of charge. This reflects a significant localization of

the oppositely-charged salt ions near the polyelectrolyte chain. At the chain ends, there is a marked increase in $\varepsilon(s)$ that reflects the transition from appearing as an 'infinite' line of charge to a 'semi-infinite' line of charge. Here, the last monomer of the chain does not get the 'advantage' of like-charged monomers connected on both sides, in terms of localizing the opposite charge, therefore it is less likely to have salt ions condensed near the chain-ends.

Analysis of our polyampholyte systems demonstrates that the pattern of positive and negative charges strongly affects charge confinement. This is apparent as the blockiness τ of the charge patterns increases from alternating positive–negative monomers (τ = 2) to blocks of 24 positive and negative monomers (τ = 48), seen in Figure 4.3. Here, the key difference is the presence of charge-patterning interfaces where the sign of the sequence changes from positive to negative (Figure 4.4). For τ = 2, this occurs every monomer. Correspondingly, the value of the electrostatic energy parameter ε(s) ≈ 6 reflects the weak localization of salt charges near to the polyampholyte, meaning that the opposite charges of the residue can effectively neutralize each other without the need for additional salt ions. Due to this close proximity of positive and negative charges, we observed an increase in salt ion localization (*i.e.*, lower values of ε(s)) at the chain ends where there are fewer nearby, opposite charges. Modest increases in the blockiness do not lead to large changes in the electrostatic environment, shown by τ = 4.

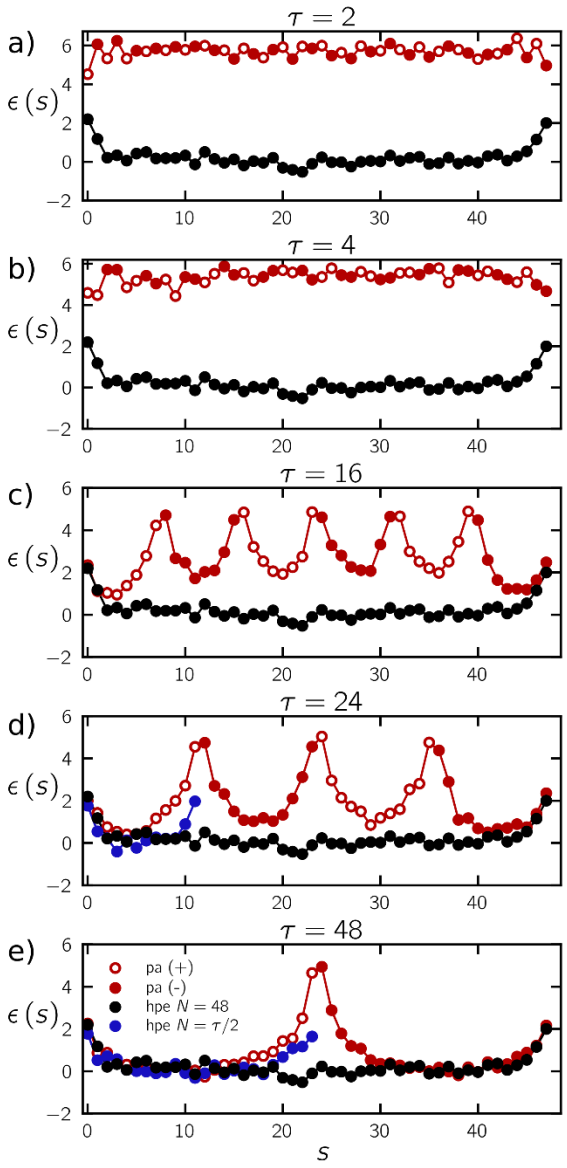

Figure 4.3. Monomer-dependent energy $\varepsilon(s)$ as a function of chain index, calculated from Eq. 4.7 using MC simulations for polyampholytes (pa, red) of increasing 'blockiness' τ. Open points are for the cation (+) beads and the filled points are for the anion (−) beads. These data are compared with a full-length homopolyelectrolyte (hpe, black) where $N_p = 48$. For $\tau = 24$ and $\tau = 48$, results are also shown for homopolyelectrolytes where $N_p = \tau/2$ (blue).

As blockiness increases significantly, for example to $\tau = 16$, salt ions become increasingly localized by the long runs of positive and negative monomers. The charge-patterning interface, located every 8 monomers, is quantitatively similar in $\varepsilon(s)$ to the $\tau = 2$ case and does not significantly localize salt ions near the polyampholyte chain. Nevertheless, as these charge-

patterning interfaces become less frequent along the polyampholyte sequence, the regions in between become closer to the homopolyelectrolyte limit of $\varepsilon(s) \rightarrow 0$. This is observed as τ is increased from 24 to 48.

We further demonstrate the significance of these charge patterning interfaces by comparing the values of $\varepsilon(s)$ for a polyampholyte with large τ to those for homopolymers with the same degree of polymerization as the component blocks (*i.e.*, $N_p = \tau/2$) in Figure 4.3a,e. The homopolymer values for ε are shown as blue dots. Deviations between the values of ε are most significant when comparing the chain ends of the homopolyelectrolyte and the location of the charge patterning interface ($s = 10, 11$ for $\tau = 24$ and $s = 22, 23$ for $\tau = 48$). Here, salt ion localization is significantly stronger for chain-ends than for the charge-patterning interface, which we attribute to the presence of the nearby oppositely-charged monomers (Figure 4.4).

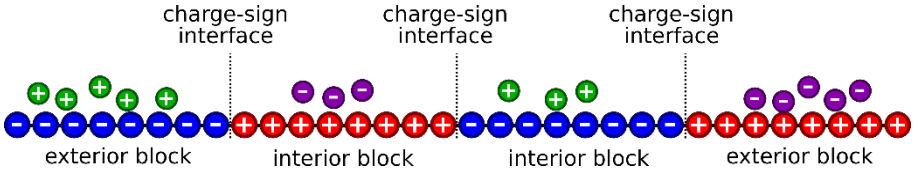

Figure 4.4. Schematic of salt localization along polyampholyte chains with $\tau = 16$. The key features are the chain ends and the charge-sign interfaces. Both chain ends and charge-sign interfaces reduce salt localization however the charge-sign interfaces sees even more reduction in salt localization.

4.4.2 Phase Behavior Predicted by Transfer Matrix Theory Model

The electrostatic energy parameters $\varepsilon(s)$ determined from the MC simulations are used to evaluate the polyampholyte chain partition function and subsequently the system free energy Eq. 4.1. We plot the resulting phase diagrams in Figure 4.5 for the sequenced tetra-block polyampholytes, as well as their analogous homopolyelectrolyte where $N_p = \tau/2$. In these phase diagrams, the binodal curves demarcate a region of salt–polymer concentrations (ϕ_s versus ϕ_p) within which phase separation occurs. Two 'branches' of the binodal at high and low polymer concentrations ϕ_p are connected by tie-lines denoting the two values of ϕ_p and ϕ_s that are in

coexistence. Similar to prior results for both simulation and experiments on homopolyelectrolyte coacervates,[72,213] these tie-lines exhibit negative slopes indicating that the polymer-dense coacervate phase (high ϕ_p) has a lower salt concentration than the polymer-dilute supernatant phase (low ϕ_s). For this transfer matrix model for coacervation, this salt partitioning to the supernatant phase has been attributed to the high excluded volume in the coacervate phase.[72–74,110,213] This is consistent with other theoretical results,[101,110,138,147] and is supported by experiment and simulations.[72,142,151,217,218] The negative slope of the tie line distinguishes this model from theories accurate in the low-charge density limit, which exhibit tie lines with negligible or positive slopes.[68,103,204,205] Here, salt partitioning is driven by the increased electrostatic attractions in the charge dense (*i.e.,* polymer dense) phase.[5,68,103,107,204,205]

Figure 4.5 highlights the difference between polyampholyte and homopolyelectrolyte coacervation, with comparable values of τ and N_p such that the main molecular difference is that the homopolyelectrolytes can be 'connected' to yield the blocky polyampholytes. A few key trends are apparent in this set of phase diagrams. We observe an increase in the size of the two-phase region that is consistent with the increased salt ion localization along the stretched polyampholytes in Figure 4.3 as a function of increasing τ, and thus an increase in the entropic driving force. This also correlates with the decrease in regions along the polyelectrolyte chain affected by the charge-pattern interfaces, where the switch from positive to negative charges in the monomer sequence prevents charge localization and thus weakens the electrostatic driving force for coacervation. This sequence effect persists even for block sizes as large as τ = 48, which we attribute to the effect that a single charge-patterning interface has on values of $\varepsilon(s)$ as far as 10 monomers away along the chain contour. A similar trend is observable in the homopolyelectrolytes, where an increase in chain length corresponds to an increase in the two-phase region. Here, there are no charge-pattern interfaces, and instead the weaker salt localization at the chain ends plays a similar role in weakening phase separation at lower values of N_p that have a higher fraction of chain ends.

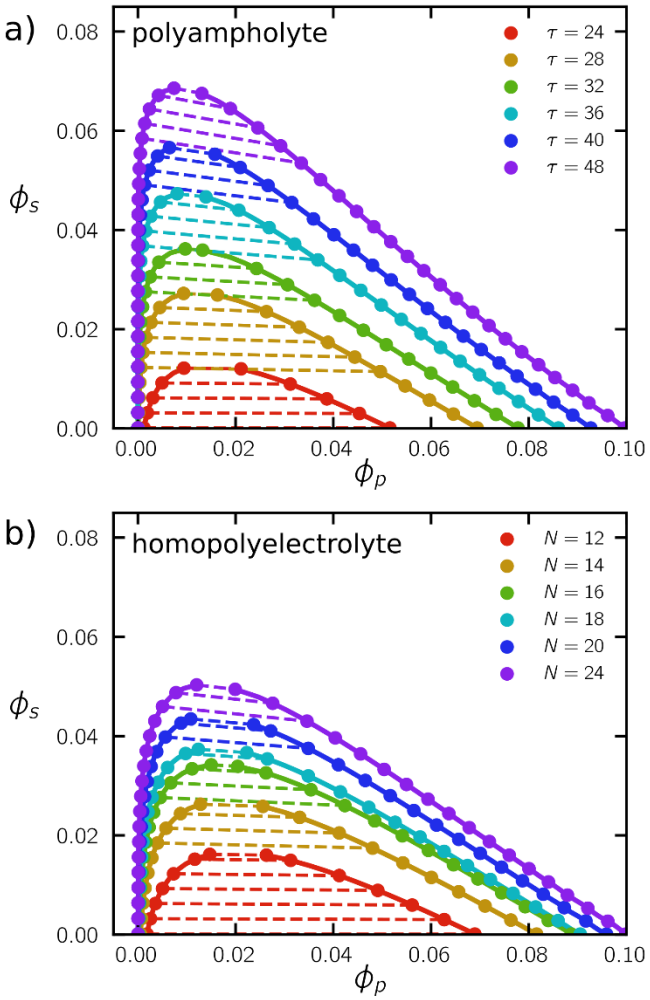

Figure 4.5. Plots showing the phase diagrams for polyampholytes **(a)**, and their analogous homopolyelectrolytes **(b)** for varying values for τ . The homopolyelectrolyte degree of polymerization is set to be $N_p = \tau/2$. The dotted lines represent the tie lines for the two phases. The tie lines are shown for each curve where the lower τ value tie lines are shown when the coexistence regions of overlaps with the coexistence region of another τ curve.

In addition to the presence of charge-pattern interfaces or chain ends, both polyampholyte and homopolyelectrolyte coacervation are expected to be affected by differences in the translational entropy of the polymeric species. Larger N_p and larger τ represent larger chains, and thus there is an increase in the number of polyelectrolyte charged interactions per chains. This chain-length effect has long been understood to play a role in homopolyelectrolyte coacervation,[219] and we expect it to complement charge-sequence effects here.

Figure 4.6 provides a summary of the simulation results, plotted as the critical salt concentration ϕ_s^{cr} as a function of the blockiness τ (for polyampholytes) and $2\,N_p$ (for homopolyelectrolytes). The value ϕ_s^{cr} is simply the maximum salt concentration ϕ_s where phase separation can be observed. This allows for the direct comparison of the phase diagrams in Figure 4.5, which exhibit an increase in the two-phase region with both increasing τ or N_p. We show that, at large values of $\tau > 32$, the strength of phase separation increases with increasing chain length; the homopolyelectrolyte for $N_p = 24$, for example, corresponds to a di-block polyampholyte of $\tau = 48$, which has a chain length of $N_p = 48$. Extending this polymer to consider a tetra-block polyampholyte with a chain length of $N_p = 96$, we observe a commensurate increase of ϕ_s^{cr} that we attribute primarily to the increase in charges per single-chain translational degree of freedom.

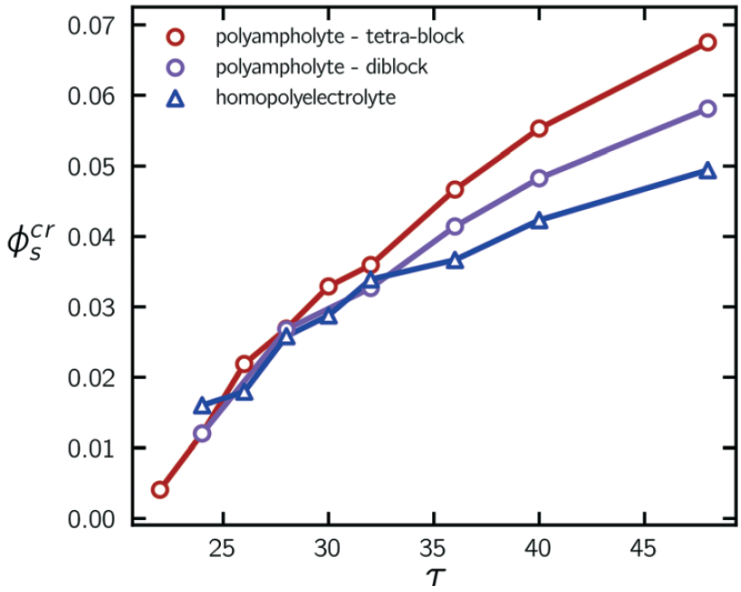

Figure 4.6. Plots of the critical salt concentrations (ϕ_s^{cr}) for the tetra-block polyampholyte (red), the di-block polyampholyte (magenta), and their analogous homopolyelectrolyte (blue) as a function of τ. For the homopolyelectrolyte, $\tau = 2N$. The dashed lines are to guide the eye.

In contrast, at low values of $\tau \leq 32$, we observe similar values of ϕ_s^{cr} for the three different types of coacervates. We attribute this to a tradeoff between the number of charges per chain, and the differences between the strength of charge localization at chain ends versus charge-pattern

interfaces. These effects cancel out, because as the number of charges per chain increases (homopolyelectrolyte to di-block polyampholyte to tetra-block polyampholyte), the chain ends are also replaced by charge-pattern interfaces that are weaker at localizing charges.

To demonstrate how this cancellation of sequence effects occurs, we show in Figure 4.7 a series of di-block versus tetra-block polyampholytes as the value of τ is increased. We note that this shows the transition out of the cancellation regime and into the regime where the two polyampholyte types significantly deviate. We highlight two trends; with increasing τ, the higher values of N_p (the tetra-blocks) are more sharply peaked near the critical point, reflecting the approach of the critical point to smaller values of ϕ_p at larger values of N_p. However, there is a second trend of the value of ϕ_p at ϕ_s = 0, where the tetra-block binodal is initially at lower values of ϕ_p than the di-block, however this inverts at larger values of τ.This inversion occurs because, in traditional polymer–solvent phase diagrams, the binodal moves to larger values of ϕ_p for larger values of N_p. This is the case at large τ. However, at lower values of τ the phase separation is weaker for the tetra-block due to the presence of more charge-pattern interfaces.

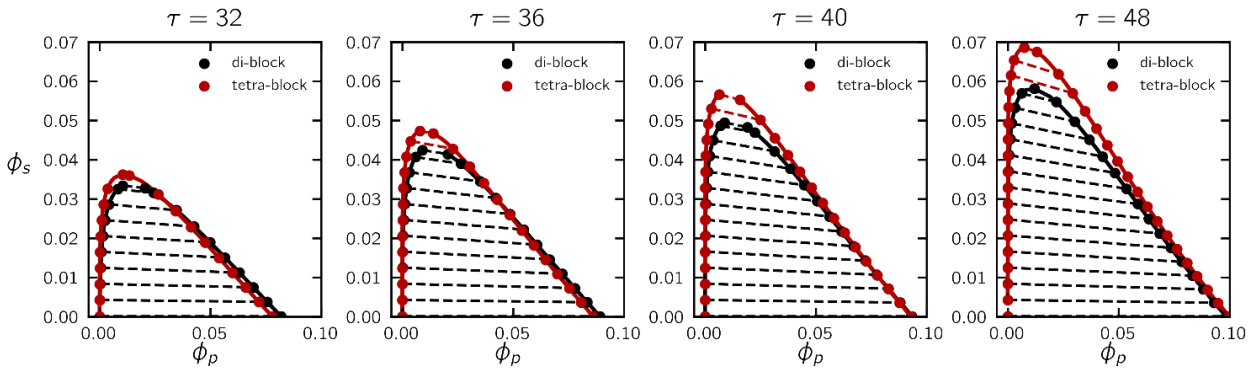

Figure 4.7. Plots comparing the phase diagrams for di-block polyampholytes (black) and tetra-block polyampholytes (red) for varying values of τ.

4.4.3 Comparison of Experimental, Theoretical Observations in Polyampholyte Self-coacervation

The trends predicted by our transfer matrix theory show good qualitative agreement with experimental observations. In particular, we compare how the salt resistance ϕ_s changes as a

function of polymer concentration ϕ_p , for polyampholytes and their analogous homopolyelectrolyte coacervates. Both theory (Figure 4.8a) and experiment (Figure 4.8b) exhibit a significant decrease in salt resistance as the polymer concentration decreases. The trends in salt resistance also increase with increasing block size τ or chain length N. Additionally, the salt resistance is higher for the di-block polyampholytes than for the analogous 'split' component homopolyelectrolytes.

In these comparisons, we note that the theoretical results included a value of the χ_{pw} parameter ($\chi_{pw} = 0.25$) to account for short-range interactions, parameterized to compare well with experimental data; nevertheless, the trends are consistent regardless of this choice. We note that we generally do not expect quantitative matching, as this theory invokes a mean-field approximation in the transfer matrix calculation that is not accurate at low ϕ_p. Furthermore, the coarsegrained representation we use does not resolve physical phenomena at the atomistic level, such as dielectric or polarization effects[220–224] that prevent us from making quantitative predictions. Regardless, we observe qualitatively similar trends in both theory and experiment, showing that this theoretical model captures key physical behaviors in blocky polyampholyte self-coacervation.

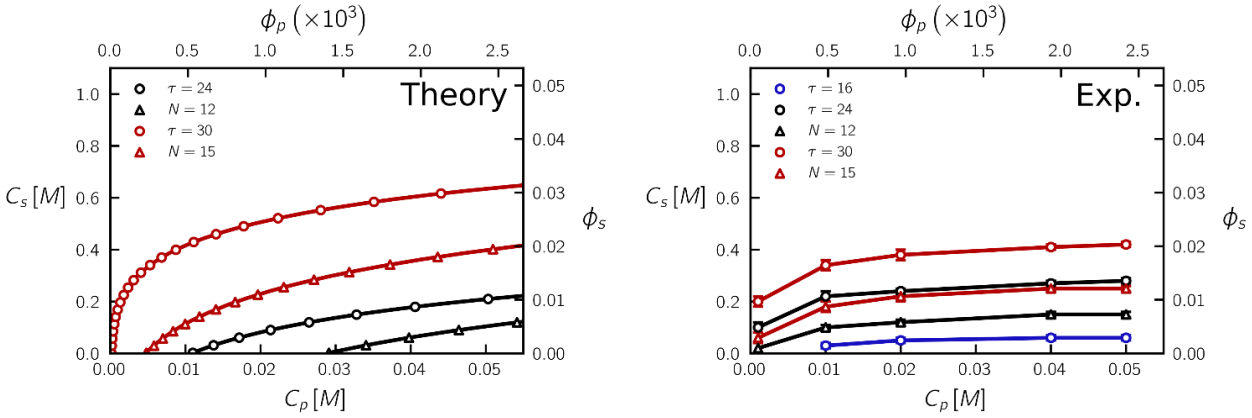

Figure 4.8. Plots of the dilute branch of the binodal as a function of ϕ_s versus ϕ_p for theory **(a)** and experiment **(b)**, for di-block polyampholytes with τ = 16, 24, 30 (circles) and the corresponding N_p = 12, 15 homopolyelectrolyte coacervates (triangles). The transfer matrix theory reproduces trends observed in experiment; namely, the two-phase region increases with increasing block length (N, τ) and is higher for block polyampholytes *versus* homopolyelectrolytes.

We extend our comparison of experiment and theory to consider how blockiness τ leads to changes in self-coacervation. We plot the salt resistance ϕ_s^r as a function of the blockiness τ for both theory (Figure 4.9a) and experiment (Figure 4.9b). These data further highlight the general trend of increasing salt resistance with increasing blockiness above some τ below which no phase separation is observed. For our theoretical model, this value is roughly around $\tau = 20$, while for experiments this value is around $\tau = 15$.

We show that the relative position of the homopolyelectrolyte *versus* polyampholyte salt resistance depends on the particular measurement. As mentioned previously, the critical salt concentration ϕ_s^{cr} exhibits a crossover at low τ related to the interplay between translational entropy and sequence- effects. However, experiments measure the related value of salt resistance ϕ_s^r that is calculated at a defined ϕ_p; in Figure 4.9a we plot both ϕ_s^{cr} and ϕ_s^r, with the latter for a number of values of ϕ_p. Indeed, the crossover observed for the critical point disappears and the trend of lower salt resistance for homopolyelectrolytes compared with polyampholytes emerges at the lower values of ϕ_p that correspond with experiments.

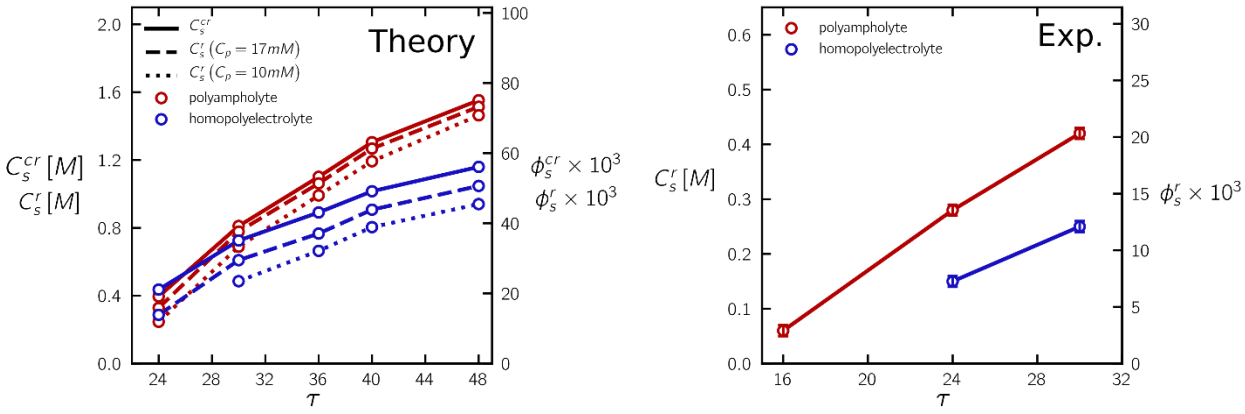

Figure 4.9. Critical salt concentration ϕ_s^{cr} and salt resistance ϕ_s^r as a function of τ in theory **(a)** and experiment **(b)** for $\chi = 0.25$. In **(a)**, we demonstrate that different measures of coacervate phase behavior result in subtly different behaviors for the block polyampholyte (pa) versus the homopolyelectrolyte (hpe) coacervates; the critical salt concentration ϕ_s^{cr} exhibits a crossover at $\tau \approx 24$, while the salt resistance ϕ_s^r shows larger differences between the two cases as the concentration ϕ_p at which they are measured is decreased. This is consistent with the experimental results in **(b)**, which show a distinctly lower value of ϕ_s^r for the homopolyelectrolyte than the block polyampholyte coacervates.

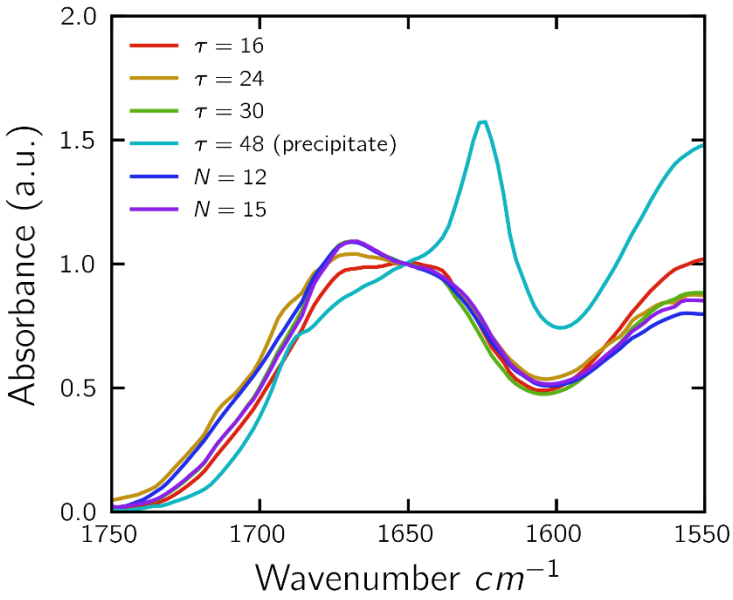

Figure 4.10. FTIR of polyampholyte/homopolypeptide complexes. FTIR spectra showing the amide I region for the liquid complex coacervates and solid precipitates. All complexes showed a peak at 1564 cm^{-1} and 1673 cm^{-1}, corresponding to the carbonyl stretch of the glutamic acid and TFA counter-ion,125 respectively. A peak at 1644 cm^{-1}, characteristic of random coil structure, was observed amongst the samples that underwent liquid–liquid phase separation. However, peaks at 1623 cm^{-1} and 1680 cm^{-1} that are characteristic of β-sheets were observed for the solid complexes formed by the τ = 48 polyampholyte.The signal was normalized at 1650 cm^{-1}.

Lastly, our experimental efforts revealed a surprising result. The polypeptides used in our experiments were synthesized using amino acids of alternating chirality to mitigate inter-peptide hydrogen bond formation and subsequent β-sheet formation.[23,91,92] While we observed liquid–liquid phase separation for most of our samples, precipitation and β-sheet formation occurred for polyampholytes with τ = 48 (Figure 4.10). Evidence for β-sheet formation can be seen through FTIR analysis (Figure 4.10), where only the τ = 48 sample showed a peak at 1623 cm^{-1}, as well as an additional low-intensity peak present near 1680 cm^{-1}, which are both indicative of β-sheet formation.[91,225–227]

This unexpected β-sheet formation is similar to recent reports by Tabandeh and Leon, however it is unclear whether the mechanism is the same.[228] The work by Tabandeh and Leon looked at complexation between patterned polypeptides with different levels of hydrophobicity and

attributed β-sheet formation to decreased steric clashing between D and L monomers because of the shorter side-chain length of the hydrophobic residues. However, the polymers in our system consist solely of lysine and glutamate, and show no evidence of precipitation when present as equivalent length homopolyelectrolytes. This result requires additional investigation that is beyond the scope of the current work.

4.5 Conclusions

We have developed a simulation-informed theoretical model for the phase behavior of polyampholytes that undergo self-coacervation, specifically in the limit where the charge density is sufficiently high that salt ion localization is a significant driver of coacervate formation. We show that the sequence, or pattern, of charges along these polyampholytes plays a large role in their ability to undergo coacervation. As the chains become more blocky, charge localization – and correspondingly the strength of coacervation – increases significantly. This increase in coacervation is similar to the effect of increasing the length of chains in homopolymer coacervation, however we show that there is a tradeoff associated with the increase in number of charges per chain for equivalent polyampholyte chains and the increase in the number of charge-pattern interfaces. These charge-pattern interfaces weaken charge localization near polyampholyte chains, and thus weaken the electrostatic driving force for coacervation.

Our predicted trends are also qualitatively consistent with experimental results, including the increase in salt resistance for polyampholytes compared to corresponding homopolyelectrolytes, and an increase in the salt resistance with increasing charge blockiness. We also show that there are subtleties in how this comparison is made. In particular, the polymer concentration at which salt resistance is measured can lead to differences between the polyampholytes and equivalent homopolyelectrolytes as the competition between translational entropy and charge-pattern interface effects affects the critical point and location of the binodal.

We note that this theoretical framework uses a number of assumptions that limit the approach; most importantly, the transfer matrix theory invokes a mean-field approximation for the charges that adsorb to the test polyampholyte. This is similar to approximations made in classical polymer mean-field theories in that the polymer interactions characterizing the dilute branch of the binodal will not reflect the highly correlated intra-chain interactions that are known to characterize molecular structure in the dilute supernatant phase. We also expect inaccuracies in the phase diagram at the critical point, due to the mean-field nature of the underlying polymer field theory. This assumption would only lead to quantitative deviations that would not affect qualitative trends, and could be relaxed by using more sophisticated polymer field theories or by coupling the transfer matrix formalism with spatial correlations.

We have, for this chapter, focused primarily on regular polyampholyte sequences and compared with experiments using model polypeptides. This sets the foundation to consider more complicated sequences and copolymers/copolypeptides. We expect this framework to thus have implications for biologically-relevant macromolecules, such as intrinsicallydisordered proteins (IDPs), which are known to undergo liquid–liquid phase separation in ways that are affected by charge monomer sequence.[9,29,40,171,188]

CHAPTER 5

THE EFFECT OF SALT IDENTITY ON COMPLEX COACERVATION

5.1 Abstract

Complex coacervation is a phase separation phenomenon where the driving force comes mainly from the entropic gains associated with the release of bound counterions upon complex formation between oppositely charged polymers. As a result, complex coacervation is sensitive to the concentration of salt present in solution, as an excess of these ions can disfavor the entropic release of counterions, preventing phase separation. While the work presented to date has addressed the effect of an individual salt on the phase behavior of sequence-defined complex coacervates, in this Chapter we address the question of salt identity. We examine how a series of alkali halide salts affect the phase behavior of a model polypeptide coacervate system, and compare these results with data from isothermal titration calorimetry measurements to probe potential differences in the thermodynamic driving force for coacervation. While we did not observe significant variation in the salt resistance of our complex coacervates as a function of salt identity, we did observe significant differences in their thermodynamic parameters. Trends in the entropic driving force for coacervation corresponded with the ordering of ions in the Hofmeister series. We hypothesis that this Hofmeister-like behavior is due to a combination of factors that include ion size, preferential interactions between ions of similar hydration level, and how water restructures during the release of counterions.

5.2 Introduction

An increasing number of reports have described the entropic nature of the driving force for complex coacervation. Typically, this favorable entropy is generally attributed to the release of bound counterions and the restructuring of water,[136,229,230] although there has been very little work looking into the ways in which ion identity and hydration affect coacervation. Here, our goal is to explore the ways in which ion identity can affect the phase behavior and thermodynamic driving forces associated with complex coacervation. This study will help to elucidate the fundamental role of salt in coacervate formation, and is critical for designing complex coacervate-based materials for applications in various environment conditions. As an example, the stability requirements for a material to be used in seawater (*i.e.*, ~700 mM NaCl and pH ~7.4–8.4) are significantly different from the requirements for stability under physiological conditions (*i.e.*, ~150 mM KCl and pH ~7.4 in the cytosol) because of both the differences in the ionic strength and the identity of the ions involved.[26,231–235] To this end, we need to have a systematic understanding of salt effects to develop an comprehensive design principle for complex coacervates.

The effect of salt on complex coacervation can be divided into two categories, (i) the effect of the "ionic strength" of the solution, and (ii) the effect of "salt identity." The effect of ionic strength has been typically characterized in terms of a salt resistance, or the concentration of salt above which phase separation is no longer observed for a given polymer concentration. Salt resistance has been used as a simple parameter to characterize the phase behavior of complex coacervates as a function of the salt concentration/ionic strength without requiring the complete mapping of a phase diagram.[20,136]

While work by Perry *et al*., demonstrated that large scale differences between ions of different charge could be accounted for in terms of ionic strength, more subtle differences between the various salt ions at an equivalent ionic strength can be explained in terms of the Hofmeister series.[2,54,236] The trends associated with the Hofmeister series were originally established from experiments concerning the precipitation of egg white proteins in the presence of different salts.

The typical Hofmeister series for anionic salts describes a continuum of behavior where salts with the strongest ability to "salt-in," or increase the solubility of proteins, termed "chaotropes," correlates with weak hydration, while strongly hydrated anions, termed "kosmotropes," results in the "salting out," or decreased solubility of proteins (Figure 5.1). In general, the Hofmeister effect for anions dominates over that of cations due to differences in ion-water interactions. For instance, an anion would have stronger interactions with water than a cation of the same size and absolute charge density.[237] However, it is noteworthy that the "salting out" effects of cations are opposite to that of anions, meaning that while a strongly hydrated anion is considered kosmotropic, a weakly hydrated cation would show similar behavior. This apparent reversal in Hofmeister-like behavior (Figure 5.1), might be caused by the different charged groups being present on the accessible surface of biological molecules such as proteins.[238]

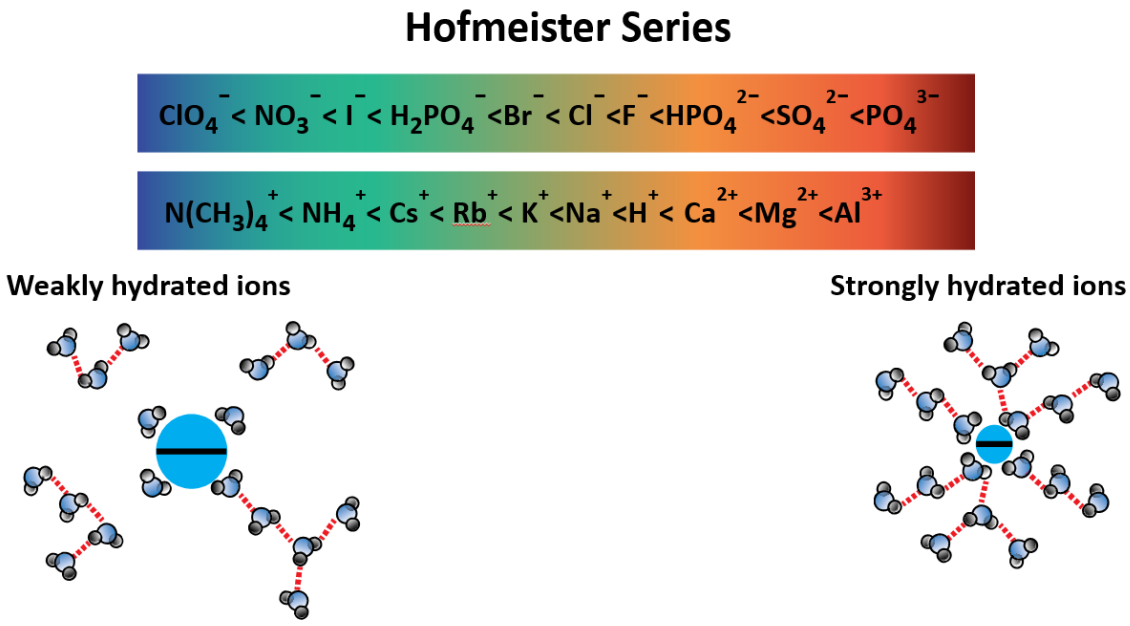

Figure 5.1. Typical ordering of anionic and cationic salts in the Hofmesister series.[236,238–241] The salt ions become more hydrated moving from left to right. Weakly hydrated anions and strongly hydrated cations are considered chaotropes, while strongly hydrated anions and weakly hydrated cations are considered kosmotropes.

It is worth noting that the trends associated with the Hofmeister series are complicated and can be attributed to a combination of factors including ion size, ion hydration, dispersion effects, polarizability and specific binding.[20] However, the underlying principles of Hofmeister series remain unclear. In some reports, the position of ions within the series can change depending on the specific details of the system that was examined or the method was selected to determine the property.[238,242]

Although there have been a number of reports addressing the effect of salt identity on polyelectrolyte complexation, they have mostly focused on solid polyelectrolyte complexes (PEC) and polyelectrolyte multilayers, rather than liquid complex coacervates.[242–244] Schlenoff *et al.* found that the thermodynamic doping constant for sodium salts with different anions in an extruded saloplastic polyelectrolyte complex followed the Hofmeister series. Furthermore, Schlenoff *et al.* noted that the diffusion coefficient for PEC with different doped sodium salts show a reversed effect at the same doping level, which was attributed to the ability of more hydrated anions (kosmotropes) to bring more water into the PEC, thus creating a larger free volume for ion motion, as well as a more plasticized PEC.[243]

The effect of salt identity on sequential layer-by-layer (LBL) assembly has been studied even earlier than for solid PECs. Salomäki *et al*.[242] observed that the thickness of dry polyelectrolyte multilayers made from poly(styrene sulfonate), PSS, and poly(diallyldimethylammonium chloride), PDADMAC, strongly correlated to the Jones-Dole viscosity B coefficient and hydration entropy of anions used in the layer-deposition process, and followed the Hofmeister series for anions. The weakly hydrated anions (chaotropes) were able to screen the polyelectrolyte charges to a greater extent than more strongly hydrated anions (kosmotropes). This effect also induced the more compact deposition of polyelectrolytes onto a surface, yielding a denser and layer.[242] The same strategy was also used to optimize the thickness and stimuli-responsiveness of LBL functionalized liposomes for drug delivery.[245]

Studies on the Hofmeister trends for cations have also been conducted in LBL systems. Dubas and Schlenoff examined the effect of variety of cations on the multilayer thickness made from PSS/PDADMAC.[246] The same correlation between thickness and the *B* coefficient and especially with the hydration entropy of the corresponding cation were also observed. This importance of ion hydration is significant, and underlies potential apparent differences in the behavior of traditional Hofmeister trends associated with "kosmotropic" and "chaotropic" anions and cations.

In this chapter, we examine the effect of salt identity on the phase behavior of charge-patterned complex coacervates. Furthermore, we will investigate how the thermodynamic driving force for coacervation changes as a function of salt identity using isothermal titration calorimetry (ITC). Through the probing thermodynamics, we are able to have deeper understanding of how complex coacervates interact with different salt species, and look to apply this knowledge to help develop more comprehensive design rules for complex coacervation.

5.3 Materials and Methods

5.3.1 Peptide Synthesis

Polypeptides were prepared using standard Fmoc-based solid-phase synthesis on a Liberty Blue automated microwave peptide synthesizer from CEM, Ltd.[90] Deprotection and coupling were performed under microwave irradiation on a Rink amide MBHA resin with 0.2 M Fmoc and Boc protected lysine (Fmoc-*L*-Lys(Boc)-OH, Fmoc-*D*-Lys(Boc)-OH), Fmoc and tBu protected glutamate (Fmoc-*L*-Glu(tBu)-OH, Fmoc-*D*-Glu(tBu)-OH), and Fmoc protected glycine (Fmoc-Gly-OH) in DMF. 20% Piperidine in DMF was used for Fmoc deprotection. DIC and Oxyma in a 0.5M and 1M concentration in DMF were used as activator and base, respectively.

Cleavage from the resin and side-chain deprotection was in performed using 10 mL of TFA/water/TIPS in the volumetric ratio of 95/2.5/2.5 for 3 hours at room temperature while

bubbling with carbon dioxide The cleaved product and resin were separated by filtration. The crude peptide was then precipitated into 40 mL of cold (stored at -80°C) anhydrous ethyl ether. The mixture was then centrifuged for 5 min at 5,000 rpm (Sorvall Legend X1R Centrifuge, Thermo Fisher Scientific, lnc.). The supernatant was decanted and a second round of precipitation and centrifugation was performed. The crude product was then dried *in vacuo* in a desiccator overnight.

Characterization of the final product was performed via a Bruker UltrafleXtreme (Fremont, CA, USA) matrix-assisted laser desorption/ionization time of flight mass spectrometer (MALDI-TOF). Samples of the peptide were mixed with matrix solution (approximately 50 mg/mL α-cyano-4-hydroxycinnamic acid dissolved in 1:1 mixture of water and acetonitrile with 0.05% TFA) in 1:1 ratio to reach a final concentration of approximately 7.5 mM peptide.

Poly(glutamate) with degree of polymerization $N = 50$ was synthesized using amino acids of alternating chirality (*D* and *L*) to mitigate inter-peptide hydrogen bond formation.[23,91,92] Sequence-defined poly(lysine-co-glycine) ($G(KKGG)_{12}K$, block size $\tau = 4$ as in Table 2.1) was also synthesized with a degree of polymerization $N = 50$. Lysine groups are neutralized by a TFA counterion. Glutamate groups are neutralized by sodium.[23,92]

5.3.2 Preparation of Stock Solutions

Polypeptide stock solutions were prepared gravimetrically using Milli-Q water at a concentration based on the total number of amino acids present. For instance, a stock solution of the homopolyanion poly(glutamate) of 10 mM amino acid would be used in parallel with a stock solution of a half-charged poly(lysine-co-glycine), also at 10 mM with respect to the total number of amino acids, or 5 mM with respect to the number of charged monomers present in solution. All solutions were adjusted to pH = 7.0 ±0.03 using concentrated solutions of HCl and NaOH, as needed. Monomer concentration was chosen as the experimental basis in order to easily enable

direct stoichiometric comparison of the number of positively and negatively charged units present in solution.

Sodium chloride (NaCl), sodium bromide (NaBr), potassium chloride (KCl), potassium bromide (KBr) were purchased as a powder from Sigma Aldrich. Stock solutions were prepared gravimetrically at 2 M and adjusted to pH = 7.0, as above.

5.3.3 Coacervate Preparation

Complexation was performed using stoichiometric quantities of positively and negatively charged polypeptides at a total charged residue concentration of 1 mM at pH 7.0. Under these conditions, it is a reasonable approximation to describe all of the residues on both polypeptides as fully charged. Samples were prepared by first mixing a concentrated solution of NaCl with MilliQ water in a microcentrifuge tube (1.5 mL, Eppendorf), followed by the polyanion. The resulting mixture was then vortexed for 5 s before addition of the polycation. The final mixture was vortexed for at least 15 s immediately after the addition of polycation to ensure fast mixing. The resulting phase separation causes the sample to take on a cloudy, or opalescent appearance, due to the formation of small droplets of the complex coacervate phase.

5.3.4 Determination of Salt Resistance

Samples were examined using brightfield optical microscopy (EVOS XL Core, Fisher Scientific) to determine the 'salt resistance,' or the salt concentration above which no phase separation occurred. All samples were imaged within 1 h of preparation. Error bars on measurements of the salt resistance correspond to the salt concentration intervals over which samples were examined.

5.3.5 Isothermal Titration Calorimetry (ITC)

ITC experiments were performed at 25°C on a MicroCal Auto-iTC200 system (Malvern Instruments, Ltd.) All experiments were performed by injecting a 5 mM solution of the charge-patterned polycation (with respect to the number of lysines) into the sample cell containing 0.625 mM polyanion (with respect to the number of glutamates). Both solutions were prepared at a salt concentration of 25 mM NaCl, NaBr, KCl, KBr and pH = 7.0 so as to minimize interference associated with heats of dilution. An initial injection of 0.5 μL was performed, followed by 3 injections of 2 μL each, 24 injections of 1 μL each, and then 4 injections of 2 μL each. This injection protocol was chosen to sample the various regions of the titration curve. An injection duration of 2 s followed by a 180 s equilibration time was used. Constant stirring speed is applied at a rate of 1000 rpm. All experiments were performed in triplicate.

The heat of dilution associated with injection of the charge-patterned polycation into the sample cell was measured in a separate reference experiment performed under identical conditions (pH = 7.0, 25 mM NaCl, NaBr, KCl, KBr), in the absence of polyanion in the cell. The measured heats of dilution were very small and were neglected in the subsequent data analysis. Instead, the average enthalpic change from last five titrations was subtracted from the dataset to normalize the baseline.

Following each experimental run, a rigorous cleaning procedure was implemented. To clean the sample cell, the empty cell was briefly allowed to soak in a solution of 10% Contrad 70 detergent in water at 25°C. The pipette was cleaned by rinsing with water and methanol, followed by a drying step. Finally, the transfer tubing was cleaned with detergent, water, and methanol, followed by a drying step.

5.3.6 ITC Data Analysis of Complex Coacervation

We used isothermal titration calorimetry (ITC) as a tool to experimentally probe the thermodynamics of complex coacervation. A two-step model of coacervation enables analysis of

ITC data and the separation of entropic and enthalpic contributions. The initial, 'ion pairing' between oppositely charged polymers is followed by a 'coacervation' step that results in phase separation. Details of the analysis of ITC data using the method reported previously by Priftis *et al.*[4] are discussed in Chapter 2 (Section 2.2).

5.4 Results and Discussion

5.4.1 The Effect of Salt Identity on Salt Resistance

To understand how different type of salts can influence the complex coacervation, we first examined the effect of the four alkali halide salts on the phase behavior, as described via salt resistance, for the complex coacervation of poly(glutamate) and poly(lysine-co-glycine). Here we chose monovalent alkali halide salts (NaCl, NaBr, NaCl, and KBr) to eliminate the differences of valency, and to allow for a systematic analysis of the identity of the different salts. However, Figure 5.2 shows the surprising result that the salt resistance is the same (within sampling error) for all of the different salts. This is an interesting result since we had hypothesized that the different salts should lead to differences in the measured salt resistance. However, it is possible that larger differences in the phase behavior might be apparent if the full phase diagram were mapped out as these data reflect only the dilute branch of the binodal curve.

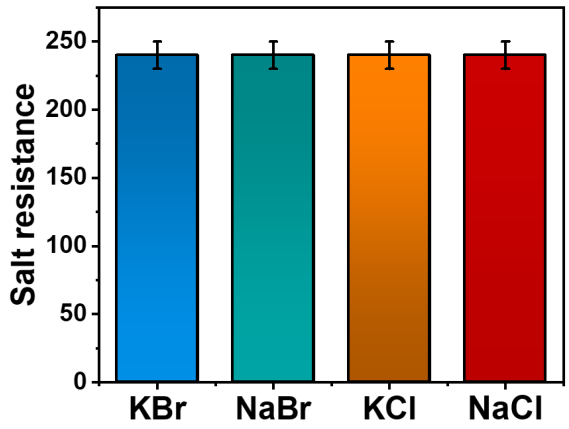

Figure 5.2. The experimentally measured salt resistance for complex coacervates of poly(glutamate) and poly(lysine-co-glycine) ($\tau = 4$) at 1 mM charged monomer concentration in the presence of different salts, pH 7.0.

Our hypothesis was based on previous work by Perry *et al*. that reported variations in the salt resistance of complex coacervates of poly(acrylic acid) and poly(allylamine hydrochloride) follows the Hofmeister series.[20] For instance, they observed that the presence of increasingly "chaotropic" salts ($I^- > Br^- > Cl^-$) decreased the salt resistance of the coacervates, since the less hydrated salt ions tended to increase the solubility of polymers and thus disfavor phase separation. It is unclear whether the significantly lower magnitude of the salt resistance for our peptide systems as compared to the vinyl polyelectrolytes used in the previous study (*i.e.*, ~240 mM vs. ~3.5 M to 4.5 M) may affect the potential difference in the observed salt resistance, or if the differences might simply be smaller than the interval over which salt resistance was sampled.

5.4.2 The Effect of Salt Identity on the Thermodynamics of Complex Coacervation

We observed a similar overall thermal signature for each of our different salt samples upon ITC analysis (Figure 5.3). Subsequent fitting of these data allows for extraction of a total enthalpy and entropy of coacervation. Consistent with the NaCl data described in Chapter 2, we observed that complex coacervation in the presence of all four different salts is an entropically driven process, with the magnitude of the calculated values for $-T\Delta S$ (Figure 5.4b) exceeding those of the unfavorable (positive) enthalpy (Figure 5.4a) by an order of magnitude. Interestingly, we observed a trend of stronger entropic gains for bromide over chloride, and for potassium over sodium. Since our experiments were performed using the same polymers, as well as the same salt concentration/ionic strength and pH, we hypothesize that these differences connected with the identity of the salt actually relate to the ways in which the various ionic species interact with water – thus, a potential Hofmeister effect.

Bromide is considered to be a more weakly hydrated ion compared to chloride. Similarly, potassium is a less hydrated ion than sodium. Our data suggest that increases in the entropic driving force for complex coacervation correlates with trends in decreasing ion hydration. As would be expected for Hofmeister-type effects, changing the anion has a much more significant impact on

the calculated entropic driving force than does altering the cation. Thus, the entropy of coacervation occurring in the presence of bromide-containing salts (KBr and NaBr) is more negative (favorable) than coacervates made with chloride salts (KCl and NaCl). For a given anion, a similar trend is also observed comparing potassium and sodium, with the more weakly hydrated potassium showing a larger entropic driving force comparing with sodium.

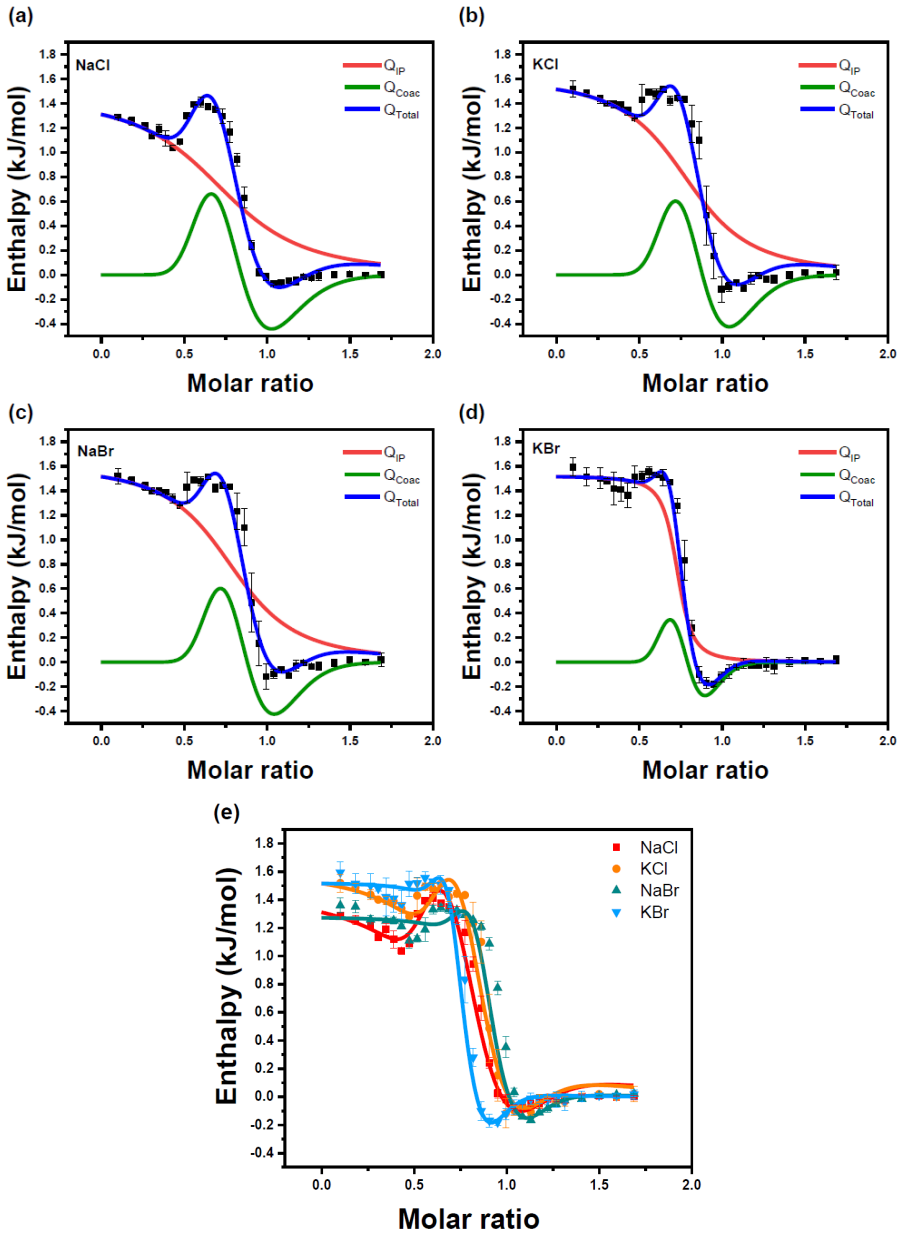

Figure 5.3. Experimental data for the molar enthalpy of complexation of poly(glutamate) and poly(lysine-co-glycine) (τ = 4) in 25 mM (a) NaCl, (b) KCl, (c) NaBr, and (d) KBr and pH = 7.0. The individual contributions from the ion

pairing (red line) and coacervation (green line) parts of the model are shown in each graph. (e) A comparison of the ITC data and curve fits for the four different salts. Lines correspond to Q_{total} in (a)-(d). Values represent the average of three runs; error bars are the standard deviation.

We believe that the trends in these data can be explained in terms of how the structure of water structure is affected by the presence of the different salts during coacervation. In the Hofmeister series, ions with a lower charge density often show a weaker interaction with water molecules, which is the reason those ions were named "chaotropes" (*i.e.*, structure breaking). Thus, as these weakly hydrated ions are released during coacervate formation, water molecules that were structured around the "condensed" counterions due to the presence of the polymer may be able to rearrange and thus have more degrees of freedom, resulting in an entropic gain.

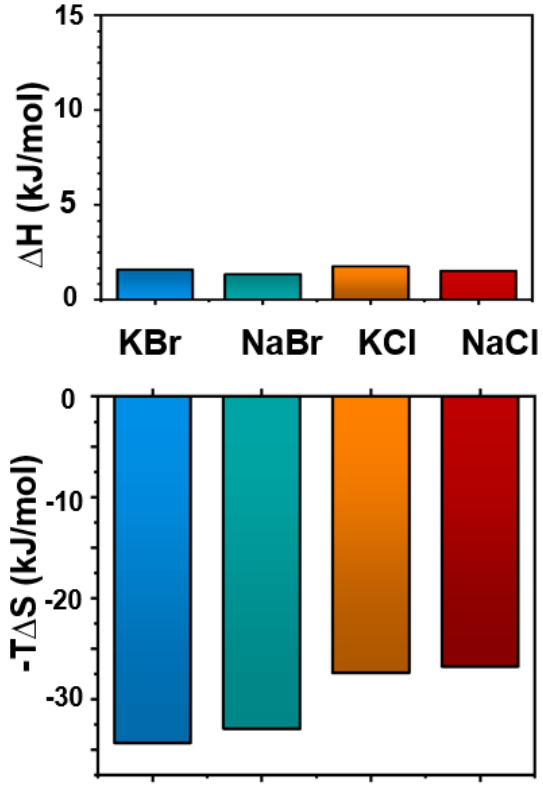

Figure 5.4. Summary of isothermal titration calorimetry results, demonstrating that complex coacervation is an entropically driven process in the presence of all four alkali halide salts. **(a)** The enthalpic contribution to coacervation is small, positive, and does not show significant differences among different salts. **(b)** The entropic contribution to the coacervation free energy is large, negative, and attributed to both counterion release and differences in the structuring of water.

Collins has proposed the concept of "matching water affinities" to explain the trends in Hofmeister series.[247–249] Generally speaking, large monovalent ions are relatively weakly hydrated, while small monovalent ions are strongly hydrated. In Collins' model, two ions of opposite charge with similar size and/or hydration levels will experience stronger electrostatic attraction than those with mismatched water affinities. This stronger attraction can allow for the formation of neutralized, "inner sphere" ion pairs, resulting in the expulsion of water molecules in the hydration sphere between these ions. However, the situation for ions with mismatched levels of hydration is very different. Here, the energetic cost of dehydrating a small, strongly hydrated ion is larger than the energetic gains resulting from the potential "inner sphere" electrostatic interactions with the more weakly hydrated ion. Thus, both ions would tend to remain fully hydrated and soluble. This concept is very similar to the general rule of "like seeks like" that is often applied in chemistry,[238,250] such as the concept proposed by Pearson of "Hard and Soft Acids and Bases (HSAB)." This theory states that "hard" acids prefer to interact with "hard" bases, and "soft" acids with "soft" bases[251–253] Building on both HSAB and the Law of Matching Water Affinities, we can describe the potential status of ion-pairs during complex coacervation as going form a "better match" with respect to the counterions interacting with the individual polymers initially, to a "worse match" after coacervation. The positively charged amine group on poly(lysine-co-glycine) is typically described as "soft," or weakly hydrated. Thus, the favorable interaction between the weakly hydrated amine and the soft, weakly hydrated chaotropic anions Cl^- and Br^- is replaced with a less favorable interaction with the hard, strongly hydrated kosmotropic carboxylate upon coacervation. A similar trend can be observed for the interactions between the negatively charged carboxylate in poly(glutamate) with its "hard" potassium or sodium counterions.

We hypothesis that this "like seeks like" might contribute to the Hofmeister trend in terms of the entropic gains driving complex coacervation in the presence of different salts. The change from "better match" to "worse match" might cause a variation in the number of water molecules

present in the hydration shell around the various ions, resulting in water restructuring and thus changes in the entropy of the system. A more detailed analysis of these various effects and the ways in which water restructuring can occur at the molecular level is still needed to further validate this hypothesis

5.5 Conclusions

In this chapter we have examined how the effect of salt identity can alter the thermodynamics and thus phase behavior of complex coacervation. In particular, results from isothermal titration calorimetry highlighted how changes in the identity of a salt can result in significant differences in the entropic driving force for coacervation. We hypothesize that this entropic difference is a consequence of the different interactions of the various ionic species with water. We observed the strongest entropic driving force in the presence of the weakly hydrated chaotropic salt KBr, and the weakest trend with the more hydrated, kosmotropic NaCl. The mechanism behind these observations could be the result of the combination of many factors, such as ion size, ion-ion interactions, ion-water interactions, water restructuring, dispersion effects, and polarizability etc., and further investigations are needed to understand the underlying physics.

CHAPTER 6

SUMMARY AND FUTURE WORK

6.1 Summary

In this research I have used sequence-controlled polypeptides to systematically analyze how parameters such as charge patterning, charge content, hydrophobicity, and the identity of counterions can be used to drive complex coacervation, an electrostatic and entropically-driven liquid-liquid phase separation phenomenon. Whereas previous studies only addressed how large-scale parameters such as average charge density affected the phase behavior of complex coacervates, my work focused on the molecular-level effects driving the polymer self-assembly. In particular, I synthesized sequence-defined polypeptides via solid-phase synthesis and examined the phase behavior of the resulting complex coacervates as a function of salt and polymer concentration. Additionally, I correlated these measurements with isothermal titration calorimetry to characterize the thermodynamics of complex coacervation. By comparing experiments with the results from theory and simulation (in collaboration with Prof. Charles Sing's group at the University of Illinois at Urbana-Champaign), we have demonstrated that the specific pattern of charges can profoundly affect the charge–charge associations that drive coacervation (Chang and Lytle *et al.*, Nature Comm. 2017, Lytle and Chang *et al.*, ACS Central Sci. 2019). Furthermore, we extended this work to characterize the effect of charge patterning on self-coacervating polyampholytes (Madinya and Chang *et al.*, Mol. Syst. Des. Eng. 2019). While these efforts have helped to clarify the role of charge patterning, I also performed preliminary investigations into the effect of changing the hydrophobicity of the neutral residues within the charge patterned polypeptides, as well as the identity of salts on complex coacervation. Our studies have identified molecular design principles that we anticipate will have broad utility in applications such as tuning the responsiveness of coacervate-based or colloidal materials for microencapsulation/emulsion or active coatings without changing the overall composition.

6.2 Future Work

6.2.1 Address the Interplay Between Charge Patterning and Hydrophobicity

Through our systematic studies on the effect of charge sequence on the phase behavior and thermodynamics of complex coacervation, we have established design principles with regards to the ways in which charge patterning affects the localization of counterions around the individual polyelectrolytes in solution, and how this effect can be used to modulate coacervate phase behavior. However, there are still some unanswered questions. While electrostatic interactions are critical for coacervation, hydrophobicity can also play a significant role. Hydrophobicity has been considered as an important factor that dictates the conformation and function of many biomacromolecules, such as protein folding.[254–256] Furthermore, hydrophobicity act orthogonally to electrostatic forces. Thus, understanding the role of hydrophobicity is critical to expand our understanding of polymer self-assembly, and particularly the non-electrostatic sequence effects associated with many biological systems.

Schlenoff *et al.* have described the contributions of hydrophobicity to association in solid polyelectrolyte complexes and multilayers, which less hydrated ions are more efficient dopants.[244] However, only a few researches about hydrophobicity in the molecular level have been conducted. Most recently, Sadman *et al.* examined coacervates made from poly(styrene sulfonate) and a modified poly(4-vinylpyridine) (QVP) with increasing side chain hydrophobicity (quaternizing with methyl, ethyl, and propyl substituents, as shown in Figure 6.1) to address the effect of hydrophobicity on polyelectrolyte complexation. The more hydrophobic modifications resulted in complexes with a lower tendency to swell in the presence of added salt, as well as stronger salt resistance. A similar trend was also observed by Tabandeh and Leon in their report describing the effect of hydrophobicity using polypeptide-based complex coacervates.[228] In this study, the authors increased the hydrophobicity of their polypeptides by replacing glycine with the more hydrophobic residues alanine and leucine. Their results also showed an increase in salt resistance with both

increasing hydrophobicity. In addition, they addressed the ways in which temperature can be harnessed in such materials as hydrophobic interactions are highly temperature-dependent.[228]

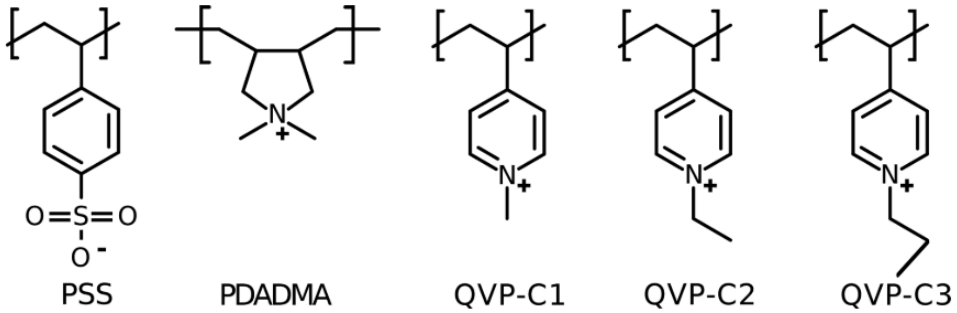

Figure 6.1. Structures and designations of the polyelectrolytes described in this chapter The counterions have been omitted for clarity.

While the results reported by Sadman *et al*. and Tabandeh and Leon provide insight into the role of hydrophobicity, these efforts have not addressed the specific question of sequence control. Therefore, future efforts in this area should build on the results from our charge patterning studies, to test the effects of increasing the hydrophobicity of the spacer from glycine (G) to alanine (A) and beyond to more hydrophobic amino acids as a function of sequence. Important considerations will be the limitations of such peptide systems in terms of solubility and coacervate formation as a function of chemical identity, sequence, hydrophobicity, charge stoichiometry, and salt concentration.

We have completed initial studies comparing the salt resistance for coacervates of poly(lysine-co-glycine) with poly(alanine-co-lysine) over a range of patterns from $\tau = 4$, 8, and 16. Coacervation in these experiments was performed with a fully charged, anionic poly(glutamate). All polymers have the same degree of polymerization $N = 50$ and were prepared using the standard solid phase synthesis methods. Preliminary experiments yielded surprising results. While the salt resistance of poly(lysine-co-glycine) coacervates increased with increasing charge block size, we observed a decrease in the salt resistance for our alanine-containing peptides (Figure 6.2). Furthermore, the magnitude of the salt resistance was lower for alanine-containing peptides compared to their equivalent glycine counterpart. As this result was unanticipated, future efforts

will need to repeat and expand these experiments. We hypothesize that one potential explanation for the differences between our results and those described in the literature is the ways in which water structures around hydrophobic sequences on our peptides.

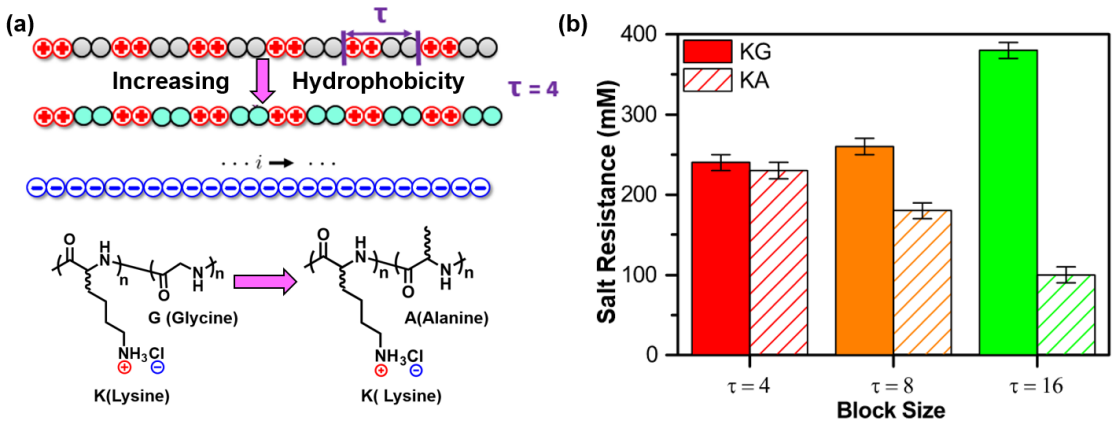

Figure 6.2. (a) We examined the effect of incorporating more hydrophobic alanine into our patterned polypeptides. **(b)** Salt resistance data comparing the effects of incorporating glycine and alanine residues into different polymer sequences.(at pH=7, 1mM polymer concentration)

An in-depth understanding of the balance between electrostatics and hydrophobicity is critical in order to obtain the full-picture of the way in which these parameters can be used to design complex coacervate materials. However, we experienced challenges related to the formation of solid precipitates upon complexation when we attempted to expand these studies to include more hydrophobic residues such as valine and leucine. To overcome this limitation, we propose to reduce the density of hydrophobic residues by increasing the fraction of charged residues from f_C = 0.5 to 0.8. We anticipate that lowering the overall hydrophobic content of the peptides will allow us to avoid precipitation. Once we identify an optimal charge fraction to allow us probe hydrophobic effect, we can start to extend the chemistry to even more hydrophobic amino acids such as valine (V), Leucine (L), phenylalanine (F) and tryptophan (W).

6.2.2 Expand Studies of Salt Identity over a Wider Range in the Hofmeister Series

From Chapter 5, we observed variations in the entropic driving force for complex coacervation in the presence of different monovalent salts. These differences correlated with trends described by the Hofmeister series, but did not translate to measurable differences in the salt resistance. To further investigate this observation, we propose to expand our study to include additional ions salts that span more broadly the Hofmeister series. These ions would expand upon both our initial data looking at alkali halides, and would include the effect of different ion valence, as well as both organic and inorganic ions. We can also expand our study to consider how different polymer systems respond to salt identity. We proposed to expand our research of salt identity to include polymers with different molecular weights, charge fraction, charge pattern, charge group identity, and polymer hydrophobicity. Through systematically addressing the effect of salt identity, we expect to unveil the underlying physics of the Hofmeister behavior in complex coacervation.

6.2.3 Study Sequence Effects in Industrially-relevant Statistical Polymers

While polypeptides provide us with an ideal platform to study the detailed effects of chemical sequence on complex coacervation, such materials are too expensive for the majority of real-world applications. Thus, we are looking to extend our knowledge of sequence effects to industrially-relevant polymer systems where the size and distribution of charge blocks must be described by a statistical distribution, rather than a specific pattern, in addition to the inherent polydispersity of the overall polymer.

Large-scale synthesis will result in the preparation of polymers containing a known composition of comonomers in a statistical distribution. Thus, it is possible to mathematically predict the expected distribution of charged and uncharged blocks. We can utilize our polypeptide system to study the effect of such a distribution of charged blocks. We propose the design and preparation of three sets of poly(lysine-co-glycine) copolymers with different content and distributions of the charged blocks. For each of these distributions, three different peptides with the

same distribution but different, known sequences can be prepared. We hypothesize that sequence effects in these designed "random" materials (*e.g.* salt resistance, thermodynamic parameters) can be described by a convolution of the most common block size and the width of the distribution.

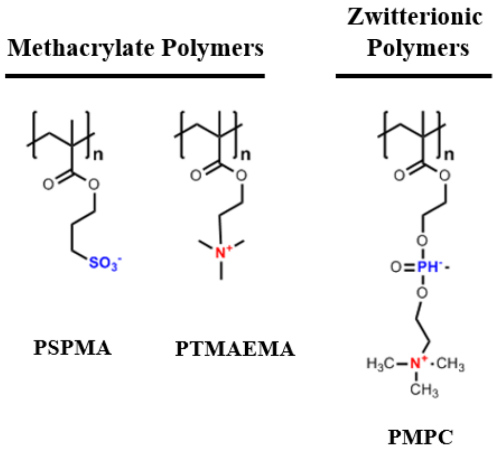

Figure 6.3. Chemical structure of the industrially-relevant polymers: poly(3-sulfopropyl methacrylate) (PSPMA) and poly(2-(N,N,N-trimethyl amino)-ethyl methacrylate) (PTMAEMA), and the zwitterionic copolymer poly(2-methacryloyloxyethyl- phosphorylcholine) (PMPC) that will be used in this study.

We can then compare the trends observed for our polypeptide system with those from a methacrylate copolymer system. We propose the use of poly(3-sulfopropyl methacrylate) (PSPMA) as an unpatterned polyanion, and will synthesize various copolymers of the cationic poly(2-(N,N,N-trimethyl amino)-ethyl methacrylate) (PTMAEMA) and the neutral, zwitterionic poly(2-methacryloyloxyethyl phosphorylcholine) (PMPC) in collaboration with Prof. Todd Emrick's lab (Figure 6.3). Based on the kinetics of the polymerization reactions, we will be able to predict the statistical distribution of charged and neutral blocks in our polymers. These distributions will be used in designing our "random" polypeptide materials. These methacrylate polymers can be prepared in gram-scale quantities that will allow for extensive characterization of not only the self-assembly and phase behavior, but also of their rheological properties and potential for use in applications such as coatings.

6.3 Conclusions

From the study of charge patterning, we successfully prove that we can modulate the phase behavior of complex coacervates via sequence control. Moreover, preliminary indications suggest that the way charge and hydrophobicity of polymers interplay with each other can affect whether complexes undergo precipitation or coacervation, as well as their phase behavior. Hence, we hypothesize there is an optimal charge density for polymers with different levels of hydrophobicity to form coacervates. We believe that investigation of the optimal distribution of charge and hydrophobic monomers can allow us to obtain design rules for further applications, and that we can export these concepts to industrially-relevant polymers to further examine the rheological and material properties.

BIBLIOGRAPHY

(1) Priftis, D.; Megley, K.; Laugel, N.; Tirrell, M. Complex coacervation of poly(ethylene-imine)/polypeptide aqueous solutions: Thermodynamic and rheological characterization. *J. Colloid Interface Sci.* **2013**, *398*, 39–50 DOI: 10.1016/j.jcis.2013.01.055.

(2) Priftis, D.; Farina, R.; Tirrell, M. Interfacial energy of polypeptide complex coacervates measured via capillary adhesion. *Langmuir* **2012**, *28* (23), 8721–8729 DOI: 10.1021/la300769d.

(3) Priftis, D.; Tirrell, M. Phase behaviour and complex coacervation of aqueous polypeptide solutions. *Soft Matter* **2012**, *8* (36), 9396–9405 DOI: 10.1039/c2sm25604e.

(4) Priftis, D.; Laugel, N.; Tirrell, M. Thermodynamic characterization of polypeptide complex coacervation. *Langmuir* **2012**, *28* (45), 15947–15957 DOI: 10.1021/la302729r.

(5) Qin, J.; Priftis, D.; Farina, R.; Perry, S. L.; Leon, L.; Whitmer, J.; Hoffmann, K.; Tirrell, M.; De Pablo, J. J. Interfacial tension of polyelectrolyte complex coacervate phases. *ACS Macro Lett.* **2014**, *3* (6), 565–568 DOI: 10.1021/mz500190w.

(6) Black, K. A.; Priftis, D.; Perry, S. L.; Yip, J.; Byun, W. Y.; Tirrell, M. Protein encapsulation via polypeptide complex coacervation. *ACS Macro Lett.* **2014**, *3* (10), 1088–1091 DOI: 10.1021/mz500529v.

(7) Patel, A.; Lee, H. O.; Jawerth, L.; Maharana, S.; Jahnel, M.; Hein, M. Y.; Stoynov, S.; Mahamid, J.; Saha, S.; Franzmann, T. M.; Pozniakovski, A.; Poser, I.; Maghelli, N.; Royer, L. A.; Weigert, M.; Myers, E. W.; Grill, S.; Drechsel, D.; Hyman, A. A.; Alberti, S. A Liquid-to-Solid Phase Transition of the ALS Protein FUS Accelerated by Disease Mutation. *Cell* **2015**, *162* (5), 1066–1077 DOI: 10.1016/j.cell.2015.07.047.

(8) Pak, C. W.; Kosno, M.; Holehouse, A. S.; Padrick, S. B.; Mittal, A.; Ali, R.; Yunus, A. A.; Liu, D. R.; Pappu, R. V.; Rosen, M. K. Sequence Determinants of Intracellular Phase Separation by Complex Coacervation of a Disordered Protein. *Mol. Cell* **2016**, *63* (1), 72–85 DOI: 10.1016/j.molcel.2016.05.042.

(9) Das, R. K.; Pappu, R. V. Conformations of intrinsically disordered proteins are influenced by linear sequence distributions of oppositely charged residues. *Proc. Natl. Acad. Sci. U. S. A.* **2013**, *110* (33), 13392–13397 DOI: 10.1073/pnas.1304749110.

(10) Kayitmazer, A. B.; Koksal, A. F.; Kilic Iyilik, E. Complex coacervation of hyaluronic acid and chitosan: Effects of pH, ionic strength, charge density, chain length and the charge ratio. *Soft Matter* **2015**, *11* (44), 8605–8612 DOI: 10.1039/c5sm01829c.

(11) Spruijt, E.; Westphal, A. H.; Borst, J. W.; Cohen Stuart, M. A.; Van Der Gucht, J. Binodal compositions of polyelectrolyte complexes. *Macromolecules* **2010**, *43* (15), 6476–6484 DOI: 10.1021/ma101031t.

(12) Chollakup, R.; Beck, J. B.; Dirnberger, K.; Tirrell, M.; Eisenbach, C. D. Polyelectrolyte molecular weight and salt effects on the phase behavior and coacervation of aqueous solutions of poly(acrylic acid) sodium salt and poly(allylamine) hydrochloride. *Macromolecules* **2013**, *46* (6), 2376–2390 DOI: 10.1021/ma202172q.

(13) Kayitmazer, A. B.; Strand, S. P.; Tribet, C.; Jaeger, W.; Dubin, P. L. Effect of polyelectrolyte structure on protein - Polyelectrolyte coacervates: Coacervates of bovine serum albumin with poly(diallyldimethylammonium chloride) versus chitosan. *Biomacromolecules* **2007**, *8* (11), 3568–3577 DOI: 10.1021/bm700645t.

(14) Johnston, B. M.; Johnston, C. W.; Letteri, R. A.; Lytle, T. K.; Sing, C. E.; Emrick, T.; Perry, S. L. The effect of comb architecture on complex coacervation. *Org. Biomol. Chem.* **2017**, *15* (36), 7630–7642 DOI: 10.1039/c7ob01314k.

(15) De La Rica, R.; Matsui, H. Applications of peptide and protein-based materials in bionanotechnology. *Chem. Soc. Rev.* **2010**, *39* (9), 3499–3509 DOI: 10.1039/b917574c.

(16) Tamerler, C.; Sarikaya, M. Genetically designed peptide-based molecular materials. *ACS Nano* **2009**, *3* (7), 1606–1615 DOI: 10.1021/nn900720g.

(17) Bungenberg de Jong, H. G.; Kruyt, H. R. Coacervation (partial miscibility in colloid systems). *Proc.Acad.Sci Amsterdam* **1929**, *32*, 849–856.

(18) Gucht, J. van der; Spruijt, E.; Lemmers, M.; Cohen Stuart, M. A. Polyelectrolyte complexes: Bulk phases and colloidal systems. *J. Colloid Interface Sci.* **2011**, *361* (2), 407–422 DOI: 10.1016/j.jcis.2011.05.080.

(19) Bowman, W. A.; Rubinstein, M.; Tan, J. S. Polyelectrolyte-Gelatin Complexation: Light-Scattering Study. *Macromolecules* **1997**, *30* (11), 3262–3270 DOI: 10.1021/ma961915u.

(20) Perry, S. L.; Li, Y.; Priftis, D.; Leon, L.; Tirrell, M. The effect of salt on the complex coacervation of vinyl polyelectrolytes. *Polymers (Basel).* **2014**, *6* (6), 1756–1772 DOI: 10.3390/polym6061756.

(21) Priftis, D.; Leon, L.; Song, Z.; Perry, S. L.; Margossian, K. O.; Tropnikova, A.; Cheng, J.; Tirrell, M. Self-Assembly of α-Helical Polypeptides Driven by Complex Coacervation. *Angew. Chemie* **2015**, *127* (38), 11280–11284 DOI: 10.1002/ange.201504861.

(22) Water, J. J.; Schack, M. M.; Velazquez-Campoy, A.; Maltesen, M. J.; Van De Weert, M.; Jorgensen, L. Complex coacervates of hyaluronic acid and lysozyme: Effect on protein structure and physical stability. *Eur. J. Pharm. Biopharm.* **2014**, *88* (2), 325–331 DOI: 10.1016/j.ejpb.2014.09.001.

(23) Hoffmann, K. Q.; Perry, S. L.; Leon, L.; Priftis, D.; Tirrell, M.; De Pablo, J. J. A molecular view of the role of chirality in charge-driven polypeptide complexation. *Soft Matter* **2015**, *11* (8), 1525–1538 DOI: 10.1039/c4sm02336f.

(24) Stewart, R. J.; Ransom, T. C.; Hlady, V. Natural underwater adhesives. *J. Polym. Sci. Part B Polym. Phys.* **2011**, *49* (11), 757–771 DOI: 10.1002/polb.22256.

(25) Shao, H.; Stewart, R. J. Biomimetic underwater adhesives with environmentally triggered setting mechanisms. *Adv. Mater.* **2010**, *22* (6), 729–733 DOI: 10.1002/adma.200902380.

(26) Lim, S.; Choi, Y. S.; Kang, D. G.; Song, Y. H.; Cha, H. J. The adhesive properties of coacervated recombinant hybrid mussel adhesive proteins. *Biomaterials* **2010**, *31* (13), 3715–3722 DOI: 10.1016/j.biomaterials.2010.01.063.

(27) Hwang, D. S.; Zeng, H.; Srivastava, A.; Krogstad, D. V.; Tirrell, M.; Israelachvili, J. N.; Waite, J. H. Viscosity and interfacial properties in a mussel-inspired adhesive coacervate. *Soft Matter* **2010**, *6* (14), 3232–3236 DOI: 10.1039/c002632h.

(28) Wright, P. E.; Dyson, H. J. Intrinsically unstructured proteins: Re-assessing the protein structure-function paradigm. *J. Mol. Biol.* **1999**, *293* (2), 321–331 DOI: 10.1006/jmbi.1999.3110.

(29) Uversky, V. N.; Gillespie, J. R.; Fink, A. L. Why are "natively unfolded" proteins unstructured under physiologic conditions? *Proteins Struct. Funct. Genet.* **2000**, *41* (3), 415–427 DOI: 10.1002/1097-0134(20001115)41:3<415::AID-PROT130>3.0.CO;2-7.

(30) Oldfield, C. J.; Dunker, A. K. Intrinsically Disordered Proteins and Intrinsically Disordered Protein Regions. *Annu. Rev. Biochem.* **2014**, *83* (1), 553–584 DOI: 10.1146/annurev-biochem-072711-164947.

(31) Wuttke, R.; Hofmann, H.; Nettels, D.; Borgia, M. B.; Mittal, J.; Best, R. B.; Schuler, B. Temperature-dependent solvation modulates the dimensions of disordered proteins. In *Proceedings of the National Academy of Sciences of the United States of America*; organizers of cellular biochemistry. Nat. Rev. Mol. Cell Biol 18, 285?298, 2014; Vol. 111, pp 5213–5218.

(32) Taylor, N.; Elbaum-Garfinkle, S.; Vaidya, N.; Zhang, H.; Stone, H. A.; Brangwynne, C. P. Biophysical characterization of organelle-based RNA/protein liquid phases using microfluidics. *Soft Matter* **2016**, *12* (45), 9142–9150 DOI: 10.1039/C6SM01087C.

(33) Hyman, A. A.; Weber, C. A.; Jülicher, F. Liquid-Liquid Phase Separation in Biology. *Annu. Rev. Cell Dev. Biol.* **2014**, *30* (1), 39–58 DOI: 10.1146/annurev-cellbio-100913-013325.

(34) Perry, S. L. Phase separation: Bridging polymer physics and biology. *Curr. Opin. Colloid Interface Sci.* **2019**, *39*, 86–97 DOI: 10.1016/j.cocis.2019.01.007.

(35) Chang, L. W.; Madinya, J. J.; Perry, S. L.; Sing, C. E. Sequence-Dependent Self-Coacervation in High Charge-Density Polyampholytes. **2019** DOI: 10.1039/C9ME00074G.MSDE.

(36) Martin, E. W.; Mittag, T. Relationship of Sequence and Phase Separation in Protein Low-Complexity Regions. *Biochemistry* **2018**, *57* (17), 2478–2487 DOI: 10.1021/acs.biochem.8b00008.

(37) Weber, S. C. Sequence-encoded material properties dictate the structure and function of nuclear bodies. *Curr. Opin. Cell Biol.* **2017**, *46*, 62–71 DOI: 10.1016/j.ceb.2017.03.003.

(38) Wang, J.; Choi, J. M.; Holehouse, A. S.; Lee, H. O.; Zhang, X.; Jahnel, M.; Maharana, S.; Lemaitre, R.; Pozniakovsky, A.; Drechsel, D.; Poser, I.; Pappu, R. V.; Alberti, S.; Hyman, A. A. A Molecular Grammar Governing the Driving Forces for Phase Separation of Prion-like RNA Binding Proteins. *Cell* **2018**, *174* (3), 688-699.e16 DOI: 10.1016/j.cell.2018.06.006.

(39) Simon, J. R.; Carroll, N. J.; Rubinstein, M.; Chilkoti, A.; López, G. P. Programming molecular self-assembly of intrinsically disordered proteins containing sequences of low complexity. *Nat. Chem.* **2017**, *9* (6), 509–515 DOI: 10.1038/nchem.2715.

(40) Quiroz, F. G.; Chilkoti, A. Sequence heuristics to encode phase behaviour in intrinsically disordered protein polymers. *Nat. Mater.* **2015**, *14* (11), 1164–1171 DOI: 10.1038/nmat4418.

(41) Ruff, K. M.; Roberts, S.; Chilkoti, A.; Pappu, R. V. Advances in Understanding Stimulus-Responsive Phase Behavior of Intrinsically Disordered Protein Polymers. *J. Mol. Biol.* **2018**, *430* (23), 4619–4635 DOI: 10.1016/j.jmb.2018.06.031.

(42) Elder, R. M.; Jayaraman, A. Molecular simulations of polycation-DNA binding exploring the effect of peptide chemistry and sequence in nuclear localization sequence based polycations. *J. Phys. Chem. B* **2013**, *117* (40), 11988–11999 DOI: 10.1021/jp406875a.

(43) Rutten, M. G. T. A.; Vaandrager, F. W.; Elemans, J. A. A. W.; Nolte, R. J. M. Encoding information into polymers. *Nat. Rev. Chem.* **2018**, *2* (11), 365–381 DOI: 10.1038/s41570-018-0051-5.

(44) Mao, S.; MacPherson, Q.; Qin, J.; Spakowitz, A. J. Field-theoretic simulations of random copolymers with structural rigidity. *Soft Matter* **2017**, *13* (15), 2760–2772 DOI: 10.1039/C7SM00164A.

(45) Levine, W. G.; Seo, Y.; Brown, J. R.; Hall, L. M. Effect of sequence dispersity on morphology of tapered diblock copolymers from molecular dynamics simulations. *J. Chem. Phys.* **2016**, *145*, 234907 DOI: 10.1063/1.4972141.

(46) Meenakshisundaram, V.; Hung, J. H.; Patra, T. K.; Simmons, D. S. Designing Sequence-Specific Copolymer Compatibilizers Using a Molecular-Dynamics-Simulation-Based Genetic Algorithm. *Macromolecules* **2017**, *50* (3), 1155–1166 DOI: 10.1021/acs.macromol.6b01747.

(47) Seitz, M. E.; Chan, C. D.; Opper, K. L.; Baughman, T. W.; Wagener, K. B.; Winey, K. I. Nanoscale morphology in precisely sequenced poly(ethylene- co -acrylic acid) zinc ionomers. *J. Am. Chem. Soc.* **2010**, *132* (23), 8165–8174 DOI: 10.1021/ja101991d.

(48) Murnen, H. K.; Khokhlov, A. R.; Khalatur, P. G.; Segalman, R. A.; Zuckermann, R. N. Impact of hydrophobic sequence patterning on the coil-to-globule transition of protein-like polymers. *Macromolecules* **2012**, *45* (12), 5229–5236 DOI: 10.1021/ma300707t.

(49) Rosales, A. M.; Segalman, R. A.; Zuckermann, R. N. Erratum: Polypeptoids: A model system to study the effect of monomer sequence on polymer properties and self-assembly (Soft Matter (2013) 9 (8400-8414) DOI: 10.1039/C3SM51421H). *Soft Matter* **2013**, *9* (48), 11713 DOI: 10.1039/C3SM90168H.

(50) Patterson, A. L.; Wenning, B.; Rizis, G.; Calabrese, D. R.; Finlay, J. A.; Franco, S. C.; Zuckermann, R. N.; Clare, A. S.; Kramer, E. J.; Ober, C. K.; Segalman, R. A. Role of Backbone Chemistry and Monomer Sequence in Amphiphilic Oligopeptide- and Oligopeptoid-Functionalized PDMS- and PEO-Based Block Copolymers for Marine Antifouling and Fouling Release Coatings. *Macromolecules* **2017**, *50* (7), 2656–2667 DOI: 10.1021/acs.macromol.6b02505.

(51) Leng, C.; Buss, H. G.; Segalman, R. A.; Chen, Z. Surface Structure and Hydration of Sequence-Specific Amphiphilic Polypeptoids for Antifouling/Fouling Release Applications. *Langmuir* **2015**, *31* (34), 9306–9311 DOI: 10.1021/acs.langmuir.5b01440.

(52) Das, R. K.; Pappu, R. V. Conformations of intrinsically disordered proteins are influenced by linear sequence distributions of oppositely charged residues. *Proc. Natl. Acad. Sci. U. S. A.* **2013**, *110* (33), 13392–13397 DOI: 10.1073/pnas.1304749110.

(53) Hunt, J. N.; Feldman, K. E.; Lynd, N. A.; Deek, J.; Campos, L. M.; Spruell, J. M.; Hernandez, B. M.; Kramer, E. J.; Hawker, C. J. Tunable, high modulus hydrogels driven by ionic coacervation. *Adv. Mater.* **2011**, *23* (20), 2327–2331 DOI: 10.1002/adma.201004230.

(54) Pergushov, D. V.; Müller, A. H. E.; Schacher, F. H. Micellar interpolyelectrolyte complexes. *Chem. Soc. Rev.* **2012**, *41* (21), 6888–6901 DOI: 10.1039/c2cs35135h.

(55) Harada, A.; Kataoka, K. Chain length recognition: Core-shell supramolecular assembly from oppositely charged block copolymers. *Science (80-.).* **1999**, *283* (5398), 65–67 DOI: 10.1126/science.283.5398.65.

(56) Krogstad, D. V.; Lynd, N. A.; Choi, S. H.; Spruell, J. M.; Hawker, C. J.; Kramer, E. J.; Tirrell, M. V. Effects of polymer and salt concentration on the structure and properties of triblock copolymer coacervate hydrogels. *Macromolecules* **2013**, *46* (4), 1512–1518 DOI: 10.1021/ma302299r.

(57) Stewart, R. J.; Wang, C. S.; Shao, H. Complex coacervates as a foundation for synthetic underwater adhesives. *Adv. Colloid Interface Sci.* **2011**, *167* (1–2), 85–93 DOI: 10.1016/j.cis.2010.10.009.

(58) Zhao, Q.; Lee, D. W.; Ahn, B. K.; Seo, S.; Kaufman, Y.; Israelachvili, J. N.; Waite, J. H. Underwater contact adhesion and microarchitecture in polyelectrolyte complexes actuated by solvent exchange. *Nat. Mater.* **2016**, *15* (4), 407–412 DOI: 10.1038/nmat4539.

(59) Weinbreck, F.; de Vries, R.; Schrooyen, P.; de Kruif, C. G. Complex coacervation of whey proteins and gum arabic. *Biomacromolecules* **2003**, *4*, 293–303.

(60) Vecchies, F.; Sacco, P.; Decleva, E.; Menegazzi, R.; Porrelli, D.; Donati, I.; Turco, G.; Paoletti, S.; Marsich, E. Complex Coacervates between a Lactose-Modified Chitosan and Hyaluronic Acid as Radical-Scavenging Drug Carriers. *Biomacromolecules* **2018**, *19* (10), 3936–3944 DOI: 10.1021/acs.biomac.8b00863.

(61) Johnson, N. R.; Ambe, T.; Wang, Y. Lysine-based polycation:heparin coacervate for controlled protein delivery. *Acta Biomater.* **2014**, *10* (1), 40–46 DOI: 10.1016/j.actbio.2013.09.012.

(62) Johnson, N. R.; Wang, Y. Coacervate delivery systems for proteins and small molecule drugs. *Expert Opin. Drug Deliv.* **2014**, *11* (12), 1829–1832 DOI: 10.1517/17425247.2014.941355.

(63) Tromp, R. H.; De Kruif, C. G.; Van Eijk, M.; Rolin, C. On the mechanism of stabilisation of acidified milk drinks by pectin. *Food Hydrocoll.* **2004**, *18* (4), 565–572 DOI: 10.1016/j.foodhyd.2003.09.005.

(64) Tuinier, R.; Rolin, C.; de Kruif, C. G. Electrosorption of pectin onto casein micelles. *Biomacromolecules* **2002**, *3* (3), 632–638 DOI: 10.1021/bm025530x.

(65) Gupta, N.; Lin, B. F.; Campos, L. M.; Dimitriou, M. D.; Hikita, S. T.; Treat, N. D.; Tirrell, M. V.; Clegg, D. O.; Kramer, E. J.; Hawker, C. J. A versatile approach to high-throughput microarrays using thiol-ene chemistry. *Nat. Chem.* **2012**, *4* (5), 424–424 DOI: 10.1038/nchem.1328.

(66) Nowak, A. P.; Breedveld, V.; Pakstis, L.; Ozbas, B.; Pine, D. J.; Deming, T. J. Rapidly recovering hydrogel scaffolds from self-assembling diblock copolypeptide amphiphiles. *Nature* **2002**, *417* (6887), 424–428 DOI: 10.1038/417424a.

(67) Kurtz, I. S.; Sui, S.; Hao, X.; Huang, M.; Perry, S. L.; Schiffman, J. D. Bacteria-Resistant, Transparent, Free-Standing Films Prepared from Complex Coacervates. *ACS Appl. Bio Mater.* **2019**, *2* (9), 3926–3933 DOI: 10.1021/acsabm.9b00502.

(68) Overbeek, J. T.; Voorn, M. J. Phase separation in polyelectrolyte solutions; theory of complex coacervation. *J. Cell. Physiol. Suppl.* **1957**, *49* (Suppl 1), 7–26 DOI: 10.1002/jcp.1030490404.

(69) Lytle, T. K.; Sing, C. E. Transfer matrix theory of polymer complex coacervation. *Soft Matter* **2017**, *13* (39), 7001–7012 DOI: 10.1039/c7sm01080j.

(70) Michaeli, I.; Overbeek, J. T. G.; Voorn, M. J. Phase separation of polyelectrolyte solutions. *J. Polym. Sci.* **1957**, *23* (103), 443–450 DOI: 10.1002/pol.1957.1202310337.

(71) Debye, P.; Huckel, E. Theory of electrolytes. *Phys. Z* **1923**, *24*, 185.

(72) Radhakrishna, M.; Basu, K.; Liu, Y.; Shamsi, R.; Perry, S. L.; Sing, C. E. Molecular Connectivity and Correlation Effects on Polymer Coacervation. *Macromolecules* **2017**, *50* (7), 3030–3037 DOI: 10.1021/acs.macromol.6b02582.

(73) Lytle, T. K.; Salazar, A. J.; Sing, C. E. Interfacial properties of polymeric complex coacervates from simulation and theory. *J. Chem. Phys.* **2018**, *149* (16), 16331 DOI: 10.1063/1.5029934.

(74) Lytle, T. K.; Sing, C. E. Tuning chain interaction entropy in complex coacervation using polymer stiffness, architecture, and salt valency. *Mol. Syst. Des. Eng.* **2018**, *3* (1), 183–196 DOI: 10.1039/c7me00108h.

(75) Lutz, J.-F.; Ouchi, M.; Liu, D. R.; Sawamoto, M. Sequence-Controlled Polymers. *Science (80-.).* **2013**, *341* (6146), 1238149–1238149 DOI: 10.1126/science.1238149.

(76) Lutz, J. F.; Lehn, J. M.; Meijer, E. W.; Matyjaszewski, K. From precision polymers to complex materials and systems. *Nat. Rev. Mater.* **2016**, *1*, 1–14 DOI: 10.1038/natrevmats.2016.24.

(77) Dudowicz, J.; Freed, K. F. Relation of Effective Interaction Parameters for Binary Blends and Diblock Copolymers: Lattice Cluster Theory Predictions and Comparisons with Experiment. *Macromolecules* **1993**, *26* (1), 213–220 DOI: 10.1021/ma00053a033.

(78) Flory, P. J. *Principles of Polymer Chemistry*; Cornell University Press: Ithaca, NY, 1953.

(79) Brangwynne, C. P.; Tompa, P.; Pappu, R. V. Polymer physics of intracellular phase transitions. *Nat. Phys.* **2015**, *11* (11), 899–904 DOI: 10.1038/nphys3532.

(80) Feric, M.; Vaidya, N.; Harmon, T. S.; Mitrea, D. M.; Zhu, L.; Richardson, T. M.; Kriwacki, R. W.; Pappu, R. V.; Brangwynne, C. P. Coexisting Liquid Phases Underlie Nucleolar Subcompartments. *Cell* **2016**, *165* (7), 1686–1697 DOI: 10.1016/j.cell.2016.04.047.

(81) Miller, T.; Goude, M. C.; Mcdevitt, T. C.; Temenoff, J. S. Molecular engineering of glycosaminoglycan chemistry for biomolecule delivery. *Acta Biomaterialia*. 2014, pp 1705–1719.

(82) Lin, Y. H.; Chan, H. S. Phase Separation and Single-Chain Compactness of Charged Disordered Proteins Are Strongly Correlated. *Biophys. J.* **2017**, *112* (10), 2043–2046 DOI: 10.1016/j.bpj.2017.04.021.

(83) Merrifield, R. B. Solid Phase Peptide Synthesis. I. The Synthesis of a Tetrapeptide. *J. Am. Chem. Soc.* **1963**, *85* (14), 2149–2154 DOI: 10.1021/ja00897a025.

(84) Culf, A. S.; Ouellette, R. J. Solid-phase synthesis of N-substituted glycine oligomers (α-peptoids) and derivatives. *Molecules* **2010**, *15* (8), 5282–5335 DOI: 10.3390/molecules15085282.

(85) Barnes, J. C.; Ehrlich, D. J. C.; Gao, A. X.; Leibfarth, F. A.; Jiang, Y.; Zhou, E.; Jamison, T. F.; Johnson, J. A. Iterative exponential growth of stereo- and sequence-controlled polymers. *Nat. Chem.* **2015**, *7* (10), 810–815 DOI: 10.1038/nchem.2346.

(86) Solleder, S. C.; Zengel, D.; Wetzel, K. S.; Meier, M. A. R. A scalable and high-yield strategy for the synthesis of sequence-defined macromolecules. *Angew. Chemie - Int. Ed.* **2016**, *55* (3), 1204–1207 DOI: 10.1002/anie.201509398.

(87) Zydziak, N.; Feist, F.; Huber, B.; Mueller, J. O.; Barner-Kowollik, C. Photo-induced sequence defined macromolecules via hetero bifunctional synthons. *Chem. Commun.* **2015**, *51* (10), 1799–1802 DOI: 10.1039/c4cc08756a.

(88) Hall, L. M.; Seitz, M. E.; Winey, K. I.; Opper, K. L.; Wagener, K. B.; Stevens, M. J.; Frischknecht, A. L. Ionic aggregate structure in ionomer melts: Effect of molecular architecture on aggregates and the ionomer peak. *J. Am. Chem. Soc.* **2012**, *134* (1), 574–587 DOI: 10.1021/ja209142b.

(89) Mao, S.; Macpherson, Q. J.; He, S. S.; Coletta, E.; Spakowitz, A. J. Impact of Conformational and Chemical Correlations on Microphase Segregation in Random Copolymers. *Macromolecules* **2016**, *49* (11), 4358–4368 DOI: 10.1021/acs.macromol.5b02639.

(90) Amblard, M.; Fehrentz, J. A.; Martinez, J.; Subra, G. Methods and protocols of modern solid phase peptide synthesis. *Molecular Biotechnology*. 2006, pp 239–254.

(91) Perry, S. L.; Leon, L.; Hoffmann, K. Q.; Kade, M. J.; Priftis, D.; Black, K. A.; Wong, D.; Klein, R. A.; Pierce, C. F.; Margossian, K. O.; Whitmer, J. K.; Qin, J.; De Pablo, J. J.; Tirrell, M. Chirality-selected phase behaviour in ionic polypeptide complexes. *Nat. Commun.* **2015**, *6*, 6052 DOI: 10.1038/ncomms7052.

(92) Pacalin, N. M.; Leon, L.; Tirrell, M. Directing the phase behavior of polyelectrolyte complexes using chiral patterned peptides. *Eur. Phys. J. Spec. Top.* **2016**, *225* (8–9), 1805–1815 DOI: 10.1140/epjst/e2016-60149-6.

(93) Lytle, T. K.; Radhakrishna, M.; Sing, C. E. High Charge Density Coacervate Assembly via Hybrid Monte Carlo Single Chain in Mean Field Theory. *Macromolecules* **2016**, *49* (24), 9693–9705 DOI: 10.1021/acs.macromol.6b02159.

(94) Hansen, J. P.; McDonald, I. R. *Theory of Simple Liquids*; Elsevier: Boston, 2006.

(95) Frenkel, D.; Smit, B. *Understanding Molecular Simulation*; Elsevier: San Diego, CA, 2002.

(96) Laaser, J. E.; McGovern, M.; Jiang, Y.; Lohmann, E.; Reineke, T. M.; Morse, D. C.; Dorfman, K. D.; Lodge, T. P. Equilibration of Micelle-Polyelectrolyte Complexes: Mechanistic Differences between Static and Annealed Charge Distributions. *J. Phys. Chem. B* **2017**, *121* (17), 4631–4641 DOI: 10.1021/acs.jpcb.7b01953.

(97) Srivastava, S.; Andreev, M.; Levi, A. E.; Goldfeld, D. J.; Mao, J.; Heller, W. T.; Prabhu, V. M.; De Pablo, J. J.; Tirrell, M. V. Gel phase formation in dilute triblock copolyelectrolyte complexes. *Nat. Commun.* **2017**, *8*, 1–9 DOI: 10.1038/ncomms14131.

(98) Krogstad, D. V.; Choi, S. H.; Lynd, N. A.; Audus, D. J.; Perry, S. L.; Gopez, J. D.; Hawker, C. J.; Kramer, E. J.; Tirrell, M. V. Small Angle Neutron Scattering Study of Complex Coacervate Micelles and Hydrogels Formed from Ionic Diblock and Triblock Copolymers. *J. Phys. Chem. B* **2014**, *118* (45), 13011–13018 DOI: 10.1021/jp509175a.

(99) Audus, D. J.; Gopez, J. D.; Krogstad, D. V.; Lynd, N. A.; Kramer, E. J.; Hawker, C. J.; Fredrickson, G. H. Phase behavior of electrostatically complexed polyelectrolyte gels using an embedded fluctuation model. *Soft Matter* **2015**, *11* (6), 1214–1225 DOI: 10.1039/c4sm02299h.

(100) Castelnovo, M.; Joanny, J. F. Complexation between oppositely charged polyelectrolytes: Beyond the Random Phase Approximation. *Eur. Phys. J. E* **2001**, *6* (5), 377–386 DOI: 10.1007/s10189-001-8051-7.

(101) Kudlay, A.; Ermoshkin, A. V.; De La Cruz, M. O. Complexation of oppositely charged polyelectrolytes: Effect of ion pair formation. *Macromolecules* **2004**, *37* (24), 9231–9241 DOI: 10.1021/ma048519t.

(102) Lee, J.; Popov, Y. O.; Fredrickson, G. H. Complex coacervation: A field theoretic simulation study of polyelectrolyte complexation. *J. Chem. Phys.* **2008**, *128*, 224908 DOI: 10.1063/1.2936834.

(103) Qin, J.; De Pablo, J. J. Criticality and connectivity in macromolecular charge complexation. *Macromolecules* **2016**, *49* (22), 8789–8800 DOI: 10.1021/acs.macromol.6b02113.

(104) Ou, Z.; Muthukumar, M. Entropy and enthalpy of polyelectrolyte complexation: Langevin dynamics simulations. *J. Chem. Phys.* **2006**, *124* (15), 154902 DOI: 10.1063/1.2178803.

(105) Wang, Q.; Schlenoff, J. B. The polyelectrolyte complex/coacervate continuum. *Macromolecules* **2014**, *47* (9), 3108–3116 DOI: 10.1021/ma500500q.

(106) Fu, J.; Schlenoff, J. B. Driving Forces for Oppositely Charged Polyion Association in Aqueous Solutions: Enthalpic, Entropic, but Not Electrostatic. *J. Am. Chem. Soc.* **2016**, *138* (3), 980–990 DOI: 10.1021/jacs.5b11878.

(107) Salehi, A.; Larson, R. G. A Molecular Thermodynamic Model of Complexation in Mixtures of Oppositely Charged Polyelectrolytes with Explicit Account of Charge Association/Dissociation. *Macromolecules* **2016**, *49* (24), 9706–9719 DOI: 10.1021/acs.macromol.6b01464.

(108) Srivastava, S.; Tirrell, M. V. *Advances in Chemical Physics*; Rice, S. A., Dinner, A. R., Eds.; John Wiley and Sons: Hoboken, NJ, 2016.

(109) Sing, C. E. Development of the modern theory of polymeric complex coacervation. *Adv. Colloid Interface Sci.* **2017**, *239*, 2–16 DOI: 10.1016/j.cis.2016.04.004.

(110) Perry, S. L.; Sing, C. E. PRISM-Based Theory of Complex Coacervation: Excluded Volume versus Chain Correlation. *Macromolecules* **2015**, *48* (14), 5040–5053 DOI: 10.1021/acs.macromol.5b01027.

(111) Salis, A.; Ninham, B. W. Models and mechanisms of Hofmeister effects in electrolyte solutions, and colloid and protein systems revisited. *Chem. Soc. Rev.* **2014**, *43* (21), 7358–7377 DOI: 10.1039/c4cs00144c.

(112) Priftis, D.; Laugel, N.; Tirrell, M. Thermodynamic characterization of polypeptide complex coacervation. *Langmuir* **2012**, *28* (45), 15947–15957 DOI: 10.1021/la302729r.

(113) Manning, G. S. Limiting laws and counterion condensation in polyelectrolyte solutions I. Colligative properties. *J. Chem. Phys.* **1969**, *51*, 924–933 DOI: doi.org/10.1063/1.1672157.

(114) Liu, S.; Muthukumar, M. Langevin dynamics simulation of counterion distribution around isolated flexible polyelectrolyte chains. *J. Chem. Phys.* **2002**, *116* (22), 9975–9982 DOI: 10.1063/1.1476930.

(115) Bates, F. S.; Hillmyer, M. a.; Lodge, T. P.; Bates, C. M.; Delaney, K. T.; Fredrickson, G. H. Multiblock Polymers : *Science (80-.).* **2012**, *336*, 434–440 DOI: 10.1126/science.1215368.

(116) Wuttke, R.; Hofmann, H.; Nettels, D.; Borgia, M. B.; Mittal, J.; Best, R. B.; Schuler, B. Temperature-dependent solvation modulates the dimensions of disordered proteins. *Proc. Natl. Acad. Sci. U. S. A.* **2014**, *111* (14), 5213–5218 DOI: 10.1073/pnas.1313006111.

(117) Brangwynne, C. P.; Mitchison, T. J.; Hyman, A. A. Active liquid-like behavior of nucleoli determines their size and shape in Xenopus laevis oocytes. *Proc. Natl. Acad. Sci. U. S. A.* **2011**, *108* (11), 4334–4339 DOI: 10.1073/pnas.1017150108.

(118) Weber, S. C.; Brangwynne, C. P. Getting RNA and protein in phase. *Cell* **2012**, *149* (6), 1188–1191 DOI: 10.1016/j.cell.2012.05.022.

(119) Wei, M. T.; Elbaum-Garfinkle, S.; Holehouse, A. S.; Chen, C. C. H.; Feric, M.; Arnold, C. B.; Priestley, R. D.; Pappu, R. V.; Brangwynne, C. P. Phase behaviour of disordered proteins underlying low density and high permeability of liquid organelles. *Nat. Chem.* **2017**, *9* (11), 1118–1125 DOI: 10.1038/NCHEM.2803.

(120) Elbaum-Garfinkle, S.; Kim, Y.; Szczepaniak, K.; Chen, C. C. H.; Eckmann, C. R.; Myong, S.; Brangwynne, C. P. The disordered P granule protein LAF-1 drives phase separation into droplets with tunable viscosity and dynamics. *Proc. Natl. Acad. Sci. U. S. A.* **2015**, *112* (23), 7189–7194 DOI: 10.1073/pnas.1504822112.

(121) Hyman, A. A.; Simons, K. Beyond oil and water - Phase transitions in cells. *Science (80-.).* **2012**, *337* (6098), 1047–1049 DOI: 10.1126/science.1223728.

(122) Hyman, A. A.; Weber, C. A.; Jülicher, F. Liquid-Liquid Phase Separation in Biology. *Annu. Rev. Cell Dev. Biol.* **2014**, *30* (1), 39–58 DOI: 10.1146/annurev-cellbio-100913-013325.

(123) Banani, S. F.; Lee, H. O.; Hyman, A. A.; Rosen, M. K. Biomolecular condensates: Organizers of cellular biochemistry. *Nat. Rev. Mol. Cell Biol.* **2017**, *18* (5), 285–298 DOI: 10.1038/nrm.2017.7.

(124) Zhu, L.; Brangwynne, C. P. Nuclear bodies: The emerging biophysics of nucleoplasmic phases. *Curr. Opin. Cell Biol.* **2015**, *34*, 23–30 DOI: 10.1016/j.ceb.2015.04.003.

(125) Nott, T. J.; Petsalaki, E.; Farber, P.; Jervis, D.; Fussner, E.; Plochowietz, A.; Craggs, T. D.; Bazett-Jones, D. P.; Pawson, T.; Forman-Kay, J. D.; Baldwin, A. J. Phase Transition of a Disordered Nuage Protein Generates Environmentally Responsive Membraneless Organelles. *Mol. Cell* **2015**, *57* (5), 936–947 DOI: 10.1016/j.molcel.2015.01.013.

(126) Koga, S.; Williams, D. S.; Perriman, A. W.; Mann, S. Peptide-nucleotide microdroplets as a step towards a membrane-free protocell model. *Nat. Chem.* **2011**, *3* (9), 720–724 DOI: 10.1038/nchem.1110.

(127) Martin, N.; Li, M.; Mann, S. Selective Uptake and Refolding of Globular Proteins in Coacervate Microdroplets. *Langmuir* **2016**, *32* (23), 5881–5889 DOI: 10.1021/acs.langmuir.6b01271.

(128) Lin, Y. H.; Forman-Kay, J. D.; Chan, H. S. Sequence-Specific Polyampholyte Phase Separation in Membraneless Organelles. *Phys. Rev. Lett.* **2016**, *117* (17) DOI: 10.1103/PhysRevLett.117.178101.

(129) Das, S.; Amin, A. N.; Lin, Y. H.; Chan, H. S. Coarse-grained residue-based models of disordered protein condensates: Utility and limitations of simple charge pattern parameters. *Phys. Chem. Chem. Phys.* **2018**, *20* (45), 28558–28574 DOI: 10.1039/c8cp05095c.

(130) Dignon, G. L.; Zheng, W.; Best, R. B.; Kim, Y. C.; Mittal, J. Relation between single-molecule properties and phase behavior of intrinsically disordered proteins. *Proc. Natl. Acad. Sci. U. S. A.* **2018**, *115* (40), 9929–9934 DOI: 10.1073/pnas.1804177115.

(131) Berry, J.; Brangwynne, C. P.; Haataja, M. Physical principles of intracellular organization via active and passive phase transitions. *Reports Prog. Phys.* **2018**, *81* (4), 46601 DOI: 10.1088/1361-6633/aaa61e.

(132) Panganiban, B.; Qiao, B.; Jiang, T.; DelRe, C.; Obadia, M. M.; Nguyen, T. D.; Smith, A. A. A.; Hall, A.; Sit, I.; Crosby, M. G.; Dennis, P. B.; Drockenmuller, E.; De La Cruz, M. O.; Xu, T. Random heteropolymers preserve protein function in foreign environments. *Science (80-.).* **2018**, *359* (6381), 1239–1243 DOI: 10.1126/science.aao0335.

(133) Perry, S. L. Phase separation: Bridging polymer physics and biology. *Curr. Opin. Colloid Interface Sci.* **2019**, *39*, 86–97 DOI: 10.1016/j.cocis.2019.01.007.

(134) Rice, S. A.; Dinner, A. R. *Advances in Chemical Physics*; Rice, S. A., Dinner, A. R., Eds.; John Wiley and Sons: Hoboken, NJ, 2017; Vol. 162.

(135) Sing, C. E. Development of the modern theory of polymeric complex coacervation. *Adv. Colloid Interface Sci.* **2017**, *239*, 2–16 DOI: 10.1016/j.cis.2016.04.004.

(136) Chang, L. W.; Lytle, T. K.; Radhakrishna, M.; Madinya, J. J.; Vélez, J.; Sing, C. E.; Perry, S. L. Sequence and entropy-based control of complex coacervates. *Nat. Commun.* **2017**, *8* (1), 1273 DOI: 10.1038/s41467-017-01249-1.

(137) Cohn, J. Theory of electrolytes. *Phys. Fluids* **1963**, *6* (1), 21–27 DOI: 10.1063/1.1724503.

(138) Kudlay, A.; De la Cruz, M. O. Precipitation of oppositely charged polyelectrolytes in salt solutions. *J. Chem. Phys.* **2004**, *120* (1), 404–412 DOI: 10.1063/1.1629271.

(139) Riggleman, R. A.; Kumar, R.; Fredrickson, G. H. Investigation of the interfacial tension of complex coacervates using field-theoretic simulations. *J. Chem. Phys.* **2012**, *136* (2), 24903 DOI: 10.1063/1.3674305.

(140) Delaney, K. T.; Fredrickson, G. H. Theory of polyelectrolyte complexation - Complex coacervates are self-coacervates. *J. Chem. Phys.* **2017**, *146* (22), 224902 DOI: 10.1063/1.4985568.

(141) Zhang, P.; Alsaifi, N. M.; Wu, J.; Wang, Z. G. Polyelectrolyte complex coacervation: Effects of concentration asymmetry. *J. Chem. Phys.* **2018**, *149* (16), 163303 DOI: 10.1063/1.5028524.

(142) Zhang, P.; Shen, K.; Alsaifi, N. M.; Wang, Z. G. Salt Partitioning in Complex Coacervation of Symmetric Polyelectrolytes. *Macromolecules* **2018**, *51* (15), 5586–5593 DOI: 10.1021/acs.macromol.8b00726.

(143) Wang, Z.; Rubinstein, M. Regimes of conformational transitions of a diblock polyampholyte. *Macromolecules* **2006**, *39* (17), 5897–5912 DOI: 10.1021/ma0607517.

(144) Rubinstein, M.; Liao, Q.; Panyukov, S. Structure of Liquid Coacervates Formed by Oppositely Charged Polyelectrolytes. *Macromolecules* **2018**, *51* (23), 9572–9588 DOI: 10.1021/acs.macromol.8b02059.

(145) Rumyantsev, A. M.; Zhulina, E. B.; Borisov, O. V. Complex Coacervate of Weakly Charged Polyelectrolytes: Diagram of States. *Macromolecules* **2018**, *51* (10), 3788–3801 DOI: 10.1021/acs.macromol.8b00342.

(146) Rumyantsev, A. M.; Kramarenko, E. Y.; Borisov, O. V. Microphase Separation in Complex Coacervate Due to Incompatibility between Polyanion and Polycation. *Macromolecules* **2018**, *51* (17), 6587–6601 DOI: 10.1021/acs.macromol.8b00721.

(147) Adhikari, S.; Leaf, M. A.; Muthukumar, M. Polyelectrolyte complex coacervation by electrostatic dipolar interactions. *J. Chem. Phys.* **2018**, *149* (16), 163308 DOI: 10.1063/1.5029268.

(148) Friedowitz, S.; Salehi, A.; Larson, R. G.; Qin, J. Role of electrostatic correlations in polyelectrolyte charge association. *J. Chem. Phys.* **2018**, *149* (16), 163335 DOI: 10.1063/1.5034454.

(149) Rathee, V. S.; Zervoudakis, A. J.; Sidky, H.; Sikora, B. J.; Whitmer, J. K. Weak polyelectrolyte complexation driven by associative charging. *J. Chem. Phys.* **2018**, *148* (11), 114901 DOI: 10.1063/1.5017941.

(150) Rathee, V. S.; Sidky, H.; Sikora, B. J.; Whitmer, J. K. Role of Associative Charging in the Entropy-Energy Balance of Polyelectrolyte Complexes. *J. Am. Chem. Soc.* **2018**, *140* (45), 15319–15328 DOI: 10.1021/jacs.8b08649.

(151) Li, L.; Srivastava, S.; Andreev, M.; Marciel, A. B.; De Pablo, J. J.; Tirrell, M. V. Phase Behavior and Salt Partitioning in Polyelectrolyte Complex Coacervates. *Macromolecules* **2018**, *51* (8), 2988–2995 DOI: 10.1021/acs.macromol.8b00238.

(152) Priftis, D.; Xia, X.; Margossian, K. O.; Perry, S. L.; Leon, L.; Qin, J.; De Pablo, J. J.; Tirrell, M. Ternary, tunable polyelectrolyte complex fluids driven by complex coacervation. *Macromolecules* **2014**, *47* (9), 3076–3085 DOI: 10.1021/ma500245j.

(153) Marciel, A. B.; Srivastava, S.; Tirrell, M. V. Structure and rheology of polyelectrolyte complex coacervates. *Soft Matter* **2018**, *14* (13), 2454–2464 DOI: 10.1039/c7sm02041d.

(154) Biesheuvel, P. M.; Stuart, M. A. C. Cylindrical cell model for the electrostatic free energy of polyelectrolyte complexes. *Langmuir* **2004**, *20* (11), 4764–4770 DOI: 10.1021/la0496789.

(155) Spruijt, E.; Leermakers, F. A. M.; Fokkink, R.; Schweins, R.; Van Well, A. A.; Cohen Stuart, M. A.; Van Der Gucht, J. Structure and dynamics of polyelectrolyte complex coacervates studied by scattering of neutrons, X-rays, and light. *Macromolecules* **2013**, *46* (11), 4596–4605 DOI: 10.1021/ma400132s.

(156) Wang, Q.; Schlenoff, J. B. The polyelectrolyte complex/coacervate continuum. *Macromolecules* **2014**, *47* (9), 3108–3116 DOI: 10.1021/ma500500q.

(157) Brumby, P. E.; Haslam, A. J.; De Miguel, E.; Jackson, G. Subtleties in the calculation of the pressure and pressure tensor of anisotropic particles from volume-perturbation methods and the apparent asymmetry of the compressive and expansive contributions. *Mol. Phys.* **2011**, *109* (1), 169–189 DOI: 10.1080/00268976.2010.530301.

(158) Honnell, K. G.; Hall, C. K.; Dickman, R. On the pressure equation for chain molecules. *J. Chem. Phys.* **1987**, *87* (1), 664–674 DOI: 10.1063/1.453562.

(159) Orkoulas, G.; Panagiotopoulos, A. Z. Free energy and phase equilibria for the restricted primitive model of ionic fluids from Monte Carlo simulations. *J. Chem. Phys.* **1994**, *101* (2), 1452–1459 DOI: 10.1063/1.467770.

(160) Kumar, S. K.; Szleifer, I.; Panagiotopoulos, A. Z. Determination of the chemical potentials of polymeric systems from Monte Carlo simulations. *Phys. Rev. Lett.* **1991** DOI: 10.1103/PhysRevLett.66.2935.

(161) Andreev, M.; Prabhu, V. M.; Douglas, J. F.; Tirrell, M.; De Pablo, J. J. Complex Coacervation in Polyelectrolytes from a Coarse-Grained Model. *Macromolecules* **2018**, *51* (17), 6717–6723 DOI: 10.1021/acs.macromol.8b00556.

(162) D. A. McQuarrie. *Statistical Mechanics*; HarperCollins Publishing, Inc.: New York, 1976.

(163) Radhakrishna, M.; Sing, C. E. Charge Correlations for Precise, Coulombically Driven Self Assembly. *Macromol. Chem. Phys.* **2016**, *217* (2), 126–136 DOI: 10.1002/macp.201500278.

(164) Manning, G. S. Limiting laws and counterion condensation in polyelectrolyte solutions. 7. Electrophoretic mobility and conductance. *J. Phys. Chem.* **1981**, *85* (11), 1506–1515 DOI: 10.1021/j150611a011.

(165) Muthukumar, M. Theory of counter-ion condensation on flexible polyelectrolytes: Adsorption mechanism. *J. Chem. Phys.* **2004**, *120* (19), 9343–9350 DOI: 10.1063/1.1701839.

(166) Dyson, H. J.; Wright, P. E. Coupling of folding and binding for unstructured proteins. *Curr. Opin. Struct. Biol.* **2002**, *12* (1), 54–60 DOI: 10.1016/S0959-440X(02)00289-0.

(167) Gething, M. J.; Sambrook, J. Protein folding in the cell. *Nature* **1992**, *355* (6355), 33–45 DOI: 10.1038/355033a0.

(168) Dobson, C. M. Protein folding and misfolding. *Nature*. 2003.

(169) Leopold, P. E.; Montal, M.; Onuchic, J. N. Protein folding funnels: A kinetic approach to the sequence-structure relationship. *Proc. Natl. Acad. Sci. U. S. A.* **1992** DOI: 10.1073/pnas.89.18.8721.

(170) Anfinsen, C. B.; Haber, E.; Sela; White, F. H. the Kinetics of Formation of Native Ribonuclease. *Proc. Natl. Acad. Sci.* **1961**, *47* (9), 1309–1314.

(171) Romero, P.; Obradovic, Z.; Li, X.; Garner, E. C.; Brown, C. J.; Dunker, A. K. Sequence complexity of disordered protein - Romero - 2000 - Proteins: Structure, Function, and Bioinformatics - Wiley Online Library. **2001**, *48* (December 1999), 38–48.

(172) Receveur-Bréhot, V.; Bourhis, J. M.; Uversky, V. N.; Canard, B.; Longhi, S. Assessing protein disorder and induced folding. *Proteins Struct. Funct. Genet.* **2006**, *62* (1), 24–45 DOI: 10.1002/prot.20750.

(173) Kriwacki, R. W.; Hengst, L.; Tennant, L.; Reed, S. I.; Wright, P. E. Structural studies of p21Waf1/Cip1/Sdi1 in the free and Cdk2-bound state: Conformational disorder mediates binding diversity. *Proc. Natl. Acad. Sci. U. S. A.* **1996**, *93* (21), 11504–11509 DOI: 10.1073/pnas.93.21.11504.

(174) Fuxreiter, M.; Simon, I.; Friedrich, P.; Tompa, P. Preformed structural elements feature in partner recognition by intrinsically unstructured proteins. *J. Mol. Biol.* **2004** DOI: 10.1016/j.jmb.2004.03.017.

(175) Tompa, P.; Fuxreiter, M. Fuzzy complexes: polymorphism and structural disorder in protein-protein interactions. *Trends Biochem. Sci.* **2008**, *33* (1), 2–8 DOI: 10.1016/j.tibs.2007.10.003.

(176) Fuxreiter, M.; Tompa, P. Fuzzy complexes: A more stochastic view of protein function. *Adv. Exp. Med. Biol.* **2012** DOI: 10.1007/978-1-4614-0659-4_1.

(177) Brzovic, P. S.; Heikaus, C. C.; Kisselev, L.; Vernon, R.; Herbig, E.; Pacheco, D.; Warfield, L.; Littlefield, P.; Baker, D.; Klevit, R. E.; Hahn, S. The Acidic Transcription Activator Gcn4 Binds the Mediator Subunit Gal11/Med15 Using a Simple Protein Interface Forming a Fuzzy Complex. *Mol. Cell* **2011**, *44* (6), 942–953 DOI: 10.1016/j.molcel.2011.11.008.

(178) Sharma, R.; Raduly, Z.; Miskei, M.; Fuxreiter, M. Fuzzy complexes: Specific binding without complete folding. *FEBS Lett.* **2015**, *589* (19), 2533–2542 DOI: 10.1016/j.febslet.2015.07.022.

(179) Mao, A. H.; Crick, S. L.; Vitalis, A.; Chicoine, C. L.; Pappu, R. V. Net charge per residue modulates conformational ensembles of intrinsically disordered proteins. *Proc. Natl. Acad. Sci. U. S. A.* **2010**, *107* (18), 8183–8188 DOI: 10.1073/pnas.0911107107.

(180) Müller-Späth, S.; Soranno, A.; Hirschfeld, V.; Hofmann, H.; Rüegger, S.; Reymond, L.; Nettels, D.; Schuler, B. Charge interactions can dominate the dimensions of intrinsically disordered proteins. *Proc. Natl. Acad. Sci. U. S. A.* **2010**, *107* (33), 14609–14614 DOI: 10.1073/pnas.1001743107.

(181) Iakoucheva, L. M.; Radivojac, P.; Brown, C. J.; O'Connor, T. R.; Sikes, J. G.; Obradovic, Z.; Dunker, A. K. The importance of intrinsic disorder for protein phosphorylation. *Nucleic Acids Res.* **2004**, *32* (3), 1037–1049 DOI: 10.1093/nar/gkh253.

(182) Wright, P. E.; Dyson, H. J. Intrinsically disordered proteins in cellular signalling and regulation. *Nature Reviews Molecular Cell Biology*. 2015.

(183) Iakoucheva, L. M.; Brown, C. J.; Lawson, J. D.; Obradović, Z.; Dunker, A. K. Intrinsic disorder in cell-signaling and cancer-associated proteins. *J. Mol. Biol.* **2002**, *323* (3), 573–584 DOI: 10.1016/S0022-2836(02)00969-5.

(184) Dunker, A. K.; Silman, I.; Uversky, V. N.; Sussman, J. L. Function and structure of inherently disordered proteins. *Curr. Opin. Struct. Biol.* **2008**, *18* (6), 756–764 DOI: 10.1016/j.sbi.2008.10.002.

(185) Das, R. K.; Huang, Y.; Phillips, A. H.; Kriwacki, R. W.; Pappu, R. V. Cryptic sequence features within the disordered protein p27Kip1 regulate cell cycle signaling. *Proc. Natl. Acad. Sci. U. S. A.* **2016**, *113* (20), 5616–5621 DOI: 10.1073/pnas.1516277113.

(186) Wei, M. T.; Elbaum-Garfinkle, S.; Holehouse, A. S.; Chen, C. C. H.; Feric, M.; Arnold, C. B.; Priestley, R. D.; Pappu, R. V.; Brangwynne, C. P. Phase behaviour of disordered proteins underlying low density and high permeability of liquid organelles. *Nat. Chem.* **2017**, *9* (11) DOI: 10.1038/NCHEM.2803.

(187) Toretsky, J. A.; Wright, P. E. Assemblages: Functional units formed by cellular phase separation. *J. Cell Biol.* **2014**, *206* (5), 579–588 DOI: 10.1083/jcb.201404124.

(188) Nott, T. J.; Petsalaki, E.; Farber, P.; Jervis, D.; Fussner, E.; Plochowietz, A.; Craggs, T. D.; Bazett-Jones, D. P.; Pawson, T.; Forman-Kay, J. D.; Baldwin, A. J. Phase Transition of a Disordered Nuage Protein Generates Environmentally Responsive Membraneless Organelles. *Mol. Cell* **2015**, *57* (5), 936–947 DOI: 10.1016/j.molcel.2015.01.013.

(189) Li, P.; Banjade, S.; Cheng, H. C.; Kim, S.; Chen, B.; Guo, L.; Llaguno, M.; Hollingsworth, J. V.; King, D. S.; Banani, S. F.; Russo, P. S.; Jiang, Q. X.; Nixon, B. T.; Rosen, M. K. Phase transitions in the assembly of multivalent signalling proteins. *Nature* **2012**, *483* (7389), 336–340 DOI: 10.1038/nature10879.

(190) Aumiller, W. M.; Keating, C. D. Phosphorylation-mediated RNA/peptide complex coacervation as a model for intracellular liquid organelles. *Nat. Chem.* **2016**, *8* (2), 129–137 DOI: 10.1038/nchem.2414.

(191) Higgs, P. G.; Joanny, J. F. Theory of polyampholyte solutions. *J. Chem. Phys.* **1991**, *94* (2), 1543–1554 DOI: 10.1063/1.460012.

(192) A. V. Dobrynin and M. Rubinstein. Flory Theory of a Polyampholyte Chain. *J. Phys. II* **1995**, *5*, 677–695 DOI: https://doi.org/10.1051/jp2:1995157.

(193) Sawle, L.; Ghosh, K. A theoretical method to compute sequence dependent configurational properties in charged polymers and proteins. *J. Chem. Phys.* **2015**, *143* (8), 085101 DOI: 10.1063/1.4929391.

(194) Firman, T.; Ghosh, K. Sequence charge decoration dictates coil-globule transition in intrinsically disordered proteins. *J. Chem. Phys.* **2018**, *148* (12), 123305 DOI: 10.1063/1.5005821.

(195) Kantor, Y.; Li, H.; Kardar, M. Conformations of polyampholytes. *Phys. Rev. Lett.* **1992**, *69* (1), 61–64 DOI: 10.1103/PhysRevLett.69.61.

(196) Xu, B.; Huang, L.; Liang, H. Thermodynamic behaviors of polyampholytes at low temperatures. *J. Chem. Phys.* **2004**, *121* (15), 7494–7500 DOI: 10.1063/1.1792191.

(197) Samanta, H. S.; Chakraborty, D.; Thirumalai, D. Charge fluctuation effects on the shape of flexible polyampholytes with applications to intrinsically disordered proteins. *J. Chem. Phys.* **2018**, *149* (16) DOI: 10.1063/1.5035428.

(198) Srivastava, D.; Muthukumar, M. Sequence dependence of conformations of polyampholytes. *Macromolecules* **1996**, *29* (6), 2324–2326 DOI: 10.1021/ma951204g.

(199) Jiang, J.; Feng, J.; Liu, H.; Hu, Y. Phase behavior of polyampholytes from charged hard-sphere chain model. *J. Chem. Phys.* **2006**, *124* (14) DOI: 10.1063/1.2186316.

(200) D. W. Cheong and A. Z. Panagiotopoulos. Phase behaviour of polyampholyte chains from grand canonical Monte Carlo simulations. *Mol. Phys.* **2005**, *103* (3031–3044) DOI: 10.1080/00268970500186045.

(201) Das, S.; Eisen, A.; Lin, Y. H.; Chan, H. S. A Lattice Model of Charge-Pattern-Dependent Polyampholyte Phase Separation. *J. Phys. Chem. B* **2018**, *122* (21), 5418–5431 DOI: 10.1021/acs.jpcb.7b11723.

(202) Lin, Y. H.; Forman-Kay, J. D.; Chan, H. S. Sequence-Specific Polyampholyte Phase Separation in Membraneless Organelles. *Phys. Rev. Lett.* **2016**, *117* (17), 1–6 DOI: 10.1103/PhysRevLett.117.178101.

(203) Lin, Y. H.; Song, J.; Forman-Kay, J. D.; Chan, H. S. Random-phase-approximation theory for sequence-dependent, biologically functional liquid-liquid phase separation of intrinsically disordered proteins. *J. Mol. Liq.* **2017**, *228*, 176–193 DOI: 10.1016/j.molliq.2016.09.090.

(204) Danielsen, S. P. O.; McCarty, J.; Shea, J. E.; Delaney, K. T.; Fredrickson, G. H. Molecular design of self-coacervation phenomena in block polyampholytes. *Proc. Natl. Acad. Sci. U. S. A.* **2019**, *116* (17), 8224–8232 DOI: 10.1073/pnas.1900435116.

(205) Delaney, K. T.; Fredrickson, G. H. Theory of polyelectrolyte complexation - Complex coacervates are self-coacervates. *J. Chem. Phys.* **2017**, *146* (22), 224902 DOI: 10.1063/1.4985568.

(206) McCarty, J.; Delaney, K. T.; Danielsen, S. P. O.; Fredrickson, G. H.; Shea, J. E. Complete Phase Diagram for Liquid-Liquid Phase Separation of Intrinsically Disordered Proteins. *J. Phys. Chem. Lett.* **2019**, *10* (8), 1644–1652 DOI: 10.1021/acs.jpclett.9b00099.

(207) Patterson, A. L.; Danielsen, S. P. O.; Yu, B.; Davidson, E. C.; Fredrickson, G. H.; Segalman, R. A. Sequence Effects on Block Copolymer Self-Assembly through Tuning Chain Conformation and Segregation Strength Utilizing Sequence-Defined Polypeptoids. *Macromolecules* **2019**, *52* (3), 1277–1286 DOI: 10.1021/acs.macromol.8b02298.

(208) Riggleman, R. A.; Kumar, R.; Fredrickson, G. H. Investigation of the interfacial tension of complex coacervates using field-theoretic simulations. *J. Chem. Phys.* **2012**, *136* (2) DOI: 10.1063/1.3674305.

(209) M. Castelnovo and J.-F. Joanny. Complexation between oppositely charged polyelectrolytes: Beyond the Random Phase Approximation. *Eur. Phys. J. E* **2001**, *6*, 377–386 DOI: 10.1007/s10189-001-8051-7.

(210) Dias, R. S.; Linse, P.; Pais, A. A. C. C. Stepwise disproportionation in polyelectrolyte complexes. *J. Comput. Chem.* **2011**, *32* (12), 2697–2707 DOI: 10.1002/jcc.21851.

(211) Jeon, J.; Dobrynin, A. V. Molecular dynamics simulations of polyelectrolyte-polyampholyte complexes. Effect of solvent quality and salt concentration. *J. Phys. Chem. B* **2006**, *110* (48), 24652–24665 DOI: 10.1021/jp064288b.

(212) Manning, G. S. Limiting laws and counterion condensation in polyelectrolyte solutions. 7. Electrophoretic mobility and conductance. *J. Phys. Chem.* **1969**, *51*, 924–933 DOI: 10.1021/j150611a011.

(213) Lytle, T. K.; Sing, C. E. Transfer matrix theory of polymer complex coacervation. *Soft Matter* **2017**, *13* (39), 7001–7012 DOI: 10.1039/c7sm01080j.

(214) Lytle, T. K.; Chang, L. W.; Markiewicz, N.; Perry, S. L.; Sing, C. E. Designing Electrostatic Interactions via Polyelectrolyte Monomer Sequence. *ACS Cent. Sci.* **2019**, *5* (4), 709–718 DOI: 10.1021/acscentsci.9b00087.

(215) Ong, G. M. C.; Sing, C. E. Mapping the phase behavior of coacervate-driven self-assembly in diblock copolyelectrolytes. *Soft Matter* **2019**, *15* (25), 5116–5127 DOI: 10.1039/c9sm00741e.

(216) Danielsen, S. P. O.; McCarty, J.; Shea, J. E.; Delaney, K. T.; Fredrickson, G. H. Small ion effects on self-coacervation phenomena in block polyampholytes. *J. Chem. Phys.* **2019**, *151* (3) DOI: 10.1063/1.5109045.

(217) Liu, Y.; Momani, B.; Winter, H. H.; Perry, S. L. Rheological characterization of liquid-to-solid transitions in bulk polyelectrolyte complexes. *Soft Matter* **2017**, *13* (40), 7332–7340 DOI: 10.1039/c7sm01285c.

(218) Sokolova, E.; Spruijt, E.; Hansen, M. M. K.; Dubuc, E.; Groen, J.; Chokkalingam, V.; Piruska, A.; Heus, H. A.; Huck, W. T. S. Enhanced transcription rates in membrane-free protocells formed by coacervation of cell lysate. *Proc. Natl. Acad. Sci. U. S. A.* **2013**, *110* (29), 11692–11697 DOI: 10.1073/pnas.1222321110.

(219) Borue, V. Y.; Erukhimovich, I. Y. A Statistical Theory of Globular Polyelectrolyte Complexes. *Macromolecules* **1990**, *23* (15), 3625–3632 DOI: 10.1021/ma00217a015.

(220) Duan, X.; Nakamura, I. A new lattice Monte Carlo simulation for dielectric saturation in ion-containing liquids. *Soft Matter* **2015**, *11* (18), 3566–3571 DOI: 10.1039/c5sm00336a.

(221) Levy, A.; Andelman, D.; Orland, H. Dielectric constant of ionic solutions: A field-theory approach. *Phys. Rev. Lett.* **2012**, *108* (22), 227801 DOI: 10.1103/PhysRevLett.108.227801.

(222) Kumar, R.; Fredrickson, G. H. Theory of polyzwitterion conformations. *J. Chem. Phys.* **2009**, *131* (10), 104901 DOI: 10.1063/1.3216107.

(223) Andreev, M.; De Pablo, J. J.; Chremos, A.; Douglas, J. F. Influence of Ion Solvation on the Properties of Electrolyte Solutions. *J. Phys. Chem. B* **2018**, *122* (14), 4029–4034 DOI: 10.1021/acs.jpcb.8b00518.

(224) Lou, J.; Friedowitz, S.; Qin, J.; Xia, Y. Tunable Coacervation of Well-Defined Homologous Polyanions and Polycations by Local Polarity. *ACS Cent. Sci.* **2019**, *5* (3), 549–557 DOI: 10.1021/acscentsci.8b00964.

(225) Dzwolak, W.; Ravindra, R.; Nicolini, C.; Jansen, R.; Winter, R. The Diastereomeric Assembly of Polylysine is the Low-Volume Pathway for Preferential Formation of β-Sheet Aggregates. *J. Am. Chem. Soc.* **2004**, *126* (12), 3762–3768 DOI: 10.1021/ja039138i.

(226) Fändrich, M.; Dobson, C. M. The behaviour of polyamino acids reveals an inverse side chain effect in amyloid structure formation. *EMBO J.* **2002**, *21* (21), 5682–5690 DOI: 10.1093/emboj/cdf573.

(227) C. R. Baiz and M. R. A. Tokmakoff. Ultrafast Infrared Vibrational Spectroscopy. *ed. M. D. Fayer, CRC Press* **2012**, 5682–5690.

(228) Tabandeh, S.; Leon, L. Engineering peptide-based polyelectrolyte complexes with increased hydrophobicity. *Molecules* **2019**, *24* (5), 868 DOI: 10.3390/molecules24050868.

(229) Thünemann, A. F.; Müller, M.; Dautzenberg, H.; Joanny, J. F.; Löwen, H. Polyelectrolyte Complexes. *Adv. Polym. Sci.* **2004**, *166*, 113–171 DOI: 10.1021/ie50670a007.

(230) Bucur, C. B.; Sui, Z.; Schlenoff, J. B. Ideal mixing in polyelectrolyte complexes and multilayers: Entropy driven assembly. *J. Am. Chem. Soc.* **2006** DOI: 10.1021/ja064532c.

(231) Hwang, D. S.; Zeng, H.; Lu, Q.; Israelachvili, J.; Waite, J. H. Adhesion mechanism in a DOPA-deficient foot protein from green mussels. *Soft Matter* **2012**, *8* (20), 5640–5648 DOI: 10.1039/c2sm25173f.

(232) Fulton, A. B. How crowded is the cytoplasm? *Cell* **1982**, *30* (2), 345–347 DOI: 10.1016/0092-8674(82)90231-8.

(233) Zimmerman, S. B.; Trach, S. O. Estimation of macromolecule concentrations and excluded volume effects for the cytoplasm of Escherichia coli. *J. Mol. Biol.* **1991**, *222* (3), 599–620 DOI: 10.1016/0022-2836(91)90499-V.

(234) Minton, A. P. Excluded volume as a determinant of macromolecular structure and reactivity. *Biopolymers* **1981**, *20* (10), 2093–2120 DOI: 10.1002/bip.1981.360201006.

(235) Vrbka, L.; Vondrášek, J.; Jagoda-Cwiklik, B.; Vácha, R.; Jungwirth, P. Quantification and rationalization of the higher affinity of sodium over potassium to protein surfaces. *Proc. Natl. Acad. Sci. U. S. A.* **2006**, *103* (42), 15440–15444 DOI: 10.1073/pnas.0606959103.

(236) Zhang, Y.; Cremer, P. S. Interactions between macromolecules and ions: the Hofmeister series. *Curr. Opin. Chem. Biol.* **2006**, *10* (6), 658–663 DOI: 10.1016/j.cbpa.2006.09.020.

(237) Leontidis, E. Hofmeister anion effects on surfactant self-assembly and the formation of mesoporous solids. *Curr. Opin. Colloid Interface Sci.* **2002**, *7* (1–2), 81–91 DOI: 10.1016/S1359-0294(02)00010-9.

(238) Kunz, W. Specific ion effects in colloidal and biological systems. *Curr. Opin. Colloid Interface Sci.* **2010**, *15* (1–2), 34–39 DOI: 10.1016/j.cocis.2009.11.008.

(239) Hofmeister, F. No Title. *Arch. Exp. Pathol. Pharmakol.* **1888**, *24*, 247–260 DOI: 10.1007/BF01918191.

(240) Kunz, W.; Lo Nostro, P.; Ninham, B. W. The present state of affairs with Hofmeister effects. *Curr. Opin. Colloid Interface Sci.* **2004**, *9* (1–2), 1–18 DOI: 10.1016/j.cocis.2004.05.004.

(241) Kunz, W. *Specific ion effects*; World Scientific, 2009.

(242) Saloma, M.; Tervasma, P.; Areva, S.; Kankare, J. The Hofmeister Anion Effect and the Growth of Polyelectrolyte Multilayers. **2004**, No. 9, 3679–3683.

(243) Ghostine, R. A.; Shamoun, R. F.; Schlenoff, J. B. Doping and diffusion in an extruded saloplastic polyelectrolyte complex. *Macromolecules* **2013**, *46* (10), 4089–4094 DOI: 10.1021/ma4004083.

(244) Schlenoff, J. B.; Rmaile, A. H.; Bucur, C. B. Hydration contributions to association in polyelectrolyte multilayers and complexes: Visualizing hydrophobicity. *J. Am. Chem. Soc.* **2008**, *130* (41), 13589–13597 DOI: 10.1021/ja802054k.

(245) Liposomes, L. F.; Correa, S.; Boehnke, N.; Deiss-yehiely, E.; Hammond, P. T. Solution Conditions Tune and Optimize. *ACS Nano* **2019**, *13*, 5623–5634 DOI: 10.1021/acsnano.9b00792.

(246) Dubas, S. T.; Schlenoff, J. B. Factors controlling the growth of polyelectrolyte multilayers. *Macromolecules* **1999**, *32* (24), 8153–8160 DOI: 10.1021/ma981927a.

(247) Collins, K. D. Ion hydration: Implications for cellular function, polyelectrolytes, and protein crystallization. *Biophys. Chem.* **2006**, *119* (3), 271–281 DOI: 10.1016/j.bpc.2005.08.010.

(248) Collins, K. D. Charge density-dependent strength of hydration and biological structure. *Biophys. J.* **1997**, *72* (1), 65–76 DOI: 10.1016/S0006-3495(97)78647-8.

(249) Collins, K. D. Ions from the Hofmeister series and osmolytes: Effects on proteins in solution and in the crystallization process. *Methods* **2004**, *34* (3), 300–311 DOI: 10.1016/j.ymeth.2004.03.021.

(250) Lyklema, J. Simple Hofmeister series. *Chem. Phys. Lett.* **2009**, *467* (4–6), 217–222 DOI: 10.1016/j.cplett.2008.11.013.

(251) Pearson, R. G. Hard and Soft Acids and Bases. *J. Am. Chem. Soc.* **1963**, *85* (22), 3533–3539 DOI: 10.1021/ja00905a001.

(252) Pearson, R. G. Hard and soft acids and bases, HSAB, part I: Fundamental principles. *J. Chem. Educ.* **1968**, *45* (9), 581–587 DOI: 10.1021/ed045p581.

(253) Kiriukhin, M. Y.; Collins, K. D. Dynamic hydration numbers for biologically important ions. *Biophys. Chem.* **2002**, *99* (2), 155–168 DOI: 10.1016/S0301-4622(02)00153-9.

(254) Sadman, K.; Wang, Q.; Chen, Y.; Keshavarz, B.; Jiang, Z.; Shull, K. R. In fl uence of Hydrophobicity on Polyelectrolyte Complexation. **2017** DOI: 10.1021/acs.macromol.7b02031.

(255) Tanford, C. The hydrophobic effect and the organization of living matter. *Science (80-.).* **1978**, *200* (4345), 1012–1018 DOI: 10.1126/science.653353.

(256) Lins, L.; Brasseur, R. The hydrophobic effect in protein folding. *FASEB J.* **1995**, *9* (7), 535–540 DOI: 10.1096/fasebj.9.7.7737462.